Repository Istituzionale dei Prodotti della Ricerca del Politecnico di Bari

New Methods and Instruments for Coastal Monitoring

This is a PhD Thesis

Original Citation:
New Methods and Instruments for Coastal Monitoring / Valentini, Nico. - (2017). [10.60576/poliba/iris/valentini-nico_phd2017]

Availability:
This version is available at http://hdl.handle.net/11589/100383 since: 2017-03-23

Published version
DOI:10.60576/poliba/iris/valentini-nico_phd2017

Publisher: Politecnico di Bari

Terms of use:

(Article begins on next page)

12 October 2024

LIBERATORIA PER L'ARCHIVIAZIONE DELLA TESI DI DOTTORATO

Al Magnifico Rettore
del Politecnico di Bari

Il sottoscritto Valentini Nico nato a Putignano il 03/09/88 residente a Rutigliano in

via San F.sco d'Assisi 174; e-mail: nicvalen@gmail.com; iscritto al

III° anno di Corso di Dottorato di Ricerca in R.S.A.T.E. ciclo XXIX ed essendo stato ammesso a sostenere l'esame

finale con la prevista discussione della tesi dal titolo:

NEW INSTRUMENTS AND METHODS FOR COASTAL MONITORING

DICHIARA

1) di essere consapevole che, ai sensi del D.P.R. n. 445 del 28.12.2000, le dichiarazioni mendaci, la falsità negli atti e l'uso di atti falsi sono puniti ai sensi del codice penale e delle Leggi speciali in materia, e che nel caso ricorressero dette ipotesi, decade fin dall'inizio e senza necessità di nessuna formalità dai benefici conseguenti al provvedimento emanato sulla base di tali dichiarazioni;
2) di essere iscritto al Corso di Dottorato di ricerca R.S.A.T.E. ciclo XXIX, corso attivato ai sensi del "*Regolamento dei Corsi di Dottorato di ricerca del Politecnico di Bari"*, emanato con D.R. n.286 del 01.07.2013;
3) di essere pienamente a conoscenza delle disposizioni contenute nel predetto Regolamento in merito alla procedura di deposito, pubblicazione e autoarchiviazione della tesi di dottorato nell'Archivio Istituzionale ad accesso aperto alla letteratura scientifica;
4) di essere consapevole che attraverso l'autoarchiviazione delle tesi nell'Archivio Istituzionale ad accesso aperto alla letteratura scientifica del Politecnico di Bari (IRIS-POLIBA), l'Ateneo archivierà e renderà consultabile in rete (nel rispetto della Policy di Ateneo di cui al D.R. 642 del 13.11.2015) il testo completo della tesi di dottorato, fatta salva la possibilità di sottoscrizione di apposite licenze per le relative condizioni di utilizzo (di cui al sito http://www.creativecommons.it/Licenze), e fatte salve, altresì, le eventuali esigenze di "embargo", legate a strette considerazioni sulla tutelabilità e sfruttamento industriale/commerciale dei contenuti della tesi, da rappresentarsi mediante compilazione e sottoscrizione del modulo in calce (Richiesta di embargo);
5) che la tesi da depositare in IRIS-POLIBA, in formato digitale (PDF/A) sarà del tutto identica a quelle **consegnate**/inviate/da inviarsi ai componenti della commissione per l'esame finale e a qualsiasi altra copia depositata presso gli Uffici del Politecnico di Bari in forma cartacea o digitale, ovvero a quella da discutere in sede di esame finale, a quella da depositare, a cura dell'Ateneo, presso le Biblioteche Nazionali Centrali di Roma e Firenze e presso tutti gli Uffici competenti per legge al momento del deposito stesso, e che di conseguenza va esclusa qualsiasi responsabilità del Politecnico di Bari per quanto riguarda eventuali errori, imprecisioni o omissioni nei contenuti della tesi;
6) che il contenuto e l'organizzazione della tesi è opera originale realizzata dal sottoscritto e non compromette in alcun modo i diritti di terzi, ivi compresi quelli relativi alla sicurezza dei dati personali; che pertanto il Politecnico di Bari ed i suoi funzionari sono in ogni caso esenti da responsabilità di qualsivoglia natura: civile, amministrativa e penale e saranno dal sottoscritto tenuti indenni da qualsiasi richiesta o rivendicazione da parte di terzi;
7) che il contenuto della tesi non infrange in alcun modo il diritto d'Autore né gli obblighi connessi alla salvaguardia di diritti morali od economici di altri autori o di altri aventi diritto, sia per testi, immagini, foto, tabelle, o altre parti di cui la tesi è composta.

Luogo e data Bari, 20/2/2017 Firma

Il/La sottoscritto, con l'autoarchiviazione della propria tesi di dottorato nell'Archivio Istituzionale ad accesso aperto del Politecnico di Bari (POLIBA-IRIS), pur mantenendo su di essa tutti i diritti d'autore, morali ed economici, ai sensi della normativa vigente (Legge 633/1941 e ss.mm.ii.),

CONCEDE

- al Politecnico di Bari il permesso di trasferire l'opera su qualsiasi supporto e di convertirla in qualsiasi formato al fine di una corretta conservazione nel tempo. Il Politecnico di Bari garantisce che non verrà effettuata alcuna modifica al contenuto e alla struttura dell'opera.
- al Politecnico di Bari la possibilità di riprodurre l'opera in più di una copia per fini di sicurezza, back-up e conservazione.

Luogo e data Bari, 20/2/2017 Firma

D.R.R.S

POLITECNICO DI BARI

12

2017

PhD Program in Environmental and Building Risk and Development

Coordinator: Prof. Michele Mossa

XXIX CYCLE Curriculum:
Coastal Engineering

DICATECh
Department of Civil, Environmental, Building Engineering and Chemistry

New Methods and Instruments for Coastal Monitoring

Supervisor: Prof. Leonardo Damiani
Department of Civil, Environmental, Building Engineering and Chemistry
Politecnico di Bari

PhD Student: Nico Valentini

D.R.R.S

Dottorato di Ricerca in Rischio e Sviluppo ambientale, territoriale ed edilizio

Coordinatore: Prof. Michele Mossa

XXIX CICLO Curriculum:
Ingegneria costiera

DICATECh
Dipartimento di Ingegneria Civile, Ambientale, del Territorio, Edile e di Chimica

POLITECNICO DI BARI

12

2017

Nuovi Strumenti e Metodi per il Monitoraggio Costiero

Supervisore: Prof. Leonardo Damiani
Dipartimento di Ingegneria Civile, Ambientale,
del Territorio, Edile e di Chimica
Politecnico di Bari

Dottorando: Nico Valentini

EXTENDED ABSTRACT

Nowadays, many European coasts are subject to erosive processes and the Italian coast is not an exception, indeed it has been suffering from severe erosion, one of the most visible consequences of a relentless depletion of the coastal environment, particularly alarming due to its crucial economic and social role. In this sense, a well-structured and continuous beach monitoring programme implemented within a far-sighted management strategy is required to support coastal interventions, aimed at the coastline protection or the mitigation of the erosive tendencies. Under this perspective, video systems have become widely used all around the world in coastal monitoring strategies, allowing both high temporal and spatial sampling frequency, with low logistic and costs efforts.

Main objective of this work is to contribute to the development of new instruments and methods able to be included in a wider coastal monitoring network for supporting regional planning and control activities.

A new system for video monitoring and surveillance of Apulian coasts (South Italy) has been recently developed. In the present thesis, the implementation of the system, oriented at some key characteristics such as easy installation, robustness, low cost, efficiency of the acquisition and tasks scheduling, concerned with the installation at two different sites, is described. The system design aims at obtaining a tool able to work automatically. The tool is composed by several routines implemented also with a web-application, addressed at images processing (e.g. shoreline extraction and geo-rectification), data analysis and sharing results about beach actual state and shore evolution, in quasi-real time. Within this context, a new specific model for shoreline detection, Shoreline Detection Model (SDM), has been developed. The present describes in details the algorithm, inspired by the global Probability of Boundary (gPb) concept and the seed-based segmentation, together with the image processing procedures used. It mainly allows extracting the sea/land boundary from automatic segmented Timex im-

ages. The SDM calibration and validation has been performed on coastal images derived from a video monitoring system installed back at Alimini (Lecce, IT) in 2005, by comparing automatic shoreline contours with manual detected ones, on several cross-shore transects. The application of the SDM on images recorded by the new system has allowed testing the model feasibility at sites characterized by different morphological features and geographical exposition. In real time, processed images and shoreline contours are so, uploaded and make freely downloadable. Moreover, shoreline time variation analysis is available on user-selected transects. The reconstruction of intertidal bathymetry from video is reported and compared with topographical (d-RTK) field survey performed at Torre Lapilllo (Le), useful also in order to assess the system efficacy and accuracy in coastal area monitoring.

The central side at the embayment of Torre Lapillo has been also involved in different coastal surveys. Among them, an innovative technique, by using Unmanned Aerial Vehicle (UAV) flight, is evaluated. A high vertical accuracy, in solving such a complex topographic system, is found by investigating the DSM and comparing it to traditional GPS surveys. The DSM has been reconstructed by processing the UAV imagery using the Structure from Motion (SfM) algorithm. All the processes involved, from acquisition phase to drawing results, are discussed.

Besides, the new video system is employed on this study area for run-up measurements, performed over several cross-shore transects, by using time-stack images. A methodology useful in order to validate 2-d numerical predicted run-up values with such observations is presented. It is described a high resolution analysis of the interaction of irregular waves with natural beach leading to wave propagation beyond the coastline, swash and vertical run-up excursion, which are numerically predicted. The novel methodology proposed, combines a wide validated forecasting dataset, MeteOcean, with SWAN and SWASH models to achieve accurate and computationally feasible simulation of waves at different time and spatial scales, up to the total energy dissipation in the swash zone. A merging strategy between field surveys for properly resolving topographical input is employed and discussed. The subaerial surface, which is essential for accurate representation of the hydrodynamic interactions with the beach

profile, is solved by employing the DSM UAV-derived. Results by employing such an approach show to be successful, while a proper calibration of the SWASH physical parameters, when the model is applied in 1-d has been necessary. The run-up observations used in this work has been compared with conventional empirical model data. Most of the empirical formulations led to a systematic overestimation, apart from two of them, which take into account transformation processes of the entire nearshore zone.

It shall be mentioned that the work reported in this thesis has been done within the framework of scholarship founded by Ministero dell'Istruzione, dell'Università e della Ricerca (MIUR).

Key words: coastal video monitoring; shoreline evolution; UAV; run-up; SWASH.

ABSTRACT ESTESO

Attualmente, una gran parte delle coste europee è soggetta a processi erosivi, e la costa dell'Italia non rappresenta un'eccezione, anzi essa sta subendo una grave erosione, una delle più visibili conseguenze di un implacabile depauperamento dell'ambiente costiero, particolarmente allarmante dato il cruciale ruolo economico e sociale che oggi esso riveste. In questo senso, per intervenire ai fini della sua stessa protezione e quindi mirare ad attenuare l'irreversibilità delle tendenze erosive, tra le assolute priorità rientra un ben strutturato e continuo programma di monitoraggio delle spiagge, da implementare all'interno di una strategia di gestione costiera lungimirante. In questa prospettiva, i sistemi video rappresentano una soluzione in via di largo utilizzo in tutto il mondo nelle strategie di monitoraggio costiero, dato che permettono un'elevata frequenza di campionamento temporale e spaziale dei processi costieri, con bassi sforzi logistici e costi complessivi.

L'obiettivo principale di questo lavoro di tesi è quello di contribuire allo sviluppo di nuovi strumenti e metodologie idonei ad essere implementate in una più ampia rete di monitoraggio costiera per supportare le attività di pianificazione e controllo regionale.

Un nuovo sistema di video monitoraggio e controllo delle coste pugliesi (Italia del Sud) è stato quindi sviluppato. Nel presente lavoro viene descritta l'implementazione del sistema, orientato ad alcune caratteristiche fondamentali quali la rapida installazione, robustezza, basso costo, efficienza delle fasi di acquisizione e la catena delle elaborazioni dei dati, in particolare attraverso l'installazione di due stazioni. Il progetto del sistema deriva da un principale obiettivo, quello di ottenere uno strumento in grado di operare in maniera completamente automatica. Per questo fine, il tool sviluppato è composto da una serie di routine supportate da un applicativo web, le quali sono finalizzate all'elaborazione di immagini (e.g. estrazione linea di riva e geo-rettifica), all'analisi dei dati e alla condivisione dei dati sullo stato attuale della spiaggia, quindi sulla sua evoluzione, quasi in tempo reale. In questo contesto si è sviluppato un nuovo modello specifico per

l'estrazione automatica della linea di riva, Shoreline Detection Model (SDM). Nella presente vengono descritti l'algoritmo, inspirato ad una formulazione probabilistica dei contorni d'immagine, Global Probability of Boundary (gPb) e ad una segmentazione basata su inseminanti, insieme alle procedure di dettaglio per la elaborazione dei frame. In particolare il modello permette di identificare l'interfaccia sabbia/mare dalla immagini Timex, automaticamente segmentate. Il modello SDM è stato calibrato e validato sui prodotti di un precedente sistema di video monitoraggio, installato ad Alimini (Le) a fine 2005, sulla base del confronto, effettuato su diversi transetti, delle linee di riva manuali ed automatiche. Il modello è stato implementato nel nuovo sistema e quindi, testato sui relativi prodotti (Timex) valutando la sua versatilità ed estendibilità, a parità di coefficienti di calibrazione, in paraggi caratterizzati da morfologia ed esposizione differenti. Ottimi risultati sono stati riscontrati.

In tempo reale perciò le immagini del nuovo sistema e le linee di riva sono caricate in rete e rese fruibili per il download. Inoltre il web-tool permette l'analisi nel tempo della evoluzione stessa della linea di riva, mediante analisi su transetti. La ricostruzione della batimetria intertidale da video, presso il sito di Torre Lapillo (Le), è descritta e confrontata con opportuni rilievi topografici di campo d-RTK GPS, anche al fine di valutare l'efficacia del sistema in queste elaborazioni automatiche.

L'area centrale della baia di Torre Lapillo è stata oggetto di diverse campagne di campo, tra le quali nel presente lavoro, in particolare, vengono descritti una strumentazione e metodi innovativi, mediante utilizzo del drone (UAV). La particolare conformazione topografica tipica degli ambiente costieri, si è dimostrato possa essere ottimamente risolta mediante Modello Digitale di Superficie (DSM), opportunamente ricostruito da immagini UAV, utilizzando l'algoritmo Structure from Motion (SfM). Il DSM è stato oggetto di validazione mediante confronto con rilievi di campo tradizionali (GPS), ottenendo un elevato livello di precisione in elevazione. Tutte le fasi, a partire dall'acquisizione vera e propria fino alla validazione della metodologia, sono qui descritte.

Il nuovo sistema di video monitoraggio è stato implementato in questa stessa area di studio per la raccolta di datti di run-up da onda su diversi transetti cross-shore, utiliz-

zando le immagini time-stack. Un modello ad elevata risoluzione per simulare l'interazione di un campo d'onde irregolari con la spiaggia fino alla risalita stessa delle onde (run-up), viene qui presentato. Una metodologia, utilizzata per la validazione di simulazioni di run-up 2-d con le osservazioni su menzionate, è introdotta. Questa nuova metodologia a partire dai dati di forecast di un modello ampiamente validato, MeteOcean, combina SWAN e SWASH al fine di modellare con grande precisione le onde a differenti scale spaziali, fino alla dissipazione energetica nella swash zone. Viene qui introdotta una strategia per unire differenti dati di campo al fine di costruire l'input topografico dei modelli. La spiaggia emersa, fondamentale per garantire una ottimale rappresentazione dei processi idrodinamici e di interazione, è risolta mediante utilizzo del DSM derivato dal drone. I risultati di simulazione di SWASH, in 2-d, mostrano una ottima correlazione con i dati da video analisi, mentre solo tramite un'opportuna calibrazione dei parametri dello stesso, in analisi 1-d, si sono ottenute stime confrontabili. Infine, i dati di run-up sono state anche confrontati con modelli empirici di letteratura, i quali hanno dimostrato di sovrastimare nella maggior parte dei casi le osservazioni da time-stack. Gli unici modelli in grado di garantire dei risultati confrontabili tengono propriamente in conto dei fenomeni di trasformazione in tutta la nearshore zone.

È doveroso menzionare che il lavoro riportato in questa tesi è stato realizzato nell'ambito di una borsa di studio che rientra nel progetto di dottorato finanziato del Ministero dell'Istruzione, dell'Università e della Ricerca (MIUR), per mezzo del Politecnico di Bari.

Key words: video monitoraggio; linea di riva; UAV; run-up; SWASH.

INDEX

INDEX **7**

General Introduction **10**

Background and motivations *10*

Objectives of the thesis *12*

Thesis outline *14*

Chapter 1 - COASTAL PROCESSES AND MONITORING **19**

1.1. Hydrodynamics of coastal zones *19*

1.2. Numerical modelling approaches *29*

1.3. Coastal areas, erosion and monitoring *36*

Chapter 2 - AUTOMATIC COASTAL IMAGE SEGMENTATION FOR SHORELINE DETECTION **45**

2.1. Introduction *45*

2.2. Coastal video monitoring - background *45*

2.3. Overview of new Shoreline Detection Model *54*

2.4. Main routine *57*

2.5. Calibration and results *71*

2.6. Implementation *77*

2.7. Conclusions 77

Chapter 3 - NEW APULIAN COASTAL VIDEO MONITORING SYSTEM 81

3.1. Introduction 81

3.2. System description 81

3.3. Image acquisition 82

3.4. Geometry of cameras 83

3.5. Image displacement 85

3.6. Sea level filter 87

3.7. System applications 87

3.8. Web-tool 103

3.9. Conclusions 106

Chapter 4 - UNMANNED AERIAL VEICHLE (UAV) APPLICATION FOR BEACH DSM RECONSTRUCTION 111

4.1. Introduction 111

4.2. Study area 113

4.3. Materials and methods 113

4.4. Results 119

4.5. Discussion 124

4.6. Conclusion 126

Chapter 5 - VIDEO ANALYSIS OF WAVE RUN-UP AND NUMERICAL PREDICTIONS WITH SWASH MODEL 129

5.1. Introduction 129

5.2. Measurement from video observations 130

5.3. Numerical approach 135

5.4. Comparison between 1-d and 2-d SWASH simulations 145

5.5. Empirical run-up estimation 155

5.6. Conclusions 158

Conclusions 163

Main Summary and future works 163

References 167

Acknowledgments 181

Curriculum 183

General Introduction

Background and motivations

A high understanding of the morphological and hydrodynamic behaviours of a coastal system and the regular monitoring of its present state is required in order to deal with an effective management of a variety of coastal concerns such as planning constraints, safety, recreation, nature, fishery and other demands. The observation of coastal evolution at time scales of primary management interest, years to decades, could be often blurred by the morphological variability at minor time scales (days to seasons). On the other side, a great research interest is addressed to the nearshore zone, probably the most dynamic region of any coastal environment. For this reason, high-resolution measurement techniques are necessary to resolve small-scale coastal processes at spatiotemporal scales in the order of meters and hours to days, whereas the collection of long-term data sets is of decisive importance to study coastal behaviour, particularly at spatial scales of $1\text{-}100\ km$ and temporal scales of months to decades. So, both researchers and coastal managers would benefit from techniques to monitor coastal evolution with a wide range of spatiotemporal scales. Present-day techniques in order to meet so should primarily satisfy two functional requirements. First, they have to provide data with high time-space frequency and second, they have to be cost-efficient in operation to enable the collection of long-term data sets. In-situ measurement techniques do not often satisfy these functional demands.

Luckily, many nearshore processes have a visible and objective signature at the sea surface, which allow to be studied and monitored remotely. In contrast to in-situ sampling techniques, remote data collection are continuous - and even most informative - during rough wave conditions. Since it represents an indirect measurement, the key issue for every remote sensing technique is the quantitative interpretation of sensed information in terms of relevant physical parameters, like the coastline.
The development of robust, generically applicable and automatic techniques to do so on a routinely basis is sometimes still a challenge. Coastal community is involved more

and more in spreading innovative solutions to managers of coastal and delta areas. In addition, nowadays, a growing trend towards automation and participation has also touched Coastal community, with more companies and research projects aiming to build useful platform/tool in order to share results and solutions to stakeholders.

The erosion phenomena of shoreline at Apulia region, since the quantification determined by the Atlas of the Italian Beaches of the National Research Council (1999) in the 30% of the 30 km of beaches, have served as a warning for the regional public authorities who started to pursue, with the relevant consultation of research communities, the objectives of monitoring and evaluation, with standard methods. Furthermore, in a growing context of increased marine-related social activities and tourism interests, coupled with the perspective of strategic commercial assets, the shoreline recession raises awareness in local community.

With this background and considering the above mentioned limitation and disadvantages of in-situ measurements, the opportunity of developing a new low-cost, effective, completely automatic and generally deployable coastal-video monitoring system has been undertaken. The new video monitoring system (Chapter 3 - New Apulian coastal video monitoring system), installed at two sites allows the monitoring of beaches. Acquisition of long-term high-resolution images of the Torre Lapillo and Torre Canne beaches, particularly focusing on the coastline position and evolution, can support the quantification of morphological changes and subsequently contribute for the sedimentary budget assessment at these coasts. The automation of the processes by including the data provided by local wave/tide network of the regional Basin Authority of Apulia is an optimal improvement of system. The results are allowed to be shared in quasi real-time either for simple web consultation and for download, in order to accomplish the objective of coastal/hydraulic professionals and local community information supports.

Monitoring strategy applied in a diffuse manner around coastal areas by means of video systems could be very exhaustive in order to achieve deep knowledge of local wave and morphodynamic behaviours, but it cannot be always reached because of natural planning limitation, obstacles, etc.

With regard to small temporal-scale processes, one need of coastal managers is to assess the impact of severe/extreme wave events in the immediate aftermath of a storm and hopefully, to be able to predict to some extent the areas most vulnerable to i.e. run-up of swells. The information required for this aim are related mainly to the precise acquisition of wave parameters and the coastal topography. In particular, when both sources are available for several different events, with corresponding observations, models for run-up could be implemented and tuned locally very easily. However, to do so, accurate timely data from field topographical surveys, which include submerged beach, and offshore wave data, from wave buoy close to the study area, have to be implemented.

Within the purpose of a regular coastal monitoring programme being carried out in a region and in order to resolve topographical input for run-up model, Unmanned Aerial Vehicles can replace many of the conventional measurements techniques (LiDAR, TLS, d-GPS), with considerable gains in the cost of the data acquisition and without any loss in the quality of topographic and aerial imagery data. The images UAV-derived allowed detailed DSMs to be contructed with high vertical accuracy over sand areas, which is appropriate to detect even relatively small shape and volume changes in beaches.

While, on the other side, as twofold reasoned, either when no reliable wave data are available and in order to build a modelling chain to be activated under certain circumstances, the potential implementation of largely validated wave forecasting model output to be concatenated with local high-resolute wave-flow model could represent an accurate, rapid, low-cost and effective tool for run-up. Moreover, the availability of observations derived from a coastal video system for a direct comparison allows measuring the quality and analysing the results of such a tool.

Objectives of the thesis

Main objectives of the present thesis are to validate new methods and algorithms developed in the context of the morphological and hydrodynamics coastal remote measurements. The quantification of shoreline position, beach cross-shore length and their

respective evolution based on video processing in low energetic environments, and focus on the hydrodynamics of beach, as vertical run-up modelling of the central stretch of the embayment of Torre Lapillo, through numerical modelling for video monitoring comparison via time-stack, are analysed. The use of an Unmanned Aerial Vehicle (UAV) is employed and the accuracy of a DSM UAV-derived from processing its imagery output is evaluated.

Several detailed objectives can be summarized:

- Analyse the potentialities and disadvantages of other experiences, particularly those at Apulia region, aim at shore video monitoring for morphological analysis.
- Investigate the promise of new video processing procedures in order to be properly embedded as stable and automatic algorithms properly addressed for coastal area implementation.
- Implement a new video monitoring system at two stations. This task includes not only hardware choices and installations, but also software components and all logistics and maintenance addressed at a long-term monitoring set-up.
- Quantify and assess the accuracy of georeferenced point clouds produced via multi-view stereoscopic from Unmanned Aerial Vehicle (UAV) imagery.
- Wave modelling as propagation and swash zone hydrodynamics of nearshore area with SWAN and SWASH.
- Application of sensitivity study to assess the accuracy of SWASH run-up predictions across conditions that have corresponding run-up measurements (time-stack).
- Validate the results of run-up through numerical modelling and empirical models by video time-stack comparison.

Thesis outline

This study covers a range of topics from video monitoring implementation by using nonstandard photogrammetric techniques and computer vision algorithms, shoreline variability, UAV application for topographic environment solving, wave forcing modelling to run-up evaluation, which are structured in 6 chapters:

A *General Introduction,* which represents a description of the thesis motivations, objectives, and overview.

Chapter one, *COASTAL PROCESSES AND MONITORING,* describes the main features under consideration in order to the efforts for the new instruments deployment and algorithms, procedures implementation in order to its monitoring.

Chapter two, *AUTOMATIC COASTAL IMAGE SEGMENTATION FOR SHORELINE DETECTION,* deals with a presentation of the state of the arts in the remote coastal monitoring realized by visible cameras, especially addressed to the shoreline mapping. Then it presents a new algorithm with the efforts in deploying a stable and completely automatic procedure for shoreline detection, without user intervention, realized by means of specialized computer vision algorithms.

Chapter three, *NEW APULIAN COASTAL VIDEO MONITORING SYSTEM,* describes the advances addressed to the implementation of a cheap, effective and completely automatic coastal video monitoring system and the validation of the new algorithms and methods at two new stations in Apulia region.

Chapter four, *UNMANNED AERIAL VEICHLE (UAV) APPLICATION FOR BEACH DSM RECONSTRUCTION,* is addressed to the validation of UAV flight on coastal area in order to reconstruct the beach topography, aiming the implementation of the results as input for hydrodynamic modelling.

Chapter five, *VIDEO ANALYSIS OF WAVE RUN-UP AND NUMERICAL PREDICTIONS WITH SWASH MODEL*, aims to validate numerical model predictions of run-up by using 2-d and 1-d approaches, by means of video time-stack comparison. Empirical formulations are also tested and discussed.

Afterwards, the main remarks and future researches are presented in the *Conclusions* of the thesis, in a separated chapter. Finally, *References* used throughout the

thesis are listed. All the published material is listed in my *Curriculum* at the end of this thesis.

CHAPTER 1
COASTAL PROCESSES AND MONITORING

Chapter 1 - COASTAL PROCESSES AND MONITORING

1.1. Hydrodynamics of coastal zones

Wind waves are generated as a result of the action of the wind on the surface of the water. The wave height, wave period, propagation direction and duration of the wave field at a certain location depend on (i) the wind field (speed, direction and duration), (ii) the fetch of the wind field (meteorological fetch) or the water area (geographical fetch) (iii) the water depth over the wave generation area. So *wind waves*, also referred to as short-crested, are generated and influenced by the local wind field, they are normally relatively steep (high and short) and often both irregular and directional, for which reason it is difficult to distinguish defined wave fronts. Whereas, *swell* are wind waves generated elsewhere but transformed as they propagate away from the generation area. Swell waves are often relatively long, of moderate height, regular and unidirectional. There are many types of wave transformation mainly related to wave phenomena occurring in the natural environment. Particularly, when the waves approach shallower water (i.e. a sandy coast), and the water depth becomes less than about half the wavelength, they are affected by the seabed through processes such as refraction, shoaling, bottom friction and wave breaking. The dissipation processes, such as wave-breaking, attenuate the short period much more than the long period components. This process acts as a filter, whereby the resulting long-crested swell will consist of relatively long (wavelength) waves with moderate wave height. Breaking waves are generally divided into different types, depending on the steepness of the waves and the slope of the shoreface. However, wave breaking also occurs in deep water when the waves are too steep, in the form of white-cups, with different mechanisms. Furthermore, when the waves meet major structures or abrupt changes in the coastline, they will be transformed by diffraction. Moreover, if waves meet a submerged reef or structure, they will overtop them.

Waves do not transport just energy but also momentum. Such momentum transport is equivalent to a stress and horizontal variations in this stress act as forces on the water

and may thus tilt the mean sea level or generate currents. The transport of wave-induced momentum, consisting of normal stresses and shear stresses, is defined as *radiation stress.* The radiation stress generally increases outside the surf zone when a wave approaches the coast and the wave *set-down* occurs. At breaking, the wave energy is dissipated through the turbulence, while the momentum is transferred to the water column, this causes a slope of the water surface in order to balance the onshore component of the momentum flux, which results in a positive tilt of the mean water surface and it corresponds to the wave *set-up*. The set-up depends on the incoming wave height and, if the wave height is stationary, then the set-up will be stationary, too. While, at an actual beach, the waves tend to arrive in groups and the incoming wave height fluctuates more or less periodically with the period of the wave groups. This causes the set-up to fluctuate accordingly, so that the surf zone moves periodically up and down as the wave groups arrive, generating low-frequency waves that travel out to sea. This phenomenon is called *surf beat.*

The above-mentioned wave set-up is only a part of the wave run-up. The latter, defined as the time-varying location of the shoreward edge of water on the beach face (Ruggiero et al., 2004)(Figure 1.1), is often expressed in terms of a vertical excursion consisting of two components: a steady super-elevation of the mean water level, the *wave setup*, and fluctuations about that mean, *swash* (Guza and Thornton, 1982, Holman, 1986, Holman and Sallenger, 1986, Kobayashi, 1999, Raubenheimer and Guza, 1996). Many work on swash zone dynamics essentially focused on the maximal excursion of water on the beach, given the frequency and amplitude of the incident wave train (Brocchini and Baldock, 2008; Holman and Sallenger, 1986). The swash signal could be decomposed into *infragravity* energy component, which dominates the swash signal on highly dissipative beaches and *incident*, predominant on reflective beaches (Ruessink et al., 1998).

Furthermore, estimates of the maximum and exceedance values of *run-up* are still one of the major goals for research in the field of coastal engineering, the interest being related to (i) the increasing availability of field data for predictive purposes (Ruggiero et al., 2004) or (ii) the use of advanced techniques like photogrammetry, topographic data

collection, and digital image-processing techniques, which largely improve its detection capabilities (Boak and Turner, 2005).

Coastal regions are also frequently subject to inundation produced by storms. The prediction of beach inundation during storms involves the accurate prediction of wave run-up, but a crucial influence in the maximum level to which the water travels up a beach or coastal structure is played also by the combination of tides and surges level.

Tides, the periodic rise and fall in the level of the water in oceans and seas, are caused by the result of gravitational attraction of the sun and moon (Simm et al., 1996, Wright et al., 1999). They are very predictable. They are large on the NW European shelf but small in the Mediterranean (Wolf, 2009). While surges, on the other hand, are quasi-periodic and caused by meteorological forcing. The most important mechanism for surge generation is wind-stress acting over shallow water. Observations of tides and surges are generally made at coastal tide gauges, even if these locations are not always ideal because they could experience local effects by being in ports or estuaries rather than reflecting open sea conditions.

The dominance of astronomical tide, surge level and wave run-up depends on site-specific conditions such as tidal range, storminess (exposure to surge levels and waves), the morphology of the continental shelf and the morphodynamic state of the beach.

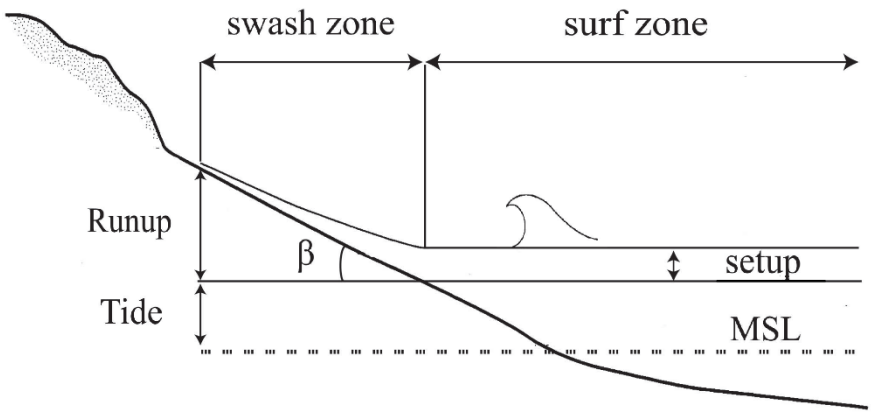

Figure 1.1 Wave run-up scheme, adapted from Peter et al. (2001).

1.1.1. Runp-up measurement

The in-situ measurements of swash processes, including spatial extension of run-up, were often coincident with measurements of sediment movement within the swash zone. Nowadays, they are growing and shifting towards remotely sensed measurements.

The first quantitative analysis of swash excursion were undertaken by using *resistance wires* (Guza and Thornton, 1982, Pitman, 2014). Typically, two electronic resistance wires are elevated to a nominal distance above the bed. The wires ran cross-shore and the swash action running up the profile submerged the wires, shorting out the current path, resulting in different levels of resistance. The wires are calibrated by submerging known lengths in water prior to field deployment (Raubenheimer et al., 1995). In the same way as these horizontal resistance wires are used to measure the spatial extent of swash, efforts in using *pore pressure sensors* buried few cm below the bed in order to monitor the water level and beach topography, are undertaken (Baldock et al., 2008).

While *Pressure transducers* represents an alternative of in-situ deployed instruments for swash depth measurement, and they are often installed in conjunction with other

sensors, such as run up wires for a more continuous dataset. Remotely sensors deployment is growing fast. *Ultrasonic* acoustic sensors mounted on a scaffold frame collecting data of bed level changes have been demonstrated to provide an acceptable performance and applicable to measurements of the swash lens (Blenkinsopp et al., 2016, Blenkinsopp et al., 2011, Turner et al., 2008).

An emerging method for remotely sensing swash and the near-shore uses light- and/or radio detection and ranging, or LIDAR and RADAR, respectively (Pitman, 2014). Both systems work by emitting a pulse and measuring the round-trip time and/or different return phases, hence known directionality of that pulse in relation to a sensor. Some recent experiences highlight the Terrestrial Laser Scanner as new optimal instrument in order to predict wave motion in the swash zone (Almeida et al., 2015, Blenkinsopp et al., 2010), morphological changes on a wave-by-wave basis in the surf zone, in combination with video-oservation (Vousdoukas et al., 2014), wave measurements, run-up heights and overtopping (Hofland et al., 2015, Valentini, 2014).

The spread of video systems for nearshore measurements have also led to the definition of a data sampling schemes designed such to collect time series of pixel intensities: *time-stack*. In the foreshore area, this often correspond to cross-shore transect across a beach face which is used to calculate position of the water's edge, run-up. Among the video-analysis techniques used in this thesis, in Chapter 5 -, this will be treated within a more extensive description.

1.1.2. Empirical models for run-up predictions

If storm surge (wind and pressure surge) can be deduced from the observed tide using tide gauge measurements, estimation of wave run-up is more complicated because of the complex processes driving the swash zone. For this reason, many run-up formulations can be found in the literature, most of them including deep-water significant wave height (H_0) and wavelength (L_0), which is related to the peak period (T_p), and the beach slope (β).

Hunt (1959)) proposed a relation of the run-up values, found proportional to the surf similarity parameter or Iribarren number:

$$\frac{R}{H_0} = \xi_0 \tag{1.1}$$

where H_0 is the average deep water regular wave height, $\xi_0 = \tan\alpha/\sqrt{H_0/L_0}$, $L_0 = gT^2/2\pi$, T the regular wave period and α the measured foreshore slope.

The extension of this relationship, by using time domain analysis of irregular waves, led Battjes (1974) to this formulation:

$$\frac{R_{2\%}}{H_{1/3}} = C_m \xi_{0\mathrm{m}} \tag{1.2}$$

with $C_m = 1.49 - 1.87$, $\xi_0 = \tan\alpha/\sqrt{H_{1/3}/L_{0m}}$, and $H_{1/3}$ the average of the 1/3 highest wave heights and L_{0m} derived from the linear wave theory.

Holman and Sallenger (1986) made a statistical analysis for the 2% exceedance maximum run-up values ($R_{2\%}$) from field data collected on a natural intermediate-to-reflective beach (beach slope $\tan\beta$ from 0.07 to 0.2), by using video images analysis. They found correlations between run-up, and the surf similarity parameter, defined by the significant wave height at intermediate depth, H_{m0}:

$$\frac{R_{2\%}}{H_{m0}} = a\xi_{0\mathrm{p}}^{b} + c \tag{1.3}$$

where, with respect to Hunt formula, Holman (1986) fits this equation with $a = 0.83$, b = 1, and $c = 0.2$.

Predictions based on the foreshore slope dramatically over-estimate run-up while predictions based on the surf zone slope under-estimate the run-up (Mayer and Kriebel, 1994).

Nielsen and Hanslow, (1991) pointed out that beach slope definition in relation to the run-up formulations may cause big differences, since for example at dissipative conditions the difference between the foreshore beach slope and the slope of the surf zone is fairly small, quite the opposite at intermediate to reflective beaches. For this reason, an ideal measure of beach slope should account for both the foreshore and the surf zone. Hunt (1959) suggests, for bi-linear geometries, a weighted average. Over complex geometries Saville Jr (1957) proposed a time-consuming iterative solution in order to implement an hypothetical average or "effective" slope of the entire active surf zone, to be extended between the wave break point and the run-up limit.

An analytical solution (Eq. 1.4) for wave run-up over non-uniform beach profiles is then found and discussed in Mayer and Kriebel (1994), to be given by the solution of a quadratic equation:

$$R = \frac{m}{2}\left(X_b - \sqrt{H_0 L_0}\right)\left[-1 + \sqrt{1 + \frac{4h_b\sqrt{H_0 L_0}}{m\left(X_b - \sqrt{H_0 L_0}\right)^2}}\right] \tag{1.4}$$

where mean run-up is derived from a formulation of the average slope between the incipient breakpoint and the run-up limit, which is defined by:

$$\tan\beta = \frac{R + h_b}{X_R + X_B} \tag{1.5}$$

As depicted in Figure 1.2, the h_b is the incipient breaking depth, X_b is the horizontal distance from the shoreline to the breakpoint, and X_R is the horizontal distance to the run-up limit.

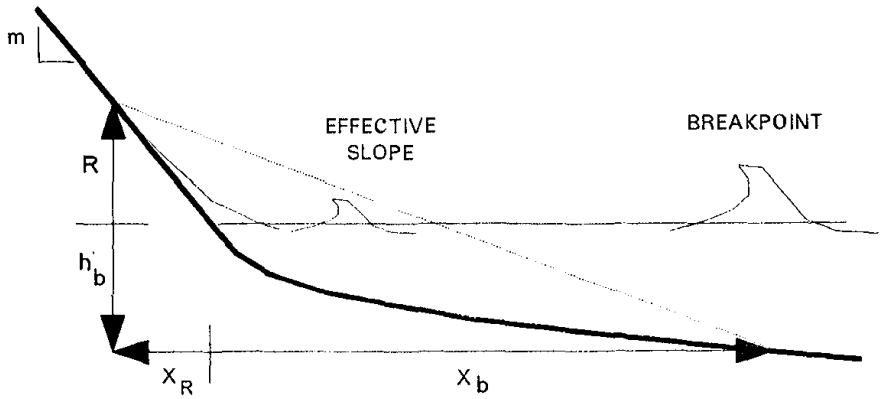

Figure 1.2 Sketch of "Effective" slope (Mayer and Kriebel, 1994).

Mase (1989) proposes a relationship for gentle, smooth and impermeable slopes for irregular wave run-up, based on the laboratory data, distinguishing the statistical run-up expression:

$$\frac{R_{2\%}}{H_0} = 1.86\xi^{0.71} \tag{1.6}$$

$$\frac{R_{max}}{H_0} = 2.23\xi^{0.77} \tag{1.7}$$

$$\frac{\bar{R}}{H_0} = 0.88\xi^{0.69} \tag{1.8}$$

where $R_{2\%}, R_{max}\ and\ \bar{R}$ are respectively the 2% exceedance, maximum and mean run-up.

Nielsen and Hanslow (1991) investigate the run-up values on several natural beaches at New South Wales, in Australia. By assuming a Rayleigh distribution, the subsequent formulations are derived, on the basis of L_{zwm}, see Eq. (1.11), which is the shape parameter, or vertical scale for the related distribution:

$$R_{2\%} = 1.98L_{zwm} \tag{1.9}$$

$$\bar{R} = 0.98 L_{zwm} \tag{1.10}$$

$$L_{zwm} = \begin{cases} 0.05\sqrt{H_{rms} L_0} & \beta_f < 0.1 \\ 0.6\beta_f\sqrt{H_{rms} L_0} & \beta_f \geq 0.1 \end{cases} \tag{1.11}$$

Ruessink et al. (1998) calculated the run-up on highly dissipative beaches, highlighting the dominance of *infragravity waves*, and defining the beach slope within the region of minimum run-down and maximum run-up. A linear relationship was found:

$$\frac{R_s^{ig}}{H_0} = 0.53\,\xi + 0.09 \tag{1.12}$$

Ruggiero et al. (2001), by using video techniques, and aggregating the dataset of Holman and Sallenger (1986), create a model for predisposition of coastal properties to erosion during extreme events. The model account for a run-up expression, in Eq. (1.13), where the foreshore beach slope β_f is defined in the region between two standard deviations from the mean run-up elevation. The formula is:

$$R_{2\%} = 0.27\sqrt{\beta_f H_0 L_0} \tag{1.13}$$

Recently, a synthesis of empirical parameterization of extreme $R_{2\%}$ run-up, based on several natural beach and laboratory experiments (Stockdon et al., 2006), indicate that in an infragravity-dominated dissipative context, the magnitude of swash super-elevation is dependent only on offshore wave height and wavelength. While, it is achieved that for intermediate to reflective condition, combined with complex foreshore morphology, beach slope is on the contrary much more important, particularly for practical applications (Suanez et al., 2015).

In Stockdon et al. (2006) experience, by using video techniques, the β_f is the average slope on a region of $\pm 2\sigma^*$ around the set-up at the shoreline and σ^* the standard

deviation of the continuous water level record. The relative formulation is elaborated differently according to the beach morphodynamic context:

$$R_{2\%} = 0.043(H_0 L_0)^{1/2} \qquad \xi o < 0.3 \tag{1.14}$$

$$R_{2\%} = 1.1\left(0.35\beta_f (H_0 L_0)^{\frac{1}{2}} + \frac{[H_0 L_0(0.563\beta_f^2 + 0.004]^{\frac{1}{2}}}{2}\right) \tag{1.15}$$

$$< 0.3 < \xi o < 1.25$$

$$R_{2\%} = 0.73\beta_f (H_0 L_0)^{1/2} \qquad \xi o > 1.25 \tag{1.16}$$

Vousdoukas et al. (2009) compare run-up video observations on microtidal pocket beaches on Eastern Mediterranean with the predicted ones using mainly Douglass, (1992), Holman, (1986), Peter et al., (2001) structured empirical relations, and the results did not match, with the exception of Stockdon et al. (2006) formulation. Reasons are traced back to swash zone sedimentology and/or the nearshore bed morphology (Vousdoukas et al., 2009) not well accounted in those formulations.

While applying same run-up extraction methodology on mesotidal reflective beach, Vousdoukas et al. (2012) add some additional terms depending on shore-normal wind speed component, U_{wx}, and the tidal water-level variations relative to mean sea level, η_{tide} for a new run-up parametrization:

$$R_{2\%} = 0.503\beta_f (H_0 L_0)^{1/2} + 0.878\xi\sqrt{\frac{H_0^3}{L_0} - 0.016U_{w,x} + 0.188\eta_{tide} + 0.457} \tag{1.17}$$

Roberts et al. (2010) found the both formulations of Holman (1986) and Stockdon et al. (2006) under predict and over predict the run-up considerably if erosion or accretion, respectively takes place. They did not include the bed slope in their analysis, justifying it with the assumption it is difficult to be measured and depends on the wave properties. The only variable they assumed is the breaking wave height:

$$R_{max} = H_b \tag{1.18}$$

Considering a study of run-up on beaches characterized by long wave periods, Mather et al. (2011) highlighted the importance of using not only the foreshore slope, but also the bathymetric profile until around the closer depth. The formulation is the following:

$$R_{max} = CH_oS^{2/3} \tag{1.19}$$

where S acts as a representative nearshore slope, and C a dimensionless coefficient which takes into account the beach morphology. Their model based on Eq. (1.19, is supported with C = 10 for open beaches, while required an adjustment of the coefficient for large embayments where C = 9 and small embayments, C = 6.

Douglass [45] proposed an independent beach slope relationship for evaluating the maximum run-up, Eq. (1.20):

$$\frac{R_{max}}{H_0} = \frac{C_1}{\sqrt{H_0 L_0}} \tag{1.20}$$

where C_1 is equal to 0.12, calibrated as an empirical coefficient with Holman's data.

Results of wave run-up parameterizations against extensive field data from the European Atlantic coast are not so diffuse and since the climatic and tidal conditions, hence the wave climate and the geological history may vary significantly among continents and sites (Vousdoukas et al., 2012), it still demands further investigation.

1.2. Numerical modelling approaches

The estimation of the wave height distribution, wave directions, periods and typical coastal wave parameters, are always of importance for questions in coastal engineering for monitoring purposes particularly, and since late '40 a great effort in their prediction and calculation has been invested. In particular, the propagation and dissipation of water waves can be simulated with the aid of two classes of mathematical models:

- *Phase-resolving models* where the sea surface is resolved, i.e. the surface is covered with a grid which is fine compared with the wave length, and the gridded values of the vertical displacement $\eta(x, y, t)$ are computed.
- *Phase-averaged models* for which the statistics of the sea surface is computed, i.e. on points of a grid the action or energy spectra are computed.

Spectral wave models can account for most of the important processes, which govern the evolution of random wind waves, hence they can be used for the simulation of the sea-state in larger areas. Starting with first-generation models, the implementation of fully discrete third generation spectral models (WAM (Group, 1988), WAVEWATCH III (Tolman, 1997)) has been actually reached (Akpınar et al., 2012). With the introduction of models, such as SWAN, the theory has been further extended to account for the processes in shallow water, such as shallow water *wave breaking* and near-resonant *nonlinear interactions*, which make this class of models an interesting approach also in the nearshore region for lots of coastal engineering applications. The SWAN model became, as a free source code, a standard tool and has been successfully applied to different coastal engineering applications where it shows its ability to hind-cast the shallow water physics with reasonable results (Rogers et al., 2007, Rusu et al., 2008).

A limitation in the model size has to be accounted for the *Phase-resolving models* because the computational grid has to be fine enough to resolve the relevant wave lengths. The actual limitation depends on the type of model used. There are time-dependent models in this category, and stationary models in which the wave motion is purely periodical. With respect to more traditional Boussinesq model which had a limitation related to the depth (recent research relaxed this limit to a certain extent), the three-dimensional model, such as SWASH, recently developed (Zijlema et al., 2011), resolves also the vertical length.

In the following the MeteOcean, SWAN and SWASH models to describe the waves until the shore, including the surfing zone are described, motivated by the approach used in Chapter 5 -. In fact, to simulate waves from the offshore zone until shore, numerical simulations with nesting schemes have been run. The basic idea is to use MeteOcean

forecast database for nesting in the SWAN model rather than feeding it directly into the SWASH model. The reason for that was the known ability of the SWAN model to generate accurate shallow water spectral wave conditions for SWASH. In this way, we achieve the good representation of the wave processes on global, meso and fine scales.

The model features and in Section 5.3, the employed implementations, are described, focusing more on the model SWASH, as it is less known than the WAVEWATCH III and SWAN models.

1.2.3. MeteOcean

The numerical modelling chain employed in the operational MeteOcean (Besio, 2012) forecasting system, whose outputs are employed in this study, consists of an atmospheric model for downscaling wind and atmospheric fields and a third-generation model for wave generation and propagation in the Mediterranean Sea. The non-hydrostatic mesoscale model Weather Research and Forecast, WRF-ARW (Skamarock et al., 2005) is implemented for the atmospheric model simulations, which provide mainly the 10-m wind fields that drives the WWIII (Tolman, 2009).

The computational domain, made by $328 * 265$ points, covers the whole Mediterranean with horizontal resolution of about $10\ km$ and a nested grid size of $2\ km$ for Northern Thyrrhenian Sea (Mentaschi et al., 2015).

WAVEWATCH III™, the wave model implemented in MeteOcean, solves the random phase spectral action density balance equation for wavenumber-direction spectra. The implicit assumption of this equation is that properties of medium (water depth and current) as well as the wave field itself vary on time and space scales that are much larger than the variation scales of a single wave (NOAA, 2013). The sum of source terms consisting of the transfer of energy from the wind field to the waves through mainly a wind-wave interaction term (S_{in}), the dissipation due to wave breaking (S_{ds}) and the nonlinear interactions between waves (S_{nl}) controls the evolution of the wave field in

the model. The regular grid employed covers the whole Mediterranean Sea with a resolution of $0.1273° \times 0.09°$, corresponding to approximately 10 km at a latitude of 45°N (Mentaschi et al., 2015).

The wave model is forced with the wind fields modelled by the atmospheric model with an hourly time step. The output is recorded hourly at all points on the computational grid to determine the integrated quantities (H_s, T_m, θ_m), whereas the wave spectra are stored and interpolated on the locations at choice. The model has been developed and validated on 32-years hindcast, by using records from Rete Ondametrica Nazionale (RON), Red Exterior (REDEXT) buoys and a set of buoys from the Greek Poseidon network. Globally speaking, in the Ionian Sea, characterized by longer fetches, with respect to Adriatic or Aegean Seas, a reliable estimate of the average significant wave height is undertaken. Particularly, for the Ionian Basin where the model is used as input for simulations (see Section 5.3), over a sample size of $72{,}082$, the Normalized Bias (NBI), defined as $\sum(S_i - O_i)/\sum(O_i)$ (where S_i and O_i are simulations and observations, respectively), for the aggregated parameters $H_m, T_p\ and\ \theta_m$ are calculated equal to $-0.29\%, 4.72\%$ and 0.94%, respectively (Mentaschi et al., 2015).

1.2.4. SWAN

Over the past two decades, a number of advanced spectral wind-wave models, known as third-generation models have been developed. The essence of a 3G model is the absence of restrictions on the spectral shape and that it is fully determined by the source terms. The SWAN model has been widely used all over the world from coastal engineers in many coastal wave studies, especially because of its ease of use and its unconditionally stable numerical scheme.

The SWAN model is a third-generation wave model that computes random, short-crested wind generated waves in coastal regions and inland waters. This model was developed by the Environmental Fluid Mechanics Section of the faculty of Civil Engineering and Geosciences at the Delft University of Technology (Booij et al., 1996).

Such a spectral wave models compute the evolution of wave action density $N = E/\sigma$, where E is the variance density and σ the relative radian frequency. For small-scale coastal application, the spectral action balance equation could be expressed in Cartesian coordinates as:

$$\frac{\partial N}{\partial t} + \frac{\partial}{\partial_x}(c_x N) + \frac{\partial}{\partial_y}(c_y N) + \frac{\partial}{\partial_\theta}(c_\theta N) + \frac{\partial}{\partial_\sigma}(c_\sigma N) = \frac{S_{tot}}{\sigma} \qquad (1.21)$$

with

$$c_x = c_{g,x} + U_x; \qquad c_y = c_{g,y} + U_y \qquad (1.22)$$

In the Equation (1.21), on the left side, the first term represents the rate of change of action in time and the second and third terms represent the propagation of action in geographical space (x, y). Then, the fourth and fifth terms represent the frequency shift and refraction induced by depth and currents, respectively. The right-hand side term S_{tot}, of the action balance equation, represents the effects of generation, dissipation, and non linear wave–wave interactions.

Six terms are representative of corresponding processes which contribute, in shallow water, to the S_{tot}:

$$S_{tot} = S_{in}(\sigma,\theta) + S_{dis,w}(\sigma,\theta) + S_{dis,fr}(\sigma,\theta) + S_{dis,br}(\sigma,\theta) + S_{nl3}(\sigma,\theta) + S_{nl,4}(\sigma,\theta) \qquad (1.23)$$

In general, the transfer of wind energy to the waves is well described with the resonance mechanism due to (Phillips, 1957) and feed-back mechanism (Miles, 1957). The former contributes to the initial stages of wave growth and varies linearly with time, the expression of Cavaleri and Rizzoli (1981) is typically assumed. The latter (feed-back mechanism) can be distinguished by its exponential growth, which becomes dominant if some wave energy is present, and the corresponding expressions are given by Komen et al. (1984), rescaled in terms of friction velocity, or Janssen (1989).

The dissipation term of wave energy is represented by the sum of mainly three different contributions: white capping, bottom friction and depth-induced breaking. The white-capping formulations are based on a pulse-based model (randomly distributed pressure pulses) of Hasselmann (1974), with a number of alternative expressions proposed to improve the accuracy of SWAN. The interaction between the surface waves and the bottom is modelled in SWAN by the dissipation of wave energy process due to the bottom friction and could be estimated based on the empirical JONSWAP formulation (Hasselmann et al., 1973), the eddy-viscosity model of Madsen et al. (1988), or the drag law model of Collins (1972). The process of depth-induced wave breaking is still poorly understood and low knowledge is about its spectral modelling. In contrast to this, the total dissipation (i.e. integrated over the spectral space) due to this type of wave breaking can be well modelled with the dissipation of a bore applied to the breaking waves in a random field. A spectral version of the bore model of Battjes and Janssen (1978) that conserves the spectral shape is used with $\alpha = 1$ and $\gamma = 0.73$.

On deep water, SWAN models the transfer of the inner energy by means of four-wave (or quadruplet) interactions and in shallow water by means of three-wave (or triad) interactions.

The integration of the action balance equation is implemented in SWAN with a finite difference schemes in the dimensions of time, geographic space (x, y) and spectral space (σ, θ). An iterative sweep mechanism is used for solving numerically the equations cast in an implicit scheme. Moreover, the SWAN model has also no Courant number limitation like WAM or WAVEWATCH. Therefore, it is able to efficiently cope with small spatial resolutions in coastal applications.

1.2.5. SWASH

The SWASH model, introduced in Zijlema et al. (2011), is a general-purpose numerical tool for simulating non-hydrostatic, free-surface, rotational flows and transport phenomena in one, two or three dimensions. It provides a general basis for simulating wave transformations in coastal waters and agitation in ports, complex changes in rapidly

varied flows, even large-scale ocean circulation and storm surges. This recently released model is developed at the TU Delft and it is available as open source in the "sourceforge" webpage http://swash.sourceforge.net/, it is still in developing process. The current version is 3.14AB.

The governing equations are the nonlinear shallow water equations (NLSW) including non-hydrostatic pressure in horizontal momentum equations, with optionally conservative transport of temperature, salinity and suspend sediments. The model uses second order finite difference method, in explicit mode, for staggered grids, whereby mass and momentum are strictly conserved at a discrete level. This simple and efficient scheme is able to track the actual location of incipient wave breaking. The momentum conservation enables the broken waves to propagate with a correct gradual change of a form and to resemble steady bores in a final stage. The Prandtl mixing length hypothesis models the energy dissipation due to the turbulence generated by wave breaking (Guimarães et al., 2015).

The depth-averaged, non-hydrostatic, free-surface flow, described by NLSW, can be derived from the Navier-Stokes equation for an incompressible and inviscid fluid with constant density ρ_o:

$$\frac{\partial \eta}{\partial t} + \frac{\partial hu}{\partial x} + \frac{\partial hv}{\partial y} = 0 \tag{1.24}$$

$$\frac{\partial u}{\partial t} + u\frac{\partial u}{\partial x} + v\frac{\partial u}{\partial y} + g\frac{\partial \zeta}{\partial x} + \frac{1}{h}\int_{-d}^{\zeta}\frac{\partial q}{\partial x}dz + c_f\frac{u\sqrt{(u^2+v^2}}{h}) = \frac{1}{h}(\frac{\partial h\tau_{xx}}{\partial x} + \frac{\partial h\tau_{xy}}{\partial y}) \tag{1.25}$$

$$\frac{\partial v}{\partial t} + u\frac{\partial v}{\partial x} + v\frac{\partial v}{\partial y} + g\frac{\partial \zeta}{\partial y} + \frac{1}{h}\int_{-d}^{\zeta}\frac{\partial q}{\partial y}dz + c_f\frac{v\sqrt{(u^2+v^2}}{h}) = \frac{1}{h}(\frac{\partial h\tau_{yx}}{\partial x} + \frac{\partial h\tau_{yy}}{\partial y}) \tag{1.26}$$

where t is the time, x and y are located at the still water level and the z-axis points upwards. $\eta(x, y, t)$ is the surface elevation measured from the still water level, $d(x, y)$

is the still water depth, or the downward measured bottom level, $h = \eta + d$ is the total water depth, $u(x, y, t)$ and $v(x, y, t)$ are the depth-averaged flow velocities in x- and y-directions, respectively. $q(x, y, z, t)$ represents the non-hydrostatic pressure (normalized by the density), g is the gravitational acceleration, c_f is the dimensionless bottom friction coefficient, and $\tau_{xx}, \tau_{xy}, \tau_{yx}$ and τ_{yy} are the horizontal turbulent stress terms.

For a proper representation of the interface of water and land, a simple approach is adopted that tracks the moving shoreline by ensuring non-negative water depths and using the upwind water depths in the momentum flux approximations.

1.3. Coastal areas, erosion and monitoring

The previous sections introduces the wave transformations over a coastal profile and how these processes generate wave induced set-up, or currents. These hydrodynamic conditions will result in the movement and transport of sediments, which may results in beach profile changes. Two main transport components are typically recognized, perpendicular and parallel to the coast; actually, the cross-shore transport is the main responsible of beach morphological evolution. Littoral zone can be described as that portion of the coastal profile where the sediments could be transported by wave action. Sandy beach and nearshore zones extend from the limits of wave action on the beach backshore, offshore to the limit of the movement of sand on the bed by waves (Masselink et al., 2014). The nearshore zone can be described as incorporated in the littoral zone between the low tide line and the offshore limit of wave action on the bed and the beach which lies landward of this. The swash zone represents a very dynamic zone of the shore experiencing large levels of sediment transport, turbulence and great rates of morphological changes from the short term (swash-to-swash scale) to longer term events (tidal cycle). Swash zone flows are of fundamental importance not only because of the effective local effects, influencing beach face morphology, longshore sediment transport, overwash and overtopping of barrier islands and coastal defence structures, etc. but also because they can affect the surf zone dynamics as a whole.

In many cases, coastal engineering problems can be expressed in terms of sediment transport-related problems. In particular, the littoral drift budget is decisive for natural coast erosion or accretive processes and for understanding impacts of man-made structures, existing or planned. The shoreline classification is also important for understanding the morphological features of the coastal area and for evaluating the most suitable protection work.

Coastal areas are continually changing, shaped by the dynamic interaction results of the processes between the two major natural systems (sketched in Figure 1.3). In addition to its hydro and morphological importance, the coastal areas are important from a human perspective. For instance, more than half of the US population lives within 80 kilometres of the shoreline and beaches are nowadays one of the top recreational destination for domestic and foreign tourists (Thornton et al., 2000) and, almost half of the European population lives within 50 km of the sea (Fragakis, 2002). These areas are

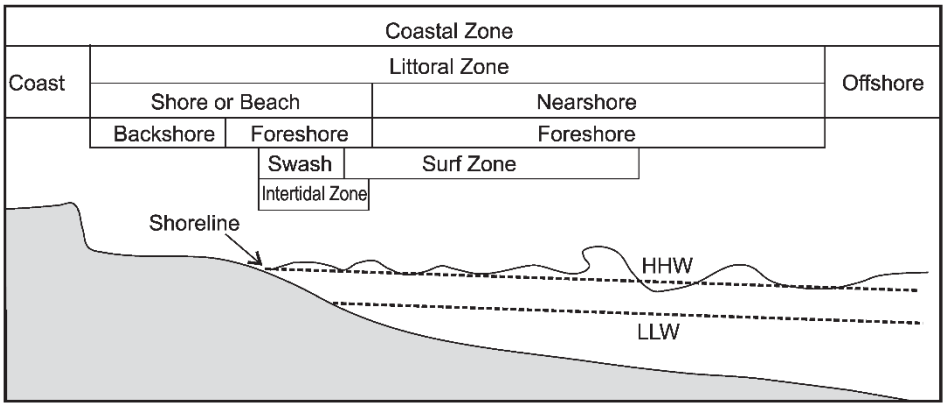

Figure 1.3 Sketch of coastal area and the description of the more representative components (after (Masselink et al., 2014)).

high vulnerable systems due to the careful balance between the human development on the coast and coastal stability itself, in order to guarantee overall coast protection. The exploitation of the coastal zone requires a depth understanding of the best resources to use and a constant monitoring within environmental forces. The main objective would consist into a planning strategy of coastal zones utilization so that negative consequences from interaction between the activities and the natural processes

are minimized. The dynamic nature of these processes could be expressed in terms of coastal accretion and erosion, of morphological mobility of dune areas, tidal inlets and in term of risk of flooding.

Coastal erosion is the process of wearing away material from a coastal profile due to imbalance in the supply and export of material from a certain section. It takes place in the form of scouring in the foot of the cliffs or dunes or at the subtidal foreshore.

Coastal erosion takes place mainly during strong winds, high waves and high tides and storm surge conditions, and results in coastline retreat and loss of land (Mangor, 2001). It is a very complex mechanism and it depends on the off and on-shore environment, wave energy and direction, weather and climate, also including the materials characterizing the coast and the supply or extraction of sediments, as well as the influence of manmade structures (Archetti and Zanuttigh, 2010). Since the 1980s, erosion is widely considered the main process acting on the coasts of the Earth. Coastal erosion, defined as the amount of shoreline retreat for a given coast is frequently evaluated in different manners according to both the researchers and the methods (Delle Rose, 2015).

Italy's coast has been facing an erosion phase from the mid XIX century, due to impacts from changes to land use and rivers (quarrying and damming). The law has been tackling shore protection since 1907. Today around $42\ \%$ of beaches are retreating with the highest rates at deltas. Hard defence dates back to Roman times and has been the preferred strategy since, but innovative approaches are being tested and put into practice. Soft strategies, e.g., nourishment (Damiani et al., 2011), are increasingly used, especially in tourism areas. Responsibility for Coastal Management and protection is decentralised, as it shifted from national to regional governments in 1989 (Pranzini et al., 2015).

Coastal managers have to deal with the coastal erosion management. Specifically, some of the most significant problems facing coastal managers can be grouped and traced back to data with limited spatial/temporal resolution and coverage, complex data

models from scientific community of difficult interpretation and also, insufficient understanding of coastal systems. Beach surveys are required, for example, for monitoring shoreline evolution (erosion and accretion); however, for any kind of logistical and economic reasons, these surveys are usually only possible once or twice a year at best, like Italian Authority of Basin's practices in Italy. Moreover, they are often not effectively well distributed or the corresponding results do not take appropriately into account the seasonal variability, etc. While, well/structured monitoring of beaches provides important information about the state of the coastal system. Furthermore, data from monitoring could provide the input into the statistical descriptors Coastal State Indicators (Davidson et al., 2007) and numerical models of beach behaviour. In the field of shoreline management, for example, monitoring must be driven by the need to provide appropriate data and several stages may be related in this process:

- Understanding the past: short-term fluctuations and long term trends in dune-beach evolution need to be identified to understand the present and predict the future.
- Identifying potential problems: monitoring allows significant change to be identified so that a reasoned response can be developed and implemented, (i.e. dune erosion may lead to damage to an important backshore asset).
- Predicting the future: past and recent developments along the shoreline are a guide to the future evolution.
- Monitoring management operations: feedback on beach-dune response to operations will guide future management, possibly suggesting refinements or alternatives.
- Calibrating or validating physical and numerical models.

Hence, regular monitoring of coastal areas, assessment of their morphodynamics and identification of the processes influencing hydrodynamic or sediment transport are increasingly important for a better understanding of changes and evolutionary trends in coastal systems. This demands a multi-disciplinary approach involving researchers with expertise in coastal processes and state-of-the-art observation technologies.

1.3.6. Shoreline definition and detection

As introduced in previous section, the analysis of shoreline variability and shoreline erosion-accretion trends is crucial to a broad range of investigations undertaken by coastal scientists, coastal engineers and managers. An idealized definition of *shoreline* in coastal engineering is associated to the physical interface of land and water (Dolan et al., 1991). Despite its apparent simplicity, this definition is in practice a challenge to apply. In reality, the shoreline position changes continually through time, because of cross-shore and alongshore sediment movement in the littoral zone and especially because of the dynamic nature of water levels at the coastal boundary (e.g., waves, tides, groundwater, storm surge, setup, run-up, etc.). The shoreline must obviously be considered in a temporal sense, and the time scale chosen will depend on the context of the investigation. Moreover, alongshore variation is quite important and has to be considered for the definition of the shoreline (Camfield and Morang, 1996, Douglas et al., 1998). The need of a *shoreline indicator* is useful for the definition of a feature to be used as a proxy to represent the “true” shoreline position.

Two main classes of shoreline indicator are well summarized in the work by Boak and Turner (2005): (i) visually discernible coastal feature and (ii) a tidal datum-based shoreline indicator determined by a coastal profile and specific vertical elevation (e.g. MWL, MHW, MSL, etc.). Into the main two classes, different instrument and methods are used. Moreover, stand the investigation purposes, and hence, the sampling frequency of the measurements, the available data sources in order to determine the shoreline position change.

The *historical oblique photographs* represents the first background source of information. Many disadvantages could be related mainly to the lack of ground control points (GCPs), absence of time-related metocean data. Hence, only qualitatively advantage regarding the evidence of special morphological features can be extracted.

Historical coastal maps propose a good representation of large spatial coverage shoreline data. Unfortunately, the temporal coverage of this data source is bounded, and lots

of potential errors can be associated to datum changes, different surveying standard, projection errors, etc. (Anders and Byrnes, 1991).

Aerial photographs with manual detection can be accounted as one of the first method useful for visually defined coastal feature and led to the definition of several types of *indicator.* Among others, they are based on man-made structure delimitation, like as landward edge of shore protection structure (Moore et al., 1999); morphological feature, such as the seaward dune vegetation limit (Priest, 1999; Komar et al., 2001) or erosion scarp (Stafford and Langfelder, 1971); and those based on position of selected waterline (i.e. high-tide HWL), such as the location of the wet and dry beach interface (McBride et al., 1991), zone of high-pixel brightness variance (Shoshany and Degani, 1992). With such a method, a good spatial coverage is easily ensured, while temporal coverage is site specific. It is generally assumed the shoreline *indicator* to have been associated with some type of visibly discernible feature.

Beach surveys along cross-shore transects can be treated as an accurate sources of shoreline, by interpolation of a discrete series of profiles. Alongshore accuracy tend to decrease with the relative transect spacing. A datum-based shoreline indicator is associated to this database.

The kinematic differential *GPS* mounted on four-wheel vehicle is an optimal alternative in order to supply for high spatial precision information. The GPS accuracy and the operator precision represent the main drawbacks.

The advances in *remote sensing* and geographical information system (GIS) techniques are overcoming the difficulties in extraction of shoreline position and calculation of shoreline changes (Aedla et al., 2015, Bruno et al., 2016). The main limitations of this data source to coastal investigations can be associated to the pixel resolution and cost. Nowadays, both drawbacks are going decreasing.

On the contrary, with the spreading of *land-based image stations* and image-processing advances, temporally dense even spatially limited data sets can provide an objective shoreline, with repeatable, scientifically valid approach and automatable. Cost and higher resolution make this approach more performing (Aarninkhof et al., 2003).

In the second class can be mentioned the measurement of Tidal datum-based MHW superimposed on a digital terrain model of the subaerial beach based on Stereo pair of aerial photographs (Parker, 2001), survey data (List and Farris, 1999) or LiDAR (Stockdon et al., 2002).

CHAPTER 2

AUTOMATIC COASTAL IMAGE SEGMENTATION FOR SHORELINE DETECTION

Chapter 2 - AUTOMATIC COASTAL IMAGE SEGMENTATION FOR SHORELINE DETECTION

2.1. Introduction

Coastal management retains a crucial importance in order to shape the economic and social assets, especially for places with large sea resources. To accomplish such an evidently powerful scope, coastal monitoring operating surveys have been established to represent a priority stage, in order to collect data useful for the study of hydrodynamic processes and morphological evolution, as well as defence or mitigation works effects and efficacy. Specifically, in order to facilitate measurements of beach evolution and response to storms, anthropic factors involving nourishments and dredging (Kroon et al., 2007), primary variables to be monitored are the shoreline position and topo-bathymetric shore data. In the framework of shoreline monitoring via video analysis, some methods have been proposed, which will be presented in Subs. 2.2.2.

This chapter presents a new algorithm developed to automatically extract shoreline from Timex images, providing a base model for calculation of shoreline evolution and cross-shore profiles.

2.2. Coastal video monitoring - background

During the last two decades, remote sensing video system has acquired a great confidence among the monitoring techniques. The frequency inadequacy of measurement of shoreline position and its time variability, using i.e. cross-shore profiles surveys and aerial photographs, makes the land-based video platforms and the digital image-processing techniques optimal instruments to derive objective shoreline detection methods. The reliability, accuracy and versatility of the coastal video systems have been tested and reviewed in scientific literature (Davidson et al., 2007).

With respect to traditional procedures, video monitoring represents an alternative method to acquire long-term and continuous information, which can be easily stored

and shared in real time, with a larger temporal and spatial sampling frequency. Moreover, the installation costs for coastal video stations are becoming lower, so researchers and managers are engaging throw the variety of applications derived for several scopes.

In the 90's the video monitoring techniques suffered important developments by the Coastal Imaging Laboratory (CIL) at Oregon State University by means of video and image processing tools directed to the monitoring and measuring of the morphodynamic changes and the physical processes acting on littoralo, which resulted on a worldwide network of video-cameras, the ARGUS monitoring system.

Beach video monitoring has the advantage to be a cheap, continuous and automatic technique for data acquisition of the visible littoral phenomena along large periods. Although images can be obscured by fog and rain during storms, it provides important information before and after storms (Smith and Bryan, 2007), with spatial and temporal scales suitable for the beach physical processes, providing an higher resolution remote detection technique, and for morphodynamic monitoring, over large periods.

The major disadvantages of video monitoring systems are the impossibility of data acquisition during the night and the variable linear scale factor along the image, inherent to the oblique acquisition geometry, which reduces the accuracy further away from the camera (Smith and Bryan, 2007).

Acquisition and storage of continuous video streams of long-term data is very consuming for remote sites, while return of a few images or image products represents a sharp compromise (Holman and Stanley, 2007b). Whereby, among the main products, there is the *Snapshot*, which represents an instantaneous overview of the beach state for simple data comparison and inspection, traditionally collected with frequency of half, one or three hour. Time-averaged (*Timex)* images, since the first application at time of first Argus systems, create an averaging of snapshots collected. They are obtained by processing and superimposing snapshot images over an acquisition cycle. This process is therefore an excellent instrument to eliminate random sea conditions and variability in wave run-up and swash. Long time series of timex and day-timex images have provided excellent, low-cost datasets of morphodynamic variability over time

scales from days to decades (Holman and Stanley, 2007b). Variance images are generally stored and presented in terms of standard deviations (*SIGMA*) rather than real mathematical variances (the shorter name is often retained for convenience): temporal windows between 5 and 30 min are used, same for Timex.

Apart from images themselves, time series of pixel intensities can be sampled along a cross-shore transect or an alongshore array, which are useful to produce *time-stack* images. Time-stack images become important to stock information on beach morphodynamic characteristics, the variation in cross-shore direction, run-up and swash.

Since the first technique was introduced to remotely measure scales and morphology of natural sand bars (Lippmann and Holman, 1989), a spreading of investigation algorithms has been attempted for a large range of coastal and marine parameters estimation. Among others, foreshore beach slope estimation (Plant and Holman, 1997), wave empirical and statistical parameterization of run-up (Melby et al., 2012, Simarro et al., 2015, Stockdon et al., 2014, Stockdon et al., 2006), directional wave number, spectra estimation (Plant et al., 2008), nearshore bathymetries and data-assimilation for forecasting analysis (Holman et al., 2013, Van Dongeren et al., 2013) have been accomplished. Moreover, the applicability of these camera platforms has been extended within the context of swimming safety and current predictions (Radermacher et al., 2014, Sembiring, 2015) and for management purposes and coastal state indicators development (Jimenez et al., 2007, Kroon et al., 2007).

2.2.1. Image geo-referencing

In order to provide quantitative information, images need to be undistorted and projected over a projected coordinates system.

When a 3d area is captured by a camera or a webcam, it has to be projected onto a 2d plane. By using photogrammetric transformation it is possible to relate 3d real world coordinates, which are described as (X, Y, Z), and image coordinates, indicated by (u, v).

This procedure for geo-referencing can be used with a distortion free lens and square image pixels. In practice, video-observed pixel locations generally retain at least a radial distortion Δr with respect to the theoretically rectangular pixel grid (u, v), while individual pixels may be slightly non-square as a result of small differences in sampling frequency between the camera and the image acquisition hardware. Hence, the raw video images need to be corrected for pixel non-squareness, radial and tangential lens distortion (internal calibration). Introduced with the cheap pinhole cameras (late 20th century), the pinhole camera model (Figure 1.3) describes the mathematical relationship between the coordinates of a 3D point and its projection onto the image plane,

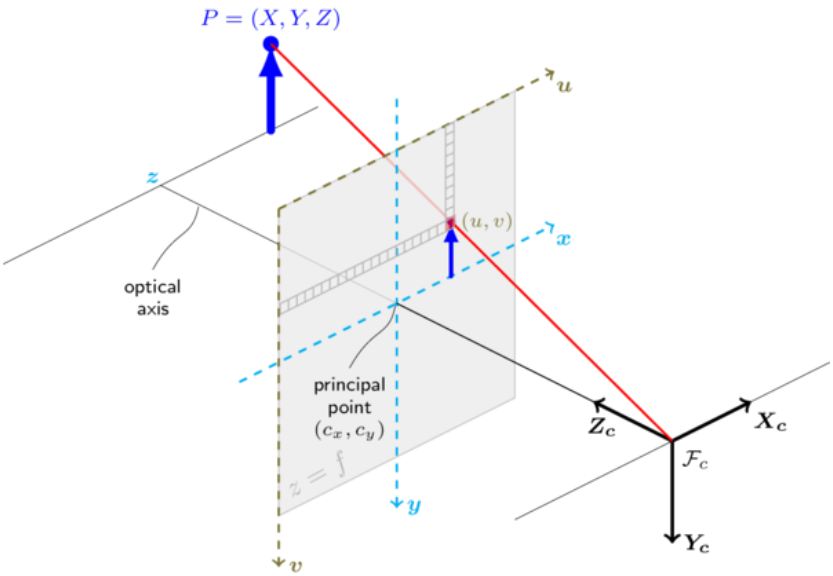

Figure 2.1 Sketch of a Pinhole camera model (OpenCV interpretation)

where the camera aperture is described as a point and no lenses are used to focus light. The model does not include, for example, geometric distortions or blurring of unfocused objects caused by lenses and finite sized apertures. This means that the pinhole camera model can only be used as a first order approximation of the mapping from a 3d scene to a 2d image. Its validity depends on the quality of the camera and, in general, decreases from the centre of the image to the edges as lens distortion effects increase. Standard photogrammetric procedures enable the transformation from (u, v)

to (X, Y, Z), to be computed by means of the collinearity equations (Aarninkhof, 1999, Silva et al., 2009). Direct Linear Transformation (DLT) is often used for this task, since one of the most important advantage is that the parameters can be estimated using the linear least squares technique or singular value decomposition (SVD). A set of reference points, called Ground Control Points (GCPs) with known image and real world coordinates are used for solving the unknowns, once cameras are installed.

A geometry solution is found with this external calibration, hence geo-rectification procedure could be applied, by assuming the real world z-coordinate to be constant, preferably at the measured tidal level (Aarninkhof et al., 2003).

The intrinsic calibration is normally conducted by using laboratory calibration prior to the field installation, accounting for non-squareness, radial distortion and tangential distortion (Silva et al., 2009). In order to overcome drawbacks due to already installed webcams, this task could be also performed together with the external calibrations by using regularization algorithm on DLT (Brignone et al., 2012) or by means of the Levenberg–Marquardt method (Pérez Muñoz et al., 2013).

2.2.2. Shoreline detection models overview

The shoreline detection through the identification of the water/sand interface in the video images allows the quantification of the shoreline evolution in large temporal scales (years) through small scales (seconds). Moreover, by including the shoreline detection along a tidal cycle, together with the sea level measured or estimated, allows the automatic mapping of intertidal bathymetry. In the framework of shoreline movements monitoring, some methods have been proposed, each of them requiring identification of shorelines whose appearance characteristics varies as far as the beach morphodynamics environment.

From earlier studies (Plant and Holman, 1997), the white band pattern discernible from the Timex grayscale images, corresponding to the shore-parallel swash motions, has been identified and defined as the the ShoreLine Intensity Maximum (SLIM). The algorithm is applied by fitting the normalized intensity cross-shore profiles with a quadratic

polynomial, whose maximum location is used as the SLIM. SLIM method has been revealed to be highly sensitive to variations in surf similarity parameter, also in such a reflective beach environment, where the swash dissipation signature is strongly marked (Plant et al., 2009).

Information retained by the full colour images have allowed the investigation of new algorithms, moving beyond the lonely grayscale details. The different reflectance properties of the “wet” and “dry” regions are analysed in order to develop a new method to detect the shoreline (Colour Channel Difference, CCD), based on the identification of the divergence of red and blue pixels intensities over cross-shore transects (Turner et al., 2001, Turner, 2000). This approach could be seen as a bottom-up process.

By applying strategy of linking together several edges detector, Osorio et al. (2012) deployed the Physical and Statistical Detection Model, which uses six edge-detection techniques, based on a combination of statistical criteria with physical constraints (i.e. tidal cycle) on the spatially extension of the detection research area.

Using the RGB channels values, the shoreline-mapping problem could be represented as a contour objective function aimed to define a threshold level, within the region that bounds the shoreline. Such a contours detection is possible by partitioning an image into similar regions. An early approach (Kingston, 2003) made use of an opportunely trained Artificial Neural Networks (ANN) for the classification of land and water regions. Kingston (2003) defined the model output as a continuous variable with water and land samples having a value close to 0 and 1, respectively.

The actual Argus commercial systems, since the implementation of the so-called Intertidal Beach Mapper tool, uses the Pixel Intensity Clustering (PIC) model. The model is applied on Timex images, in a specific Region Of Interest (ROI), by means of a discriminator function Ψ to distinguish two clusters (Aarninkhof et al., 2003, Aarninkhof, 2003). The efficiency of the algorithm is guaranteed by the application of the routine on the two-dimensional colour (Hue-Saturation) and luminance (Value-Value) domains, using the best contrast. Uunk et al. (2010) attempted the complete automation of this extraction process, by varying the ROI position over time.

Vousdoukas et al. (2011) implement, over a ROI, a data-driven automatic procedure on SIGMA images, using information retained by images histograms that are fitted on an ensemble function of a 2nd order polynomial and two Gaussian shape functions. Over a vector composed by more than 1000 images in their trials, the optimal threshold value is based on the minimum Root Mean Square Error (RMSE) between automatic and manual extracted shoreline contours. A three-layer ANN perceptron, trained by the Levenberg-Marquardt algorithm, is introduced by using the fitting functions parameters and the four-histogram statistical moments as inputs (Vousdoukas et al. 2011). Compared to a priori threshold intensity value method, the ANN leads to a decrease in the average RMSE cross-shore locations and an increase of the overall data return rate.

A very similar approach, resulting in a highly performing automatic procedure, is described in Rigos et al. (2014). Differences between the two methods are related to functions used for histogram fitting and type of ANN. The Chebyshev polynomials are encompassed to approximate the histograms of grayscale variance images, after thresholding process segmentation developed in Vousdoukas et al. (2011). Radial Basis Function (RBF) network is employed, where the number of polynomial coefficients defines the dimension of input space. A fuzzy c-means clustering analysis has been used for radial basis function centres determination and the connection weights of the hidden nodes are calculated by using a steepest descent approach.

The above mentioned techniques, particularly PIC, ANN, CCD represents the most popular and overused methods. On the contrary, the segmentation and classification of the fundamental areas framed by typical coastal video monitoring station field of view has been rarely studied, and, to date, they could represent an alternative solution in order to eliminate the constraint due to the research of a ROI area. In a nearly contemporary work, Hoonhout et al. (2015) uses a semantic approach for the automatic pixels classification. Pre-defined set of classes, based on thousands of intrinsic and extrinsic pixel features, are defined and a supervised learning (SSVM) for class distinction is trained. While, an object-oriented analysis on low-tide images of Argus system has

been tested in Quartel et al. (2006) for morphology segmentation, using maximum likelihood classification, based on manually labelled regions for defining a model of class prediction.

2.2.3. ALIMINI Video Monitoring Experience and Database

In 2005, a video-monitoring station was installed at Alimini (Lecce), in South Italy. The acquisition system consisted in two webcams positioned on the top of a pole about ten meters high on MWL (Lisi et al., 2011).

The routine developed for Alimini coastal video-system, aimed at shoreline detection, is a color-based, Matlab implemented procedure. It aims at a user-assisted shoreline extraction applied on the ortho-rectified Timex images. In addition, run-up information and beach slope variation are studied in the experience.

The routine started with a ROI definition by the user, useful since the characteristic large swash excursion along very low sloped nearshore (around 1-2 %) and the presence of intertidal bars, leading to a large buffer area to process (around 200^2 pixels on the rectified image).

The tool works on RGB colour information from the jpeg coded images, and it partially includes the code developed by (Lau, 1997). User has to identify some points (regularly more than two to increase performance) in order to distinguish and segment sand and sea areas. The code works by selecting connected groups of pixels whose colour are consistent with respect to some reference pixels (user-selected), with a predefined tolerance. In order to get better results, tolerance level could be changed for colour similarity assimilation, other points could be selected in order to include areas ignored in the previous step and real time visual inspecting of the detected waterline allowed. A suitable procedure was developed enabling the user to solve characteristic summer issues due to obstacles (beach umbrellas, vehicles, etc.) on the image frame. It is mainly based on the interpolation of neighbouring pixels around the foreign objects, permitting their deletion.

During installation phase of the station at Alimini shore, a topographic survey was carried out. It allowed the definition of the spatial coordinates of a farm of GCPs (1739) distributed over two grids, materialized by applying white markers on some pegs located in the cameras Fiel of View (FoV) (Damiani and Molfetta, 2008) (Figure 2.2).

The advantages of this system are strictly connected to the remotely controllable acquisition and configuration, the presence of hydro-cleaning system, which guarantees useful recording also during wet weather, a useful website retaining only info on last images produced. Drawbacks are mainly due to (i) location on the top of the high dune, which has been prone to displacements during the station lifetime, (ii) the dutiful frequent maintenance in order to fill the water tank.

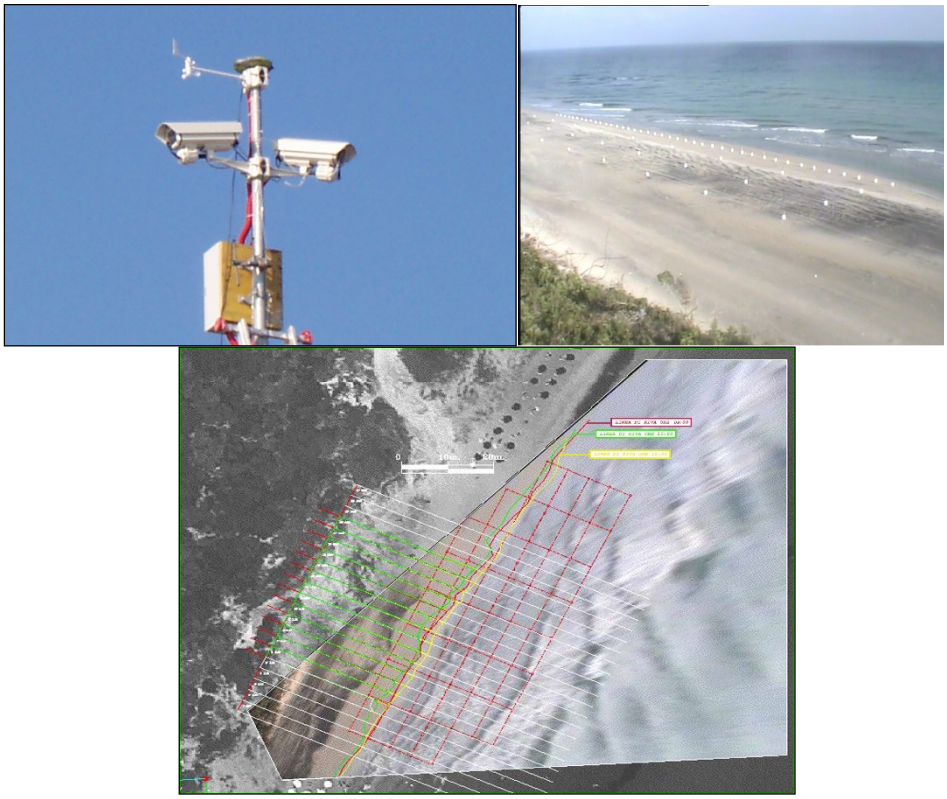

Figure 2.2 Alimini video monitoring station. **Top left:** Web-Cams installed with anemometer; **Top rigth:** GCPs grid on cam1 FoV; **Bottom:** Shoreline extracted with virtual grid and cross-shore transects for long-term analysis. (after Damiani and Molfetta (2008)).

2.3. Overview of new Shoreline Detection Model

The new Shoreline Detection Model (SDM), described hereafter, is the results of the boundary extraction from automatic segmented coastal area, it is calibrated and tested on Alimini dataset.

A pre-processing routine has been developed in order to bypass the issues due to low/different illumination or contrast and filter out outliers (algae, objects, etc.). A distribution of the popular software ImageJ: Fiji (Schindelin et al., 2012), is used for this task. The Fiji is one of the most used software in biological field for generating advanced image-processing pipelines, allowing to process large quantities of images via scripting languages and feature-rich libraries, based on the simplicity of Java.

Therefore, the main shoreline detection algorithm is implemented, inspired by the Global Probability of Boundary edge detector (Arbelaez et al., 2011), combined with segmentation steps based on detected boundaries procedure and, then, on the colour properties recognition for intertidal bars detection and a parallel overall correction. In the present work the ROI area limits, widely adopted, are eliminated, in order to face regional morphological/urbanization properties due to the combination of both swash length seasonal differences and constraints on low height of cameras.

While small seeds pixel areas are introduced in order to cope mainly with the constrained segmentation on the Ultrametric Contour Map, using Voronoi metric space, which will be described below (Subs. 2.4.5.).

In Figure 2.3, a flow diagram of the processes is pointed out.

It has been figured out that illumination and atmospheric dust/rain have a great influence into the Colour properties of coastal images. This issue is previously introduced in the work of Aarninkhof (2003), where the luminance-luminance and hue-saturation domains (HSV color space) are investigated in order to retrieve the relative spread of pixel intensities within two clusters of wet and dry regions for best contrast definition. In the present approach, it is considered uniquely the CIELab, a perceptually uniform colour space (Schwiegerling, 2004).

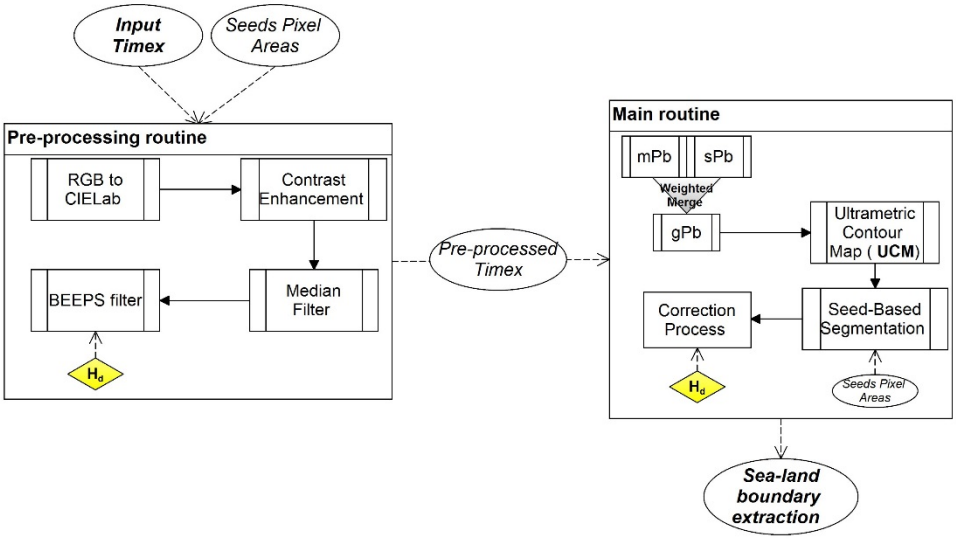

Figure 2.3 Block diagram of algorithms implemented for image pre-processing and main routine.

The histograms of the masked image by two small seed areas (around 200 pixels) representative of the sea water and sand pixel surfaces are calculated (Figure 2.10, Top left). This framed seed areas are supposed to remain constant during long-term monitoring. The normalized Chi-Square histogram (Pele and Werman, 2010) distance, H_d on the seed pixels areas, is assumed to determine the best contrasting colour feature, between *L* and *b*, useful for the further processing.

To sum up, the pre-processing steps could be described as:

i) RGB to CIELab colour space transformation;
ii) Contrast enhancement;
iii) Median filtering;
iv) Bi-exponential edge-preserving smoother (BEEPS).

In particular, the (iv) step is basically a version of the bi-exponential filter with adaptive weights, BEEPS (Thévenaz et al., 2012), itself realized by a pair of one-tap recursions (photometric STD=3.2 and spatial decay=0.004), applied on the best contrasting colour channel, L or b of CIELab color space, which derives from the normalized Chi-Square histogram distance (H_d) distance, calculated.

An example of the pre-processing task result is shown in Figure 2.4.

Figure 2.4 **Left:** Example of original Timex image and **Right:** pre-processed image (b)

It should be notice that *a* channel is neglected since from a preliminary qualitative analysis on the influence of each channels on cross-shore transects, it has been verified his low influence in the swash area.

In Figure 2.5 two reference images are shown, with CIELab components and respective profile plots, in the middle and right, respectively. The top left image is referred to a characteristic bright/sunny date time, while on the bottom left it refers to a shady/sunset date time. On the right part of the figure, it is highlighted the major influence of the *b* channel in the upper case image, with an almost straight "jump" in the 1-D profile, on the contrary the luminance domain "*L*" dominates the signal in the case at the bottom.

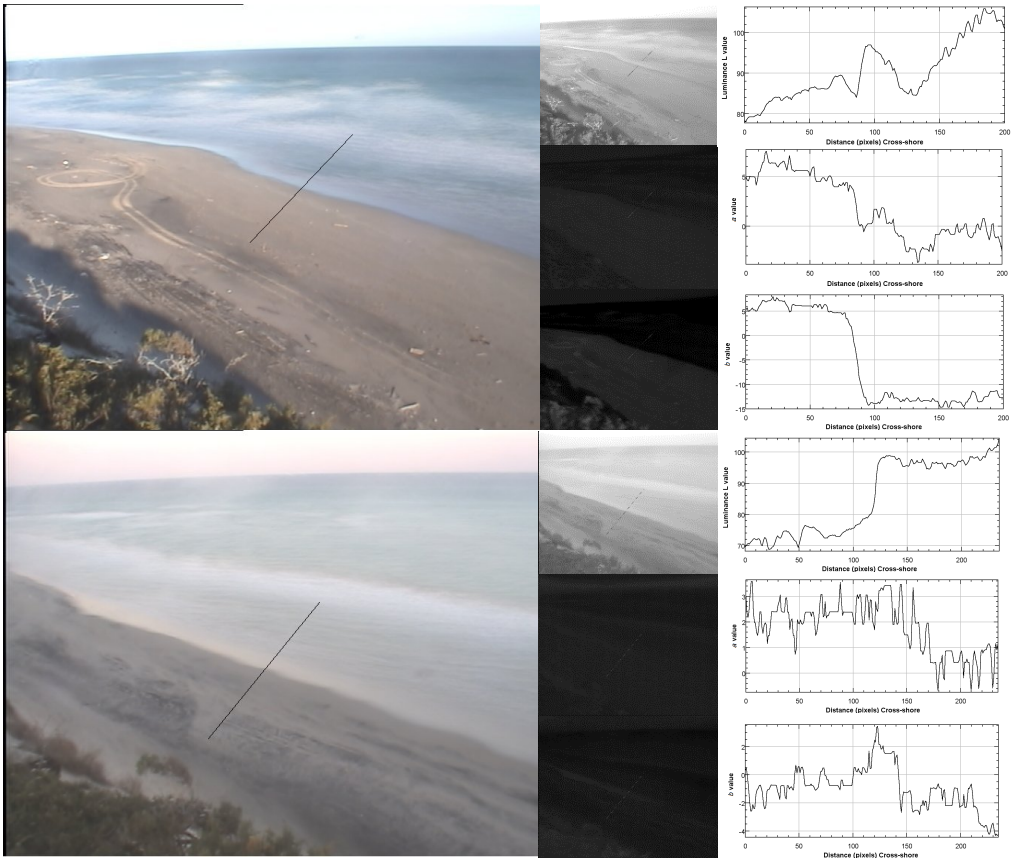

Figure 2.5 **Left:** Original images during sunny illumination condition and during sunset. Overlapped one cross-shore transect. **Middle:** *L*, *a*, *b* (CIE Lab) components of original images. Overlapped e.g. one cross-shore transect. **Right:** Corresponding 1-D sections for each colour feature components plotted.

2.4. Main routine

On the pre-processed images, the main routine for automatic segmentation and then, shoreline detection algorithm, is implemented.

Contours and shape-based features have been always used with success and, as highlighted in Subs. 2.2.2. implemented in some detection algorithms in coastal video analysis, although there is a sense that low-level machinery, which produces contours

alone, is not enough. Often, a partition of the image into meaningful segments is aspired. Actually, segments may reduce the computational complexity of subsequent stages by transforming an image consisting of millions of pixels into hundreds of regions. A subdivision of the main routine can be summarize as follows: i) *Contours detector* algorithm over the full frame; ii) *2-steps segmentation*; iii) intertidal bar solver and *correction process*.

2.4.4. Global Probability of Boundaries

The contours detector implemented and described hereafter is based on the application of a modified version of the global Probability of boundary (*gPb*) concept (Arbelaez et al., 2011).

The *gPb* contour detector is thought in order to combine the benefits of bottom-up techniques, such as simple edge detection, with those of top-down approaches like clustering, including both approaches into a probabilistic framework. Indeed, it works by combining a multiscale (mPb) and spectral (sPb) probability of boundary detectors, and the final result as well as all intermediate results are regarded as probabilities.

A key prerequisite of the model is its capability in predicting the posterior probability, $Pb(x, y, \theta)$ that a pixel (x, y) is part of a boundary with orientation θ, by measuring differences in local image brightness (BG), colours (CGA/CGB) and texture (TG).

The probability of boundary, Pb (Martin et al., 2004) is built upon the computation of an oriented gradient signal $G(x, y, \theta)$ on the image intensity (I). This process is accomplished through the definition of the distance $\chi^2(g, h)$ between two histograms computed at location (x, y), Eq. (2.1), by placing a circular disc (computationally approximated as a series of rectangular boxes) split into two half-discs (g, h), along the diameter, at angle θ (Figure 2.6):

$$\chi^2(g, h) = \frac{1}{2}\sum_i \frac{\left(g(i) - h(i)\right)^2}{g(i) + h(i)} \tag{2.1}$$

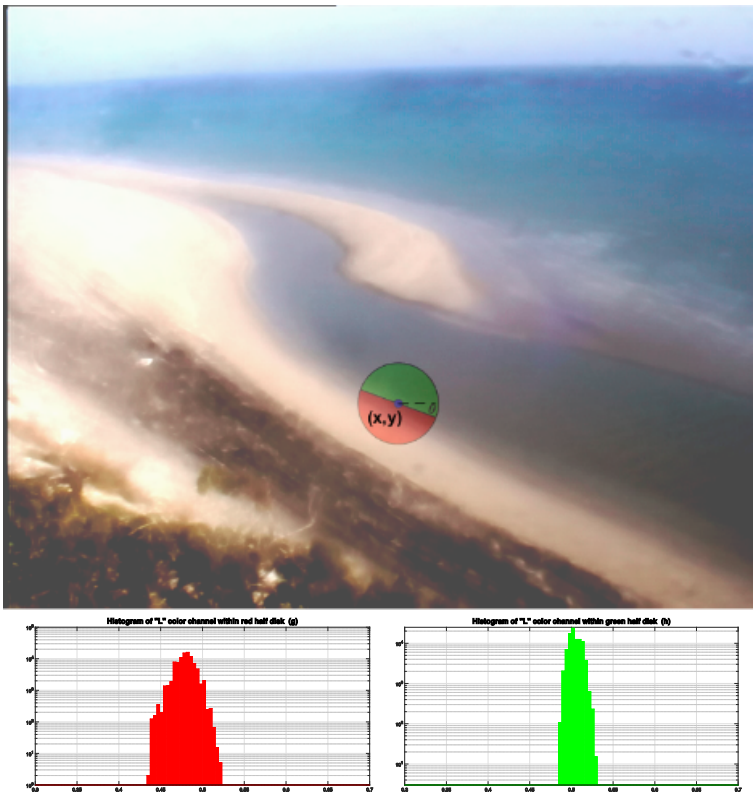

Figure 2.6 **Top:** Given an image, consider a circular disc, centered at a pixel and split along the diameter. Magnified view of the overlapped circular disc. **Bottom:** Example of half-discs histograms, *h* and *g,* at location (x, y) and orientation θ.

A second-order Savitzky-Golay filtering stage is applied to enhance local maxima and smooth out multiple detection peaks in the θ orthogonal direction (Maire, 2009).

The detector is based on the combination of the oriented gradient signal $G(x, y, \theta)$, separately computed on 4 image channels: the 3 CIELab colorspace channels and a texture one. The latter is built by assigning a texture id (texton) to the pixel value, after a prior filtering stage. It consists in the convolution of the grayscale channel image with texton filter sets, constituted by 17 Gaussian derivative and centre-surround filters (Maire, 2009), then followed by a K-means clustering stage (MacQueen, 1967) applied

on the relative vectors of response. By this way, each pixel value is associated to the integer texture id in the range $[1, K]$ of the closest cluster center. In this implementation, K is set equal to 16. The typical white band associated to the swash and/or the wave roller area (the white, aerated, turbulent mass of water at the breaking wave face) could be clustered as a homogeneous region.

As highlighted also in Ren (2008), multi-scale processing improves boundary detection, boosting precision at salient boundaries, preserving, at the same time, details. In order to completely automatize the routine and for a precise shoreline contours extraction, such a concept complies with peculiar shoreline conformations (e.g. sharp bends or large swash area), due to different morphological factors, to the height of the camera and to the monitored area extension.

The multiscale extension of the Pb is performed by considering 3 gradient scales $[\sigma, 2\sigma, 3\sigma]$ for brightness, color and texture channels. Both brightness and colour σ are set at 4 pixels, while for texture channels σ it is considered equal to 5 pixels. The combination of local cues is made by calculating the linear operator defined in Eq. (2.2):

$$mPb(x, y, \theta) = \sum_{s} \sum_{i} \alpha_{i,s} G_{i,\sigma(i,s)}(x, y, \theta) \tag{2.2}$$

where s and i represent the index scales and feature channels, respectively. $G_{i,\sigma(i,s)}(x, y, \theta)$ are the histogram distances and $\alpha_{i,s}$ the learned weights associated to the features channels and gradient scales. In the routine, θ is sampled at 8 equally spaced orientations, as in Arbelaez et al. (2011), assuming it as a realistic balance between routine efficacy and computation efficiency. The boundary strength is well defined by taking the maximum over the sampled orientations (Eq. (2.3)):

$$mPb(x, y) = \max_{\theta} \{mPb\ (x, y, \theta) \tag{2.3}$$

The boundary locations as derived from the previous step are still very blurry and it is not immediately clear where the exact region boundary would be. Hence a non-maxi-

mum suppression, whose working principles are the same as the non-maximum suppression used by the Canny edge detector (Canny, 1986) would produce thinned, real valued contours.

The mPb detector can only provide local features.

Globalization - Spectral Partitioning

A completely different way to detect contours is to partition an image into similar regions. One way to classify the region-based approach to partitioning techniques is among clustering and energy minimization in graphs.

Spectral clustering attempts to unite both concepts. Like other clustering algorithms, spectral clustering is trying to partition data points into groups such that the members of one group are similar to each other and dissimilar to data points outside of that group. Spectral clustering makes use of the spectrum (the eigenvalues) of a graph that is expressed in the form of an affinity matrix to perform dimensionality reduction before clustering in fewer dimensions. With respect to different clustering approaches, spectral techniques are usually less prone to be stuck in local optima. It has a simple formulation and can be solved by standard linear algebra techniques. Moreover, it typically produces better results than traditional clustering algorithms such as k-means and mixture models. There are many algorithms and variants for the spectral clustering (MeilPa and Shi, 2001, Ng et al., 2002, Shi and Malik, 2000). A well-defined overview of overused methods and implementation is described in (Verma and Meila, 2003).

The work of Maire (2009) describe a soft manner for treating eigenvectors using spectral partitioning and it is here implemented. A sparse affinity matrix W, is defined as a function of $max\{mPb\}$ along all lines connecting couple of pixels (Eq. (2.4)):

$$W_{ij} = \exp(-\max_{p\in\overline{ij}}\{mPb(p)\}/\omega) \tag{2.4}$$

where $\overline{ij}$ is the line segment, connecting the i_{th} and j_{th} pixels, sampled with Bresenham's algorithm (Bresenham, 1965) and ω is a constant. The latter controls the

strength of the affinity and how similar two pixels have to be in order to be assigned to the same region, and it is set equal to 0.1 (Arbelaez et al., 2011).

The graph partitioning approach would led to a fully connected graph, which would determine that every pixel has to be connected to all each other, hence in order to balance quality and memory consumption, the value of radius of the neighbouring pixels connected is set to $r = 5\ px$.

The system $(\mathrm{D} - W)\boldsymbol{v} = \boldsymbol{\lambda} D\boldsymbol{v}$, where $D_{ii} = \sum_j W_{ij}$ is the row-sums of the affinity matrix D, is solved for the generalized eigenvectors $\{v_0, v_1, \dots, v_n\}$ which corresponds to n+1 smallest corresponding eigenvalues $0 = \lambda_0 \leq \lambda_1 \leq \dots \leq \lambda_n,\ n = 16$.

As highlighted in (Eggert (2012), Maire (2009)), standard approaches, after this step, proceed with K-means clustering in order to just obtain a segmentation into regions. However, this strategy very often breaks uniform regions where the eigenvectors have smooth gradients. Looking at solutions for this issue, for example Tolliver and Miller (2006) worked in reweighing the affinity matrix, or Yu (2005) applied different partitioning formula.

At this point, treating the eigenvectors $\boldsymbol{v_k}$ as images, as in Arbelaez et al. (2011) and Maire (2009), the convolution of the latters with Gaussian derivative filters is applied at multiple orientations θ. Such a spectral partitioning technique is able to extract the most salient curves on images, and to obtain the oriented spectral component of the global detector, $sPb_{v_k}(x, y, \theta)$, the Eq. (2.5) is applied:

$$sPb(x, y, \theta) = \sum_{k=1}^{n} \frac{1}{\sqrt{\lambda_k}} sPb_{v_k}(x, y, \theta) \tag{2.5}$$

The global probability of boundary is hence formalized as a weighted sum of multiscale local and spectral detectors, assuming this formulation:

$$gPb(x, y, \theta) = \sum_{s} \sum_{i} \beta_{i,s} G_{i,\sigma(i,s)}(x, y, \theta) + \gamma\ sPb(x, y, \theta) \tag{2.6}$$

where $G_{i,\sigma(i,s)}$ are the oriented gradients as delivered by the mPb detector. γ and $\beta_{i,s}$ are the weights for i^{th} and s^{th} cue and scale, respectively.

In the Figure 2.8 an example of $mPb(x,y)$, $sPb(x,y)$ and $gPb(x,y)$ processed images are shown.

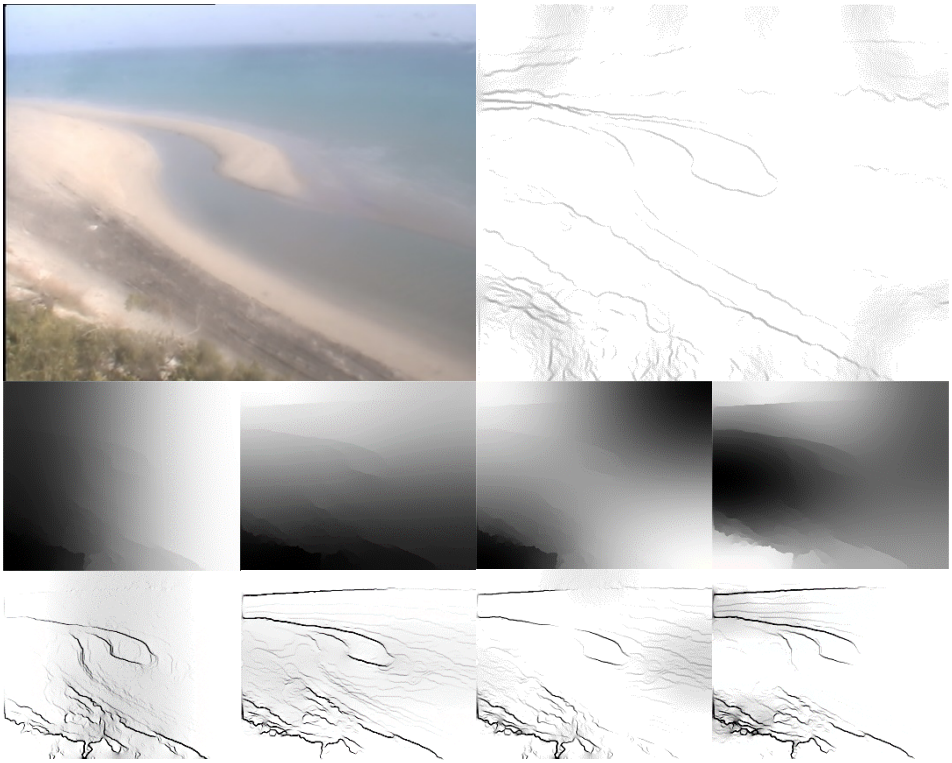

Figure 2.7 **Top:** Original image and maximum response of *sPb* over orientations θ. **Middle:** First four eigenvectors in the spectral *sPb*. **Bottom:** maximum response of *sPb* over orientations θ for each components in the middle panel.

As with the *mPb*, the gradients over all orientations could be combined into a single image by taking the maximum over all orientations.

$$gPb(x,y) = \max_{\theta}\{gPb(x,y,\theta)\} \tag{2.7}$$

A thinned non-max suppression and skeletonizing steps (Kong and Rosenfeld, 1996) on the thinned image could be applied in order to pass through the blurry border maps, as displayed in bottom right of Figure 2.8, to thinned ones.

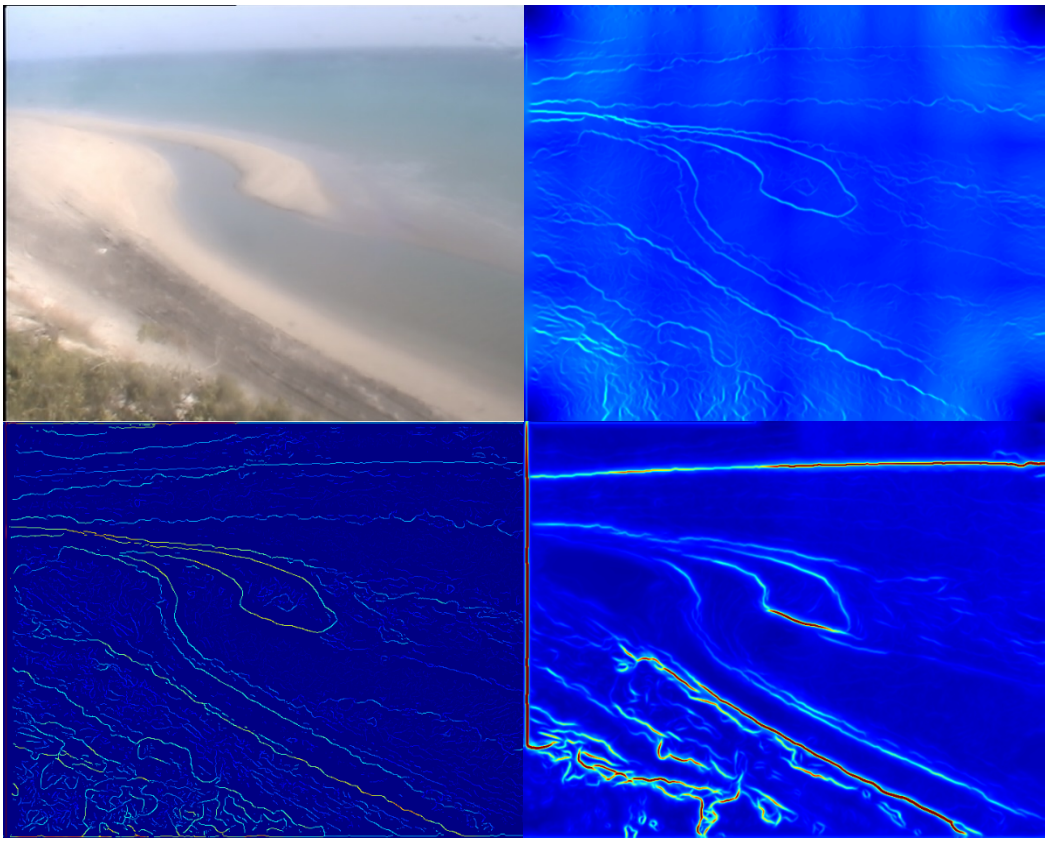

Figure 2.8 **Top left**: Original Image; **Top right**: Multiscale Probability of boundary component as jet colormap; **Bottom left**: Spectral Probability of Boundary as jet colormap; **Bottom right**: Global Probability of boundary as jet colormap

2.4.5. Segmentation and shoreline extraction

The 2-steps segmentation tasks, introduced above, follow the boundaries detection process. The algorithms employed, reported in (Arbelaez (2006), Arbeláez and Cohen (2008), Maire (2009)), are implemented in order to produce a hierarchical boundaries

map that becomes useful for enforcing regions closure and which is used for a subsequent seed-based segmentation, allowing few framed overall distinct areas of the shore to be classified.

From the previous contour detectors step, an *Oriented Watershed Transform* (OWT) (Arbelaez et al., 2009) is employed, based on a morphological watershed transform (Beucher and Meyer, 1992, Najman and Schmitt, 1996), applied on the topographic surface defined by the signal $E(x,y) = \max_{\theta} gPb(x,y,\theta)$, better described in SubS. 2.4.4.

In the study of image processing, a watershed of a grayscale image input is analogous to the notion of a catchment basin. From a geographic/hydraulic point of view, watersheds represents the divide lines which separate neighbouring drainage basins of a topographic relief, landscape flooded by water. In mathematical morphology, it can be classified as a region-based segmentation approach (Roerdink and Meijster, 2000).

The OWT starts with flooding the above-mentioned $E(x,y)$ signal from seed local minima, hence, a partition of the image into regions is performed: let us denote P_0 and K_0 the regions and watershed arcs of the partition, respectively.

A specific procedure is applied to reweight the watershed arcs K_o, which are approximated as straight-line segments and suitably subdivided in a scale-invariant manner. The original arcs in K_o are assigned weights according to the pixels $gPb(x,y,\theta)$ signal they contain. Such a procedure is able to suppress artefacts due to the spatially extended response around strong boundaries produced by contours detector gPb (Maire, 2009).

In order to add a probabilistic factor on the image segmentation calculation, the opportunity to use the *Ultrametric Contour Map* (UCM) is undertaken. It represents a useful algorithm for exploiting the potential of weighting closed boundaries at different threshold value, the latter determined by the average contour strength. A hierarchy of regions is built by using a graph-based region merging strategy.

The process starts with the construction of a graph, defined by the Eq. (2.8):

$$G = (P_0, K_0, W(K_0)) \tag{2.8}$$

where K_o represents the watershed arcs separating regions, P_0 is the regions set and $W(K_0)$ indicates the weights initialized by the OWT, holding the measure of similarity between regions. The algorithm is intended to sort the arcs by similarity, hence iteratively merging the most similar regions. The result is the definition of a tree of regions, ordered by an inclusion relationship, defined as *indexed hierarchy*.

Ultrametric property are satisfied by the dissimilarity distance (Arbelaez et al., 2011). At the end, the first step permits the composition of a real-value image (double-sized), with the property of producing closed curves for any threshold value (Figure 2.9).

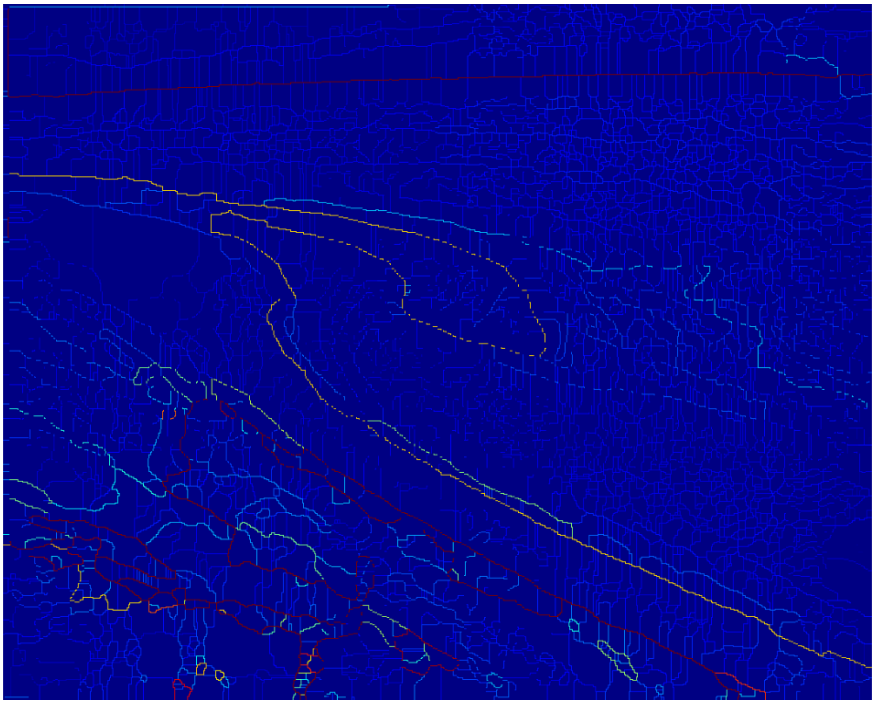

Figure 2.9 Jet colormap of the *UCM* obtained by using as input *gPb* detector boundaries on an example Timex image.

The second-step is based on the implementation of the algorithm firstly described in Arbeláez and Cohen (2008), who studied the connection between seed-based and hierarchical segmentation and proposed a front propagation strategy on the UCM map, by using *Voronoi tesselations*.

A *tessellation* may be defined as a division of a space into polygonal regions of convex shape. A classic example of a randomly generated tessellation is the Voronoi tessellation which separates a region into cells $\{Di\}$ using a set of points/sites X_0. A description of the Voronoi tessellation can be summarized as follows: for any point x_0 of the set X_0, let D_i be the area consisting of all locations in the space which are closer to x_0 than to any other point of the set X_0. This definition is applicable to Voronoi tessellations in whatever metric space.

To be able to implements the Voronoi tessellations on an ultrametric space, an approach of measuring distances to an ensemble of sets of image domain is presented in Arbeláez and Cohen (2008) and it is based on the front propagation strategy, similar to the Dijkstra's algorithm (Dijkstra, 1959), or to the Fast Marching Method (Sethian, 2003). It aims at computing the minimal distance function $U(x) = d(x_0, x)$ of nodes x to some starting seed points x_0.

In this case, a weighted graph, defined as $G = (X, L, C_w)$ is used for discretization, where $X = P_0$ is the set of nodes, L the set of links between two adjacent regions, and C_w represent the set of scales of disappearance of the contour from the hierarchy of contours in the UCM, respectively. The general initialization of this algorithm can be found in Peyré and Cohen (2006) and be defined, following different naming convention, as follows:

Initialization:

- *Alive* set: the starting x_0;
- *Trial* set: the neighbours of x_0;
- *Far*: the set of all other grid points.

Loop:

- Let x be the *Trial* point with the smallest priority $Pr(x)$;
- Move it from the *Trial* to the *Alive* set;
- For each neighbour y of the current point x:

  - If y is *Far*, then add it to *Alive* and compute a new value for $U(y)$,
  - If y is *Alive*, re-compute the value $U(y)$, and update it if the new value is smaller,
  - Re-compute the priority $Pr(y)$.
- If the end point $x = x_0$ is reached, stop the algorithm.

The propagation methods is capable of labeling the points during the computation according to:

- *Alive* is the set of points at which the distance value U has been computed and will not change;
- *Trial* is the set of next grid points to be examined and for which the computation of U has been performed;
- *Far* is the set of all other grid points, not yet investigated and for which estimate of U does not exist (Peyré and Cohen, 2006).

The inputs are the UCM and a set of seed pixels (X_0), that in this implementation, are labelled as *Sea wate*r, *Sand* and *Sky*. The outputs are constituted by the ultrametric distance of a general pixel from X_0 and the relative labels (Figure 2.10). The priority map $Pr(x)$ and the function $U(x)$ are both equal to the ultrametric distance from x to X_0, whose value is calculated as the maximum weight on the shortest path between x and X_0 (Arbeláez and Cohen, 2008). The update of the function $U(x)$ using adjacent nodes is computed by using Voronoi tessellation.

The last process stage of the main routine has been thought in order to search for intertidal bars boundaries and correct the results of the previous constrained segmentation, using the colour properties of the UCM regions. Firstly, a fraction of the mean value of UCM map is chosen ($15\ \%$) as optimal threshold for breaking down the region tree of UCM and obtaining a set of closed boundaries on image-basis, in order to select the properties to be investigated. The Sea water/Sand interface is investigated by implementing a routine for the comparison between the colour properties (*L* or *b* features only) of UCM segments, whose centroids are close (a fraction of image size) to those of the opposite labelled area. By this way, segments which held much similarity (based on H_d) with respect to the opposite seed label pixels, are marked as different seeds for a new constrained segmentation (Figure 2.10).

All the processes are here suitable targeted at the shoreline detection, hence the sea-land boundary extraction is performed with a sub-pixel accuracy (Trujillo-Pino et al., 2013).

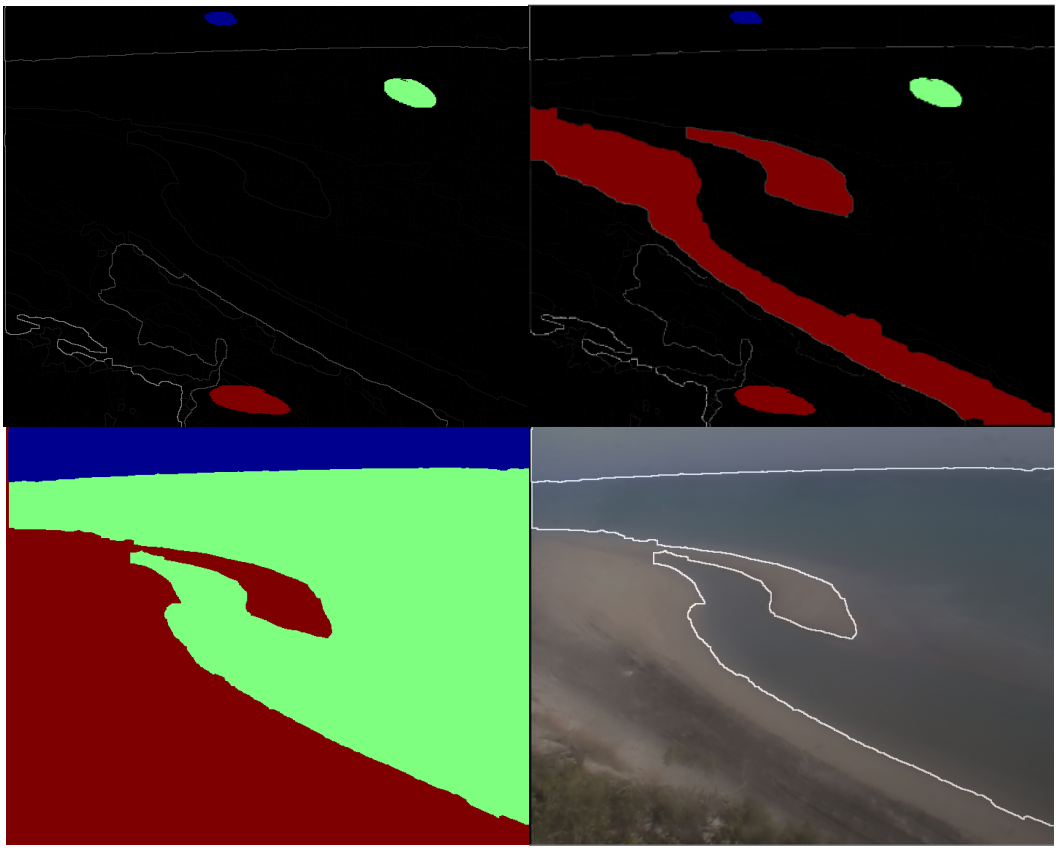

Figure 2.10 **Top Left:** UCM map image as input for seed-based/constrained segmentation approach, three labels highlighted in different colours. **Top right:** UCM map image and new-seeds highlighted after the last correction approach for new segmentation is applied. **Bottom left:** Segmented Image with three labels highlighted. **Bottom right:** Original Image and overlapped boundaries layer.

2.5. Calibration and results

2.5.1. Methodology

Precision-recall curve represents a common evaluation technique in the information retrieval standard and it could also be used for evaluating edge detectors. It is a parametric curve that measures a balance achieved between accuracy and noise as the detector threshold varies.

The theoretical global F-measure (F), shown in Figure 2.11, can be defined as the harmonic mean of Precision (P) and Recall (R), Eq. (2.9), where P is the fraction of detections that are true positives rather than false positives, while recall is the fraction of true positives that are detected rather than missed (Martin et al., 2004). Actually, while P is representative of the noise in the detector outputs, R quantifies the ground-truth detected and w, Eq. (2.9) is the relative importance associated to P and R.

$$F = \frac{PR}{wR + (1 - w)P}, \quad w = 0.5 \tag{2.9}$$

In particular, the location of the maximum *F*-measure along the curve provides the optimal detector threshold for the application. In this case, an image-basis threshold is used.

A way of measuring the correspondence between the detectors' outputs and Ground-truths could simply be the evidence of coincidence of boundary pixels and the assignment of false positives to unmatched ones. However, this approach, mostly known in computer vision community, would penalize, to an excessive extent, marginal localization errors. The approach of (Martin et al., 2004) and their implementation is used here in order to measure the *F* and perform the weights calibration.

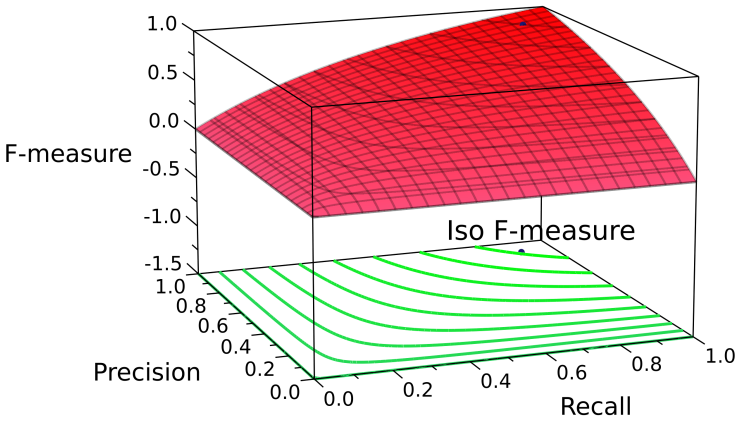

Figure 2.11 Theoretical global iso-F curves. Black point refers to the $F = 0.9$, assumed representative of Ground-truth.

Their algorithm is built by dealing with the correspondence problem as a minimum cost assignment problem; specifically they formulate a sparse assignment and construct this in order to comply with peculiar algorithmic constraints. The weight associated to the automatic contour and Ground-truth is assumed proportional to their relative distance, on image-basis. The reader is referred to the above mentioned work of Martin et al. (2004) for detailed discussion of this issue.

For the computer vision advance, in the effort to create methods and define samples for segmentation algorithms comparison, (Martin et al., 2001) developed an image segmentation benchmark by which one can objectively evaluate segmentation algorithms: Berkley Segmentation Database (BSDS). It consists of 300 natural images, each

of which has been manually segmented by a number of different human subjects and provides a useful metric needed for evaluating contour detectors performance through comparison to human-drawn ground-truth boundaries, for generic natural images.

With the aim of learning weights for local features combination (*mPb*, Subs. 2.4.4.), a logistic regression classifier is used in Martin et al. (2004), while Arbelaez et al. (2011) approach a gradient ascend method, both based on the BSDS.

In this contest, Timex images from Alimini database are used for calibrating the weights in the *mPb* signal ($\alpha_{i,s}$) and *gPb* signal ($\beta_{i,s}$). The training dataset consists of 30 images, chosen among several different illumination conditions, seasons and morphological shapes (i.e. emerged intertidal bar, strict curves, etc.). The manually detected shorelines (Ground-Truth) are assumed to be represented by $P = 0.9$ and $R = 0.9$.

The starting vectors are defined by the weights vectors implemented in Arbelaez et al. (2011). Then, the $\alpha_{i,s}$ and $\beta_{i,s}$ are learned by minimizing an unconstrained multivariable function, using a derivative-free method fminsearch (Lagarias et al., 1998), applied on the above described F-measure, which provides a useful score for comparing automatic real-value contours masked on the shoreline area and the manually detected shorelines (Ground-Truth).

The F-score curves of learned weights for *L* feature channel of *gPb*, *mPb* are shown in Figure 2.12, overlapped to the iso-F lines. Moreover, the UCM curve is plotted.

The model SDM has been then validated by using Timex images from Alimini database and manually mapped shorelines. This testing dataset is composed by 30 images processed by both cameras installed, using two different interval periods, during April 2006 and October 2007, each 8 days long. The cross-shore distances from a baseline on 60 transects have been used (Valentini et al., 2016).

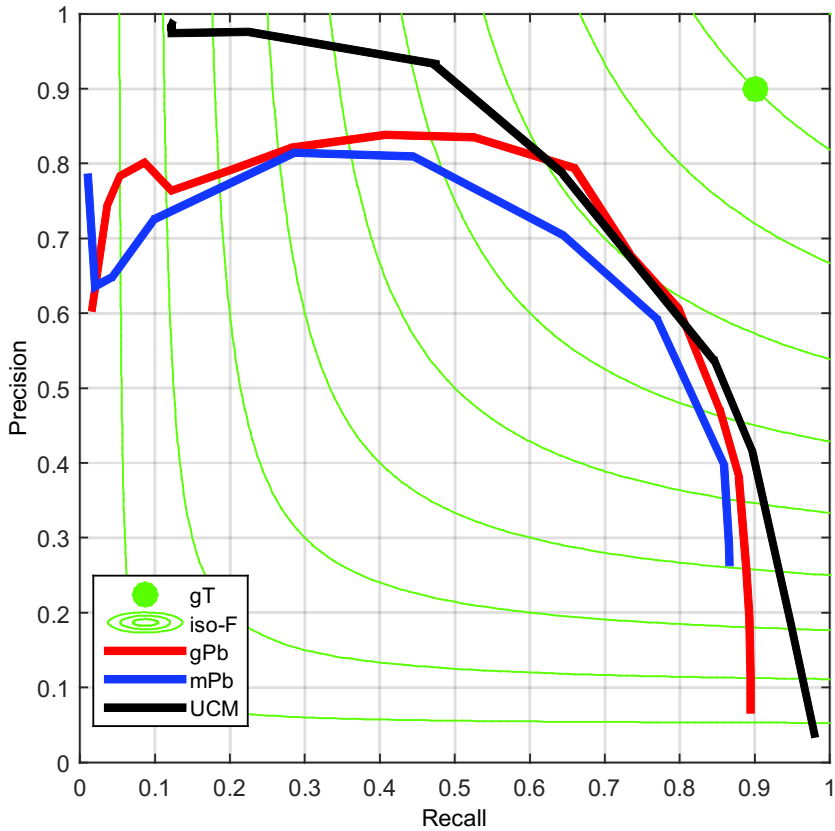

Figure 2.12 F-score curves of learned weights for L-channel of *gPb* (red), *mPb* (blue). UCM (black) curve is also plotted.

The Figure 2.13, at the top, reports an example of the comparison between manual (blu line) and automatic (red line) shorelines. In the same Figure 2.13, at the bottom, the distribution of data based on the five number summary (minimum, first quartile, median, third quartile and maximum) is displayed in the box plots for each analysed image.

The results show particularly good reliability, with respect to similar experiences, where pixels space is used for the comparison (Osorio et al., 2012, Santos et al., 2012). With reference to the relative distances (Δ) between the automatic and manual shorelines, the Table 2.1 reports the mean overall statistics.

Table 2.1 Main statistics (image pixel space) of the SDM model at Alimini.

$mean_{\Delta}$	max_{Δ}	min_{Δ}	$median_{\Delta}$	std_{Δ}
1.88	5.97	- 2.08	1.9	1.74

It can be noticed that all datasets are approximately balanced around 2. Indeed, the mean over 30 images is equal to 1.88. However, there is substantially more variation in some images datasets with a maximum range, (third to first quartile distance) approximately from -2.2 to 4 for image n. 3, whereas data relative to images 27 show the minimum range approximately from 1 to 1.5. In most images the sample dispersion, represented by the distance between the upper and lower quartiles, is very close to the median, which indicates that the 50 % of data is concentrated in the median value. Those images are characterized by quite straight shoreline in an optimal illumination condition.

Moreover, for all images the median values (horizontal red line in box plots) are positive. This means that automatic shoreline is, on average, placed offshore with respect to the manual one. As a matter of fact, the manual detection has been verified to partially include wet sand, that could probably explained this behaviour. 11 images show the presence of outlier values, in general 1 for image, except for image n. 12 for which 4 outliers can be identified. Most of the outliers are positive, and relative to the further transects from the camera. The analysis of the results also shows that few images (i.e. 1, 3, 21, 24) are characterized by a high standard deviation (mean value over the 60 transects greater than 3), most probably due to the *mPb* performance which calculates local cues at a minimum scale of $\sigma = 4$. Such a behavior underlines the ambiguity in recognizing sharp bends along the shoreline, especially for transects placed far from the cameras.

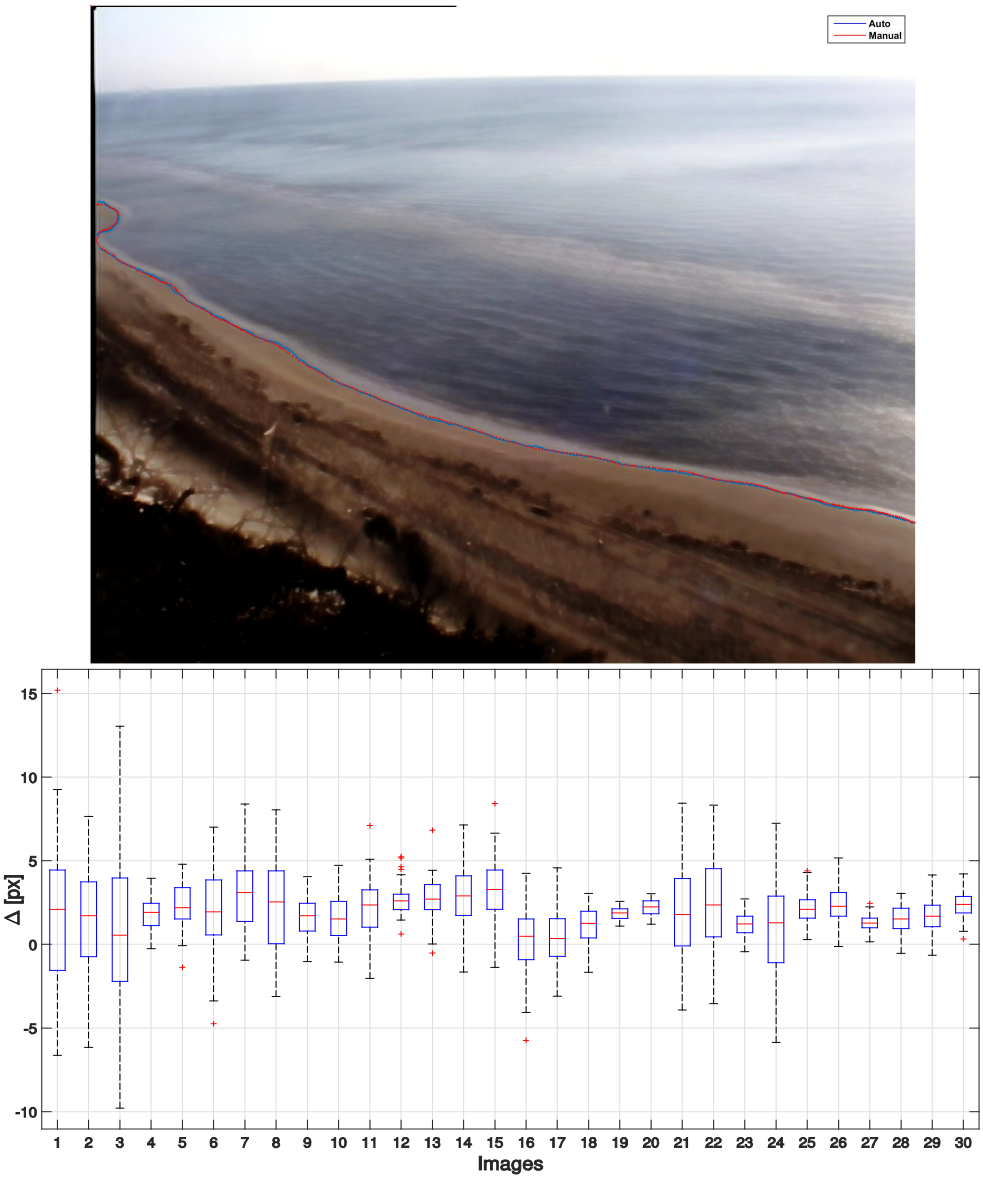

Figure 2.13 **Top:** Example of comparison between manually (red spots) and automatic shoreline contours (blue spots); **Bottom:** Statistic box plots of results for 30 images analysed.

2.6. Implementation

The algorithms implementation, in the present study, is based on libraries of the *gPb* detector, segmentation routines of OWT-UCM and seed-based by Maire (2009). The original implementation of *Pb* (Martin et al., 2004) is indeed extended to *mPb* detector and then, to *gPb*. This overall implementation includes modifications to allow it to be run on multiple scales, to adjust scales parameters and clusters number, to combine the results and implementing the non-maximum suppression step. Moreover, it includes the calibration of the basic combinatorial weights and the introduction of overall correction and intertidal bars solver.

The full implementation is developed in MATLAB environment, combined with several C++ and Fortran dynamic linked subroutines (MEX) above-mentioned that MATLAB interpreter loads and execute. *MATLAB Compiler*™ is chosen in order to implement a standalone application. It includes the component: *MATLAB Runtime* (v.8.1) which is essentially based a standalone set of shared libraries that enables the execution of compiled MATLAB applications or components on computers that do not have MATLAB installed. It is an easy and quick way thought in order to release and install the routines on whatever distributions (Linux-based).

2.7. Conclusions

The chapter presents a new automatic algorithm for shoreline extraction from Timex images recorded by a field video monitoring system. The Shoreline Detection Model (SDM) is based on the identification of sea/sand boundary from automatic segmented coastal image framed by visible camera. Code calibration and validation have been performed on the Timex images recorded at Alimini (Lecce, Italy) by a video station previously installed in 2005.

Calibration process has allowed deriving both the *mPb* and *gPb* signals weights based on F-measure. The comparison shows a good agreement for all the images considered, with a mean error of 1.88 pixels over 60 transects.

The higher standard deviation occurs for few images, probably due to the minimum scale chosen for σ, which conducts to some ambiguities in recognizing sharp bends along the shoreline, especially for those transects placed far from the cameras. This scale is chosen for achieving a balance between efficiency and computational time.

The further researches in this direction would be the analysis of the relative importance in down-warding the minimum scale parameter σ, in order to be completely insensitive to the height and the distance of the camera, as well as to all possible shoreline shapes. Moreover, it would be necessary the implementation of more feasible and not consuming routines in order to calibrate the weights $\alpha_{i,s}$ and $\beta_{i,s}$ without manual shoreline mapping, and, for example, by learning them on the base of images and pixels seeds area histograms.

CHAPTER 3

NEW APULIAN COASTAL VIDEO MONITORING SYSTEM

Chapter 3 - NEW APULIAN COASTAL VIDEO MONITORING SYSTEM

3.1. Introduction

In Italy, and especially in Apulia region beach video-monitoring systems are still at initial stage of development, mainly because of the relative high cost of commercial systems that has made the littoral video-monitoring difficult to be deployed and maintained for management organizations and also for the scientific community. For that reason the development of an efficient, almost completely automatic and low-cost video-monitoring system, which is the main goal of this chapter, is fully justified.

This has been achieved through the development of a video-monitoring system, built upon rigorously calibrated non-metric IP surveillance cameras, able to accurately quantify coastal processes.

3.2. System description

The new video monitoring system has been built through close cooperation between the Technical University of Bari, DICATECh Department, Multitel research centre, Image Processing R&D Department (http://www.multitel.be/) and its spin-off ACIC (http://www.acic-tech.be/). System development aimed at some core factors including easy installation, robustness, low cost, efficiency of the acquisition and tasks scheduling.

In order to meet these objectives, few firm principles are taken into account:

- Disjoin the post-processing processes from the acquisition ones, the former take place on remote server computing clouds, the latter take place on-site. This enable the independence on type of cameras and hardware solutions from post-processing steps;

- find a compromise between compact and cost-effective, network cameras solution;
- guarantee all the calibration procedures, including the lens distortion correction, to be applied on-site, without affecting overall accuracy;
- contribute to the distribution of video-analysis results by building an user-friendly, Java based, interface in order to gain a broad based support and public participation.

3.3. Image acquisition

The system has to be placed in location with a good overview of the shore to monitor, primarily at high place. Considering the difficulty to ensure stability and robustness of steel poles in such dynamic environment (Chapter 2 -), littoral establishments, structures are preferred, when available. They also represent a good solution in order to rely on power supply systems, which are of paramount importance.

The image acquisition procedure has been implemented by using state of the art autonomous IP cameras, detached from archiving/processing server or laptop, which guarantee a decentralized framework; hence, the acquisition phase could be preserved during components maintenance, by using substituted hardware.

The redundancy ensured by the storage on both local low-cost servers running Unix-based operating system and remote servers is a key factor in this system deployment. By doing this, one could choice best solution for local Hard-Drive copy, while the web-portal is served by server storage via rest call.

The use of low-cost router, dual-band 4G/3G sim cards enable a secure and, depending on the network coverage (signal strength), fast connection. This source, combined with a stable power supply serving server with remote controls features, determine an increment of efficiency, particularly for far-field system location.

3.4. Geometry of cameras

The transformation of image coordinates into world coordinates involves three main steps, which can be summarized in: (i) *intrinsic calibration*, where the internal camera parameters are determined in laboratory, or even in the field; (ii) the proper *image correction*, which aims to correct the relatively large image distortions induced by internal camera optics and (iii) *image rectification* to transform oblique images into vertically equivalent images (rectified images), generally coupled with georeferencing procedure.

Most of the commercial cameras undertake an amount of manufacturer distortions, which must be corrected. The Intrinsic calibration has been performed parallel to phase of installation, (Bouguet, 2004, Bradski and Kaehler, 2008, Wolf and Dewitt, 2000, Zhang, 2000) accounting for the following parameters: focal length, principal points, distortions with radial at 6th order and tangential components, neglecting skew. For visible cameras, square or circle pattern chessboards are typically used for this task. The model, which is used to describe the internal matrix and distortion model in matricial form, is as follows:

$$\begin{bmatrix} u \\ v \\ w \end{bmatrix} = \begin{bmatrix} f_x & 0 & c_x \\ 0 & f_y & c_y \\ 0 & 0 & 1 \end{bmatrix} \begin{bmatrix} x'' \\ y'' \\ z'' \end{bmatrix} = \mathrm{K} \begin{bmatrix} x'' \\ y'' \\ z'' \end{bmatrix} \tag{3.1}$$

where u and v represent the coordinates of a point in the distorted coordinate system, f_x and f_y the camera focal lengths and (c_x, c_y) is the optical centre expressed in pixels coordinates. w is explained by the use of homography coordinate system (and $w = z''$). The matrix K containing these four parameters is referred to as the C*amera Matrix*. The vector (x'', y'', z'') corresponds to the normalized point with radial and tangential distortion numerically defined as:

$$\begin{aligned} \mathrm{x}'' &= \mathrm{x}'(1 + \mathrm{k}_1\mathrm{r}^2 + \mathrm{k}_2\mathrm{r}^4 + \mathrm{k}_3\mathrm{r}^6) + 2\,\mathrm{p}_1\,\mathrm{x}'\mathrm{y}' + \mathrm{p}_2(\mathrm{r}^2 + 2\,\mathrm{x}'^2) \\ \mathrm{y}'' &= \mathrm{y}'(1 + \mathrm{k}_1\mathrm{r}^2 + \mathrm{k}_2\mathrm{r}^4 + \mathrm{k}_3\mathrm{r}^6) + 2\,\mathrm{p}_2\,\mathrm{x}'\mathrm{y}' + \mathrm{p}_1(\mathrm{r}^2 + 2\,\mathrm{y}'^2) \end{aligned} \tag{3.2}$$

$$r^2 = x'^2 + y'^2 \tag{3.3}$$

where $x' = x/z$ and $y' = y/z$ are normalized undistorted coordinates of image point; k_1, k_2, k_3 are radial distortion coefficients. p_1 and p_2 are the tangential distortion coefficients considered. Higher-order coefficients and thin prism distortion are not considered in this context.

The correction process is applied automatically once each image is stored by the main system, just before the geo-rectification tasks.

Image rectification is the process used for the transformation between an originally oblique image into a plan view equivalent one (rectified image), free from deformations induced by the camera. The so-called external (or extrinsic) parameters, i.e. precise camera global coordinates and orientation are necessary.

The pinhole camera model (Figure 2.1) has been considered for this task (external calibration), which is performed in order to the transformation from the undistorted image coordinates system to the global coordinate system. Such a task has been typically solved in many photogrammetric and coastal video applications by integrating the well-known Direct Linear Transform (DLT) algorithm, by using at least 3-4 GCPs and relative image coordinates correspondences, also when including focal length (Holland et al., 1997). There are, though, several simplifications to the problem once known internal parameters, which turns into an extensive list of different algorithms that improve the accuracy of the DLT (Penate-Sanchez et al., 2013).

This is the so-called Perspective-n-Point problem, for which three point correspondences are sufficient in its minimal version (Gao et al., 2003), while solutions to the over-constrained problem with n $>$ 3 point correspondences exists as iterative (Horaud et al., 1997, Lu et al., 2000) and non-iterative solutions (Ansar and Daniilidis, 2003, Fiore, 2001). Here it is applied an iterative solver by minimizing the sum of the re-projection errors, which corresponds to the accumulated squared distances between the 3D point projection and its measured 2D coordinate. The minimization is applied by using Levenberg-Marquardt algorithm, hence the $3 * 4$ perspective transformation matrix P, Eq. (3.4) is calculated as follows:

$$P = K\ R\ [I| - C] \tag{3.4}$$

where I is the identity matrix, C and R are the translation vector and rotation matrix, respectively, of the camera Centre of View (CoV). The R retains information of the effective orientation of the CoV with respect to the Cartesian axes.

The joint rotation-translation matrix $[R| - C]$ is called matrix of *extrinsic parameters*.

3.5. Image displacement

The great meteorological variability, due to i.e. strong wind, heavy rain, or even hailstorm, human inadvertences, thermal expansion and mechanical factors could led to unexpected change of the precise camera CoV location, and this may imply the loss of information/fault in the geo-rectification procedure. The definition of a procedure in order to correct the perspective transformation P has been demonstrated to be of strong importance in order to reduce these significant geo-rectification errors (Holman and Stanley, 2007b).

So, the need of a real-time and/or one-off controls is desirable also in order to keep preserved the external calibration parameters as long as possible.

A procedure, basically build on computer vision algorithms, also inspired by Vousdoukas et al. (2011), has been defined in this context which is summarized in the following:

1. Snapshot images, taken at different illumination condition at the time of external calibration, for which camera geometry is known are selected and undistorted, in the number of $N.5/6$, referred as set I_R.
2. Snapshot images, for which the image displacement has to be calculated, uniformly distributed over a day, are undistorted, in the number of 15 around, referred as set I_D. SURF algorithm, which can be classified as a local feature detector and descriptor, mostly used for image alignment or make 3D reconstructions (Bay et al., 2008), is

applied to I_R and I_D. The characteristic feature points detected, outside those regions where fixed structures are framed, are masked/filtered out (manually).

3. The locations retrieval of matched points using SURF algorithm between the two data sets is performed, but data still includes several outliers. Identical matched points are neglected.

4. A geometric transform estimator (Hartley and Zisserman, 2003) assuming a non-reflective similarity transformation, is used in order to remove outliers by using RANSAC schema (Fischler and Bolles, 1981). The latter represents an overused method for robust fitting of models in the presence of data outliers, as the case.

5. The Procrustes analysis is performed (Kendall, 1989). This determines a linear transformation matrix M_{DR} between the points matched from the set I_D to best conform to those in the set I_R. The goodness-of-fit criterion is the sum of squared errors.

6. The undistorted coordinates of the previous/original GCPs are transformed by applying the matrix M_{DR}. The mean values of the new GCPs are used for updating external calibration and geo-rectification procedures.

The steps 4-6 are applied only in the case the number of keypoints matched in step 3 is greater than 10.

The procedure does not take into account high frequency oscillations, due to wind turbulence for example. Indeed, the latter is considered to be compensated while the Timex is composed during the 10 min acquisition period, since simple Snapshot is mostly used only for illustrative purposes.

While drifting and camera angle changes (jumps) are not yet observed during a barely year monitoring period of the systems, unlike described in (Holman and Stanley (2007a), Vousdoukas et al. (2011)).

3.6. Sea level filter

Tide gauges measure real sea levels, useful for geo-rectification procedure. In the Apulia region, AdBP hold most of wave and tide gauges deployed which are available at consultation and download on:

http://simopadb.dyndns.org/web/simop/misure.

In order to avoid the use of such raw data "as they are", not yet validated, a quasi-real-time filter is implemented. It includes:

- a filter for setting tolerance limit values between successive measurements;
- a spike filtering, using spline test adaptation applied over the measurements extracted using 16 hours temporal windows;
- threshold values filtering, according to the analysis of the multi-year validated time series (Bruno et al., 2014, Canesso et al., 2012).

The filtered water level is used for Timex image produced and shoreline processed georectification. This code is MATLAB written and automatized by using python sripting.

3.7. System applications

The AdBP, among several characteristic sites along the Apulian coast, which have been investigated for several years in order to monitor states and morphodynamic evolutionary trend, has identified two locations for further analysis by using video analysis.

The new system developed has been installed at two stations, in Torre Canne (TC) and Torre Lapillo (TL), the reader is referred to Subs. 3.7.1. and 3.7.2. , respectively, for more details.

The outline of the processes, which determine the main modules included in the new video monitoring system are detached in Figure 3.1 and includes the acquisition, processing and sharing the results on a web-tool, well linked to the Sistema Informativo Meteo Oceanografico delle coste Pugliesi (SIMOP) portal of AdBP.

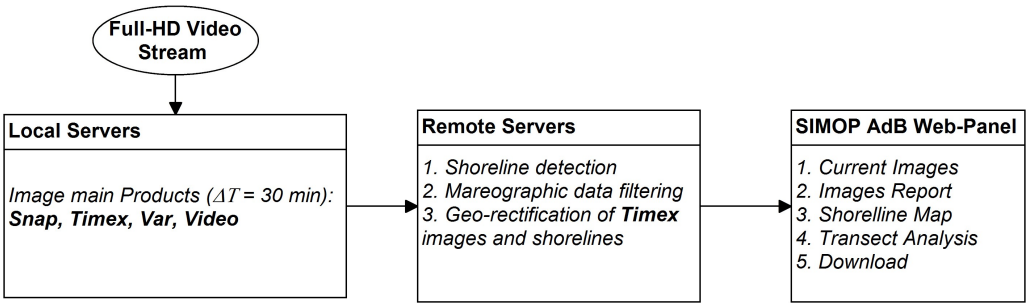

Figure 3.1 Process outline of main tasks of new coastal video monitoring system.

The stream of each camera installed is configured in such a way to collect video records of 10 min and frequency of $1\ Hz$. The sampling interval is 30 min. The main products produced and stored into the local servers are three fundamental types of images: *Snapshot, Timex* and *Variance*, better explained in Section *2.2*. The acquisition cycle is therefore 10 minute, and during this, the images acquired are hence, 600, every half an hour. The transfer to a cloud server is granted by local router connectivity.

The remote post-processing tasks are applied once each new image is uploaded. Specifically, the SDM model, described in Chapter 2 -, is implemented on the *Timex*. The sea level data filter is executed, which produce the level used for geo-rectification procedure. The latter procedure, described in Section 3.4, is performed on the *Timex*. The shoreline detected on the oblique image are geo-rectified as well. These tasks are executed and automatized by using Python scripting, partially including libraries from OpenCV, flamingo-openearth and Gdal/OSR.

Figure 3.2 shows the locations of the installed system, nearest tidal gauges and the approximate FoV of cameras.

Figure 3.2 New Video Monitoring station installed at Apulia region: Camera locations and approximate Field of View (FoV). Nearest tidal buoy (dots) of Apulia monitoring network , BR: Brindisi; PC: Porto Cesareo . Grid coordinates: RDN2008/TM33.

3.7.1. Torre Canne, Fasano (BR)

Study area

Torre Canne represents an important thermal location for Apulia region, facing the Adriatic Sea. It presents several free and private beaches characterized by medium grain size sand, according to Udden-Wentworth scale, with a mean diameter of the particle size distribution, D_{50} and a D_{95} equal to $0.28\ mm$ and $0.44\ mm$, respectively. The emerged beach is about $20 \div 50\ m$ wide, characterized by a steep berm with periodically vegetation encroachment.

The wave climate in the area is moderate, with an annual significant wave height (H_s) ranging from $0.5\ m$ to $1.5\ m$ for the $49.75\ \%$ of wave observations in $1990\text{-}2007$. Only the 0.16% of the measured waves heights exceeds $3.5\ m$. A peak period from $3\ s$ to $7\ s$ constitutes the 67.6% of observations. The analysis of wave climate shows that waves approach from NNO for the 29.7% of the time, while a discrete contribute of the sector ESE occurs for around 18% (Petrillo and LIC, 2010).

The great urbanization rate, mainly due to touristic activities, has been crucial in increasing the negative sedimentary balance of the area (AdB-Puglia, 2015). Indeed, in the last decade, the analysis of long-term shoreline movements, highlights a global erosional trend, with maximum shoreline withdraws equal to about $10\ m$ at few spots, which, recently, has become quite stable. Coastal vulnerability assessment in this area is of great interest because of the tourism economy of this coastal stretch, which represents a great resource for local community.

System Implementation

At TC site, two IP network cameras are installed on a steel pole, which is fixed by brackets on parapet, at the roof of the "Hotel del Levante". The approximate orthometric height of the cameras is $23.4\ m$ (ITALGEO2005).

In Figure 3.3 the installed cameras and coastal stretch under investigation framed are shown.

The system placed at Torre Canne consists of one thermal (TC_{th}) and one visible (TC_{vs}) cameras, both faced NNW, with a FoV of $10°$ and $59.5°$, respectively. The TC_{vs} is an Axis, Mod. Q1765-LE Network Camera, TC_{th} is an Axis, Mod. Q1931-E Thermal Network Camera. Both visible and thermal are outdoor-ready network cameras. The TC_{vs} is equipped with CMOS RGB Progressive Scan $1/2.9$ sensor, and delivers HDTV $1080p$ video in multiple, individually configurable $H.264$ and Motion JPEG video streams and have a built-in IR illumination. Moreover, visible camera has 18x optical motorized zoom and auto-focus. The corresponding single frame resolution is $1920 \times 1080\ pixel$.

The TC_{th} provides thermal imaging, with an Uncooled Micro bolometer 384×288 sensor (image can be scaled up to 768×576), a noise filter which gives improved thermal image contrast while keeping noise levels low.

The system includes a local server, which is a HP ProLiant MicroServer Gen 8, 1Tb storage drives, in the number of N. 2 and one router, model D-Link's Wireless N150 4G LTE for data transmission.

During the installation phase, a collection of reference images for internal and external calibration tasks has been gathered. Specifically, intrinsic parameters are estimated by imaging a well-defined pattern from different angles and distance. Checkerboard patterns are typically used for calibration, since they provide easily detectable features, the intersections between the black and white squares form high contrast points, estimated with sub-pixel accuracy. Hence, for visible cameras the pattern used is a classic paper chessboard over a smooth plane, in Figure 3.5 representative images used are shown.

Figure 3.3 **Right:** Cameras location in Torre Canne (TC) and the coastal stretch framed; **Left:** Cameras installation.

While, the use of different emissivity materials has been proposed for the internal and external calibration pattern of TC_{th}. Since low emissive materials would appear colder than high emissive, aluminium foil tape stuck on paper, as highlighted in (Engström et al., 2013), is used. The Figure 3.4 shows the thermal patterns used for internal and external calibration procedures, at the top and bottom, respectively.

Results from the calibration procedure show that the lens deformation is dominated by the radial component, which errors become larger than 30 pixels at the outer edge of the original image, while the errors related with the tangential component are always lower than $1\ pixel$. The computed average error of re-projection is calculated as always less than $0.52\ pixel$.

Camera external orientation is estimated by using eight to ten GCPs, for each cameras, among fixed structures and as movable target, a $1\ m^2$ chessboard pattern (classic and mixed aluminium/paper) using unique central intersection between squares.

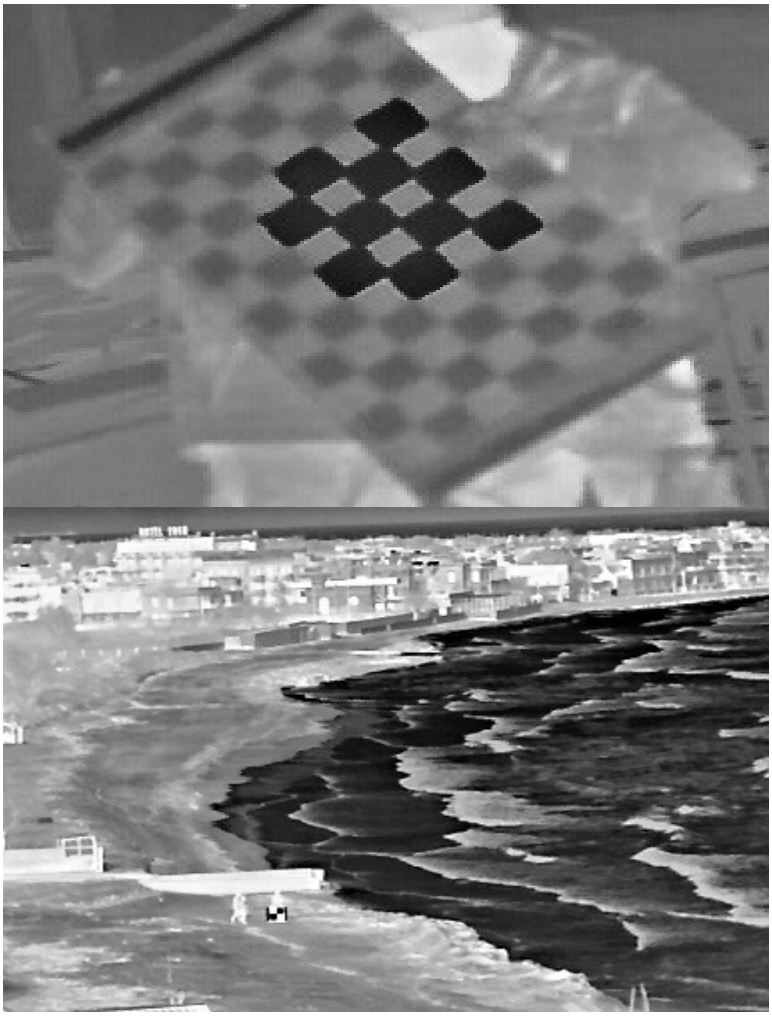

Figure 3.4 **Top:** Paper/Aluminium chessboard for internal calibration; **Bottom:** Example of Pattern used as GCP in order to perform external calibration procedure for thermal camera.

Figure 3.5 **Top:** Classic paper chessboard for internal calibration; **Bottom:** Example of Pattern used as GCP in the external calibration procedure for visible camera.

Pixel footprint, which gives us the dimension of each pixel in the geographic space, is represented as example in Figure 3.6, and shows the typical contrast between along-shore and cross-shore components.

The near-alongshore footprint is more sensitive to the distance from the camera and ranges from a decimetres to around $13\ m$ when the distance is less than $1\ km$; on the other hand, the near-cross-shore component is generally under the $1\ m$ in the principal target area. Increasingly the geo-rectified area would decrease the positional accuracy.

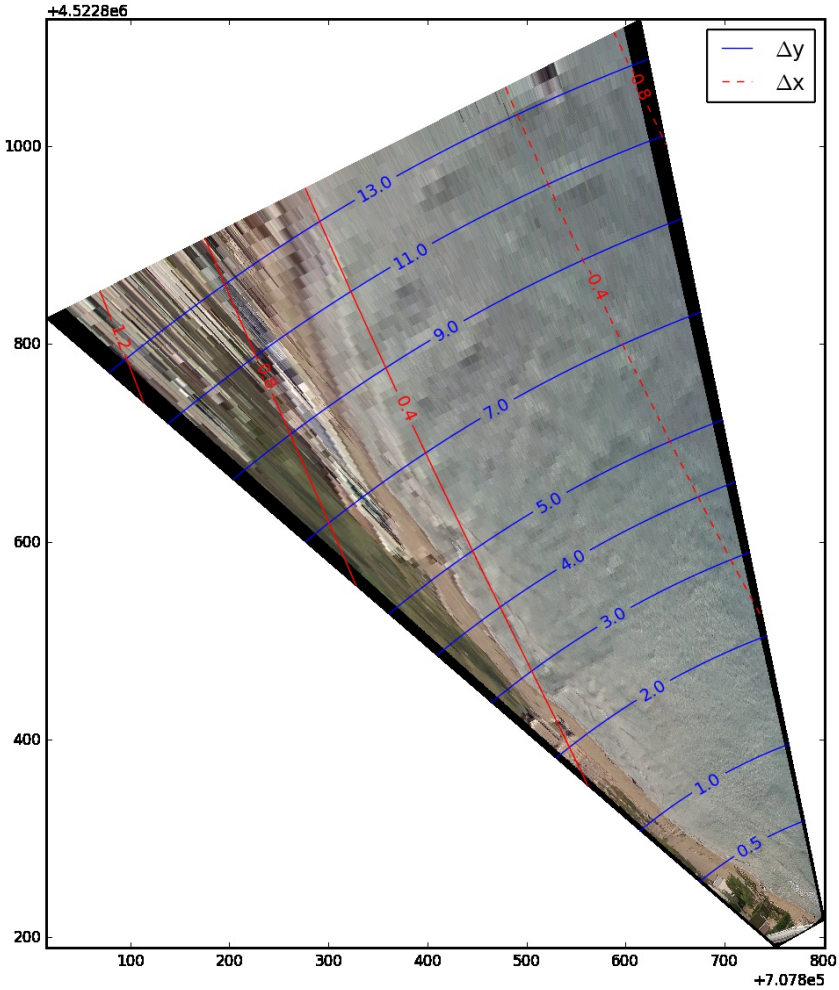

Figure 3.6 Pixel footprint (m) across Torre Canne (TC) study site, along 800 m beach stretch. Black lines: almost alongshore component (Δy); red solid and dashed lines – cross-shore component (Δx) .

3.7.2. Torre Lapillo, Porto Cesareo (LE)

Study area

The Marine Area of Porto Cesareo is an interesting site from a morphological point of view. This area is constituted by typical sub-environment of low-lying coasts, with calcarenitic rocky and sandy beaches. The embayed beach of Torre Lapillo has its typical asymmetric planform shape, characterized by quite strongly curved zone (at NW), a gently curved centre (where coastal video-monitoring is installed) and a relative straight section (at SE). Sandy beaches are characterized by a mean diameter D_{50} almost equal to $0.47\ mm$ and D_{95} to $1.38\ mm$. Sandy beaches are characterized by a mean diameter D_{50} almost equal to $0.47\ mm$ and D_{95} to $1.38\ mm$.

Since the first 60's, the number of establishments has been increased in the geographical area of Porto Cesareo, with remarkable damages of emerged beach, especially of dunes. The establishments' managers applies a common defence practice during the winter season, by means of geotextile sandbags which are uniformly distributed just few meters close to coastline, determining a morphological change in shapes of the ordinary and stormy berms and reducing shore erosion. It has been revealed that the main reason connected to the erosional trend in the period 2009 - 2011 could be related to the mean sea level rise (about $13\ cm$) , amplified by significant storms occurred (AdB-Puglia, 2015). Particularly, the shoreline erosional hotpots are located in southeast, where in $2013 - 2015$ the cumulative sediments balance resulted less than -10 m.

For the majority of the time ($49.7\ \%$) the waves approach from SSE, while for $34.8\ \%$ they come from SW direction. The wave climate in the area is moderate to low, with an annual significant wave height less than $0.75\ m$ for the $44\ \%$ of observations in $2006 - 2013$, while a $12.17\ \%$ for $0.75 < Hs < 1.75\ m$ and only the 0.66 % with $Hs \geq\ 3.0m$ (AdB-Puglia, 2015). The peak period T_p in the interval $3\ s$ to $5\ s$ represents the most frequent ($31.9\ \%$ around).

System Implementation

At Torre Lapillo site, hamlet of Porto Cesareo, two IP network cameras are installed on a steel pole, fixed on parapet, at the roof of the restaurant establishment "Bacino Grande" (Figure 3.7). The approximate orthometric height of the cameras is, in this case, $7.5\ m$ (ITALGEO2005).

Figure 3.7 **Right:** Cameras location in Torre Lapillo (TL); **Left:** Cameras installation and the NW coastal stretch monitored.

The video-station placed at PC (Figure 3.7) includes a couple of identical visible cameras (PC_{vs1}, PC_{vs2}). The first one stared at NW direction, with FoV equal to $51.6°$, while the second one faced to SE direction, with a FoV of $56.2°$. Both are Axis, Mod. Q1765-LE Network Cameras. The same hardware equipment, as TC shore, is installed.

The pixel accuracy for both cameras in the alongshore component ranges from few centimetres to around $14\ m$ when the distance is less than $700\ m$, while near-cross-shore footprint is generally lower than $2\ m$. System accuracy depends, among others on the pixel footprint, the calibration and geo-rectification procedure, stability of camera over time, etc. In order also to evaluate overall new system positional accuracy, differences in the position of a set of $6\ GCPs$ are computed, taken at distance from the

camera ranging from 10 to $300\ m$. Results show significant differences between cross-shore and alongshore positional accuracy, with a root mean square error ($rmse$) of $0.43\ m$ and $5.21\ m$, respectively. The error is mainly related to the pixel footprint, with the longshore accuracy error that significantly dominate, as expected.

When the system is used in the extraction of intertidal bathymetry, the vertical error is further reduced as foreshore slope is generally 0.1 or around this value, translating in the reduction of the error by an order of magnitude (Silva et al., 2009).

The new Shoreline Detector Model (SDM), presented in Chapter 2 -, is tested at the new video systems and presented here for the case of PC shore, aimed at validation of results, by comparing manual shoreline contours with the automatic extracted ones. The intertidal bathymetry calculated from the SDM is then compared with GPS-RTK field surveys.

As for the Alimini testing dataset, the SDM is validated by using 15 Timex images recorded in the first months of system working, representative of main illumination and wave conditions for both cameras, calculating the relative distance on 40 transects in pixel space. In the Figure 3.8, the box plots for each analysed image are displayed. The results show that the SDM algorithm calibrated and validated at Alimini could be extended at different sites, characterized by different morphological features and site geographical exposition. The Table 3.1 reports the mean overall statistics at PC.

The mean overall pixel distance ($mean_{\Delta}$) is about 1.17 px, while the mean of maximum values over all the images (max_{Δ}) is about 3.77 px. It can be noticed that all datasets are approximately balanced around 1.2. However, there is substantially more variation

Table 3.1 Main statistics (pixel space) at PC

$mean_{\Delta}$	max_{Δ}	min_{Δ}	$median_{\Delta}$	std_{Δ}
1.17	3.77	-1.7	1.22	1.16

in some images datasets with a maximum range approximately from -5.5 to 7.3 for image n. 6, whereas data relative to images 27 show the minimum range approximately

from -1.3 to -0.9. As for Alimini, in most images the sample dispersion is close to the median. Outliers are almost completely associated with the presence of sand bags.

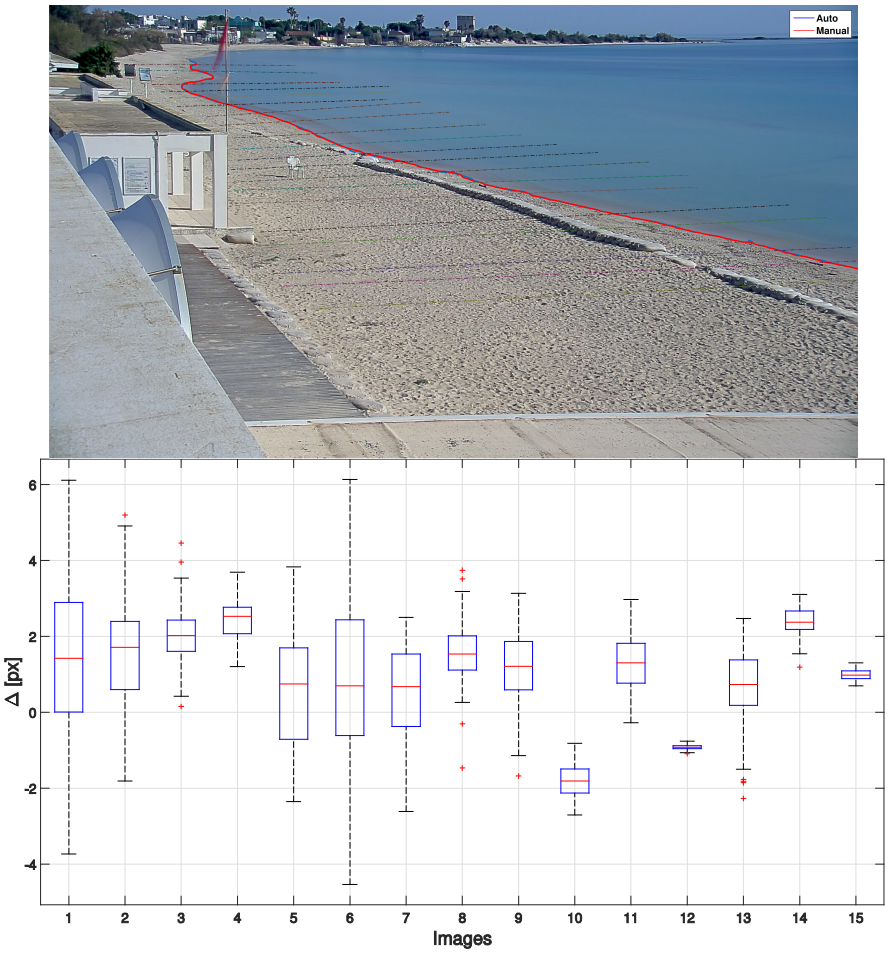

Figure 3.8 **Top:** Example of comparison between manually and automatic shoreline contours with transects overlapped (cam PC_{vs1}); **Bottom:** Statistic box plots of results for 15 images analysed.

Actually, when at certain locations, the pixel distance from the offshore limit of bags and shoreline is low, less than around 2.5 pixels, the probability of boundaries detector could lead to a single result in that neighborhood, which propagates in cascade until the last step of correction (Section *2.4.5.*) into the main routine. This issue is often associated with high illumination condition.

Intertidal Bathymetry estimation

Several authors approached the determination of the intertidal bathymetry of beach from video system. Previous works, since first experiences (Aarninkhof et al., 2003, Davidson et al., 2007, Plant and Holman, 1997), based the intertidal reconstruction on the shoreline geo-rectification at elevations derived from site-specific parameterization of the total water level referred to the offshore wave height (Uunk et al., 2010) or breaking wave height (Vousdoukas et al., 2011) and different models for set-up and swash contributions.

The process presented here in order to test the new system is based on the Digital Elevation Model (DEM) reconstructed by geo-rectifying the time-varying shoreline position over a tidal cycle, by using the filtered sea level, as above described. In order to test the code, the intertidal bathymetry evaluation has been performed in quite wave condition, in order to neglect wave set-up and swash effects. The extracted contours, automatically stored also as shapefiles for being digitized in GIS environment for further analysis, have been processed by using Triangulated Irregular Network (TIN).

A Real Time Kinematic survey using differential GPS solution on the Global Navigation Satellite System (GNSS) of Apulia Region is conducted along the beach stretch monitored until around 300 m, in order to measure the beach profiles over 16 cross-shore transects. The measured profiles are then compared with the intertidal bathymetric profiles extracted from the reconstructed DEM, obtained from video analysis one day later the survey.

The evaluation of the intertidal bathymetry profiles can be sketched as follows: (i) automatic shorelines detection over the Timex oblique images; (ii) sea level time-series filtering (Section 3.6); (iii) shoreline geo-rectification; (iv) DEM reconstruction and transects extrapolation. The Figure 3.9 highlights the transects positions and few automatic detected shorelines, overlapped on a portion of rectified snapshot image framed by PC_{vs1} camera FoV.

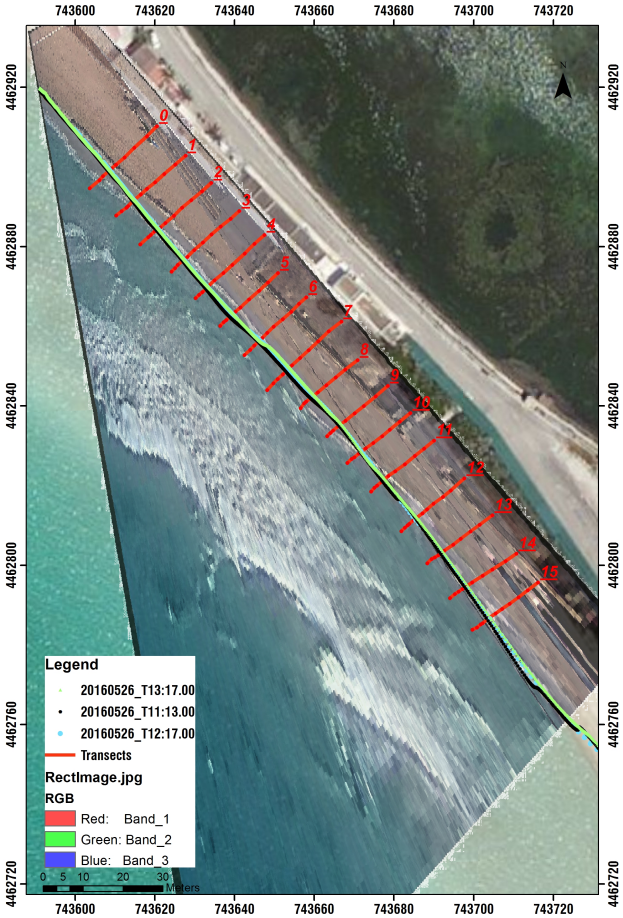

Figure 3.9 Cross-shore transect (red pointed GCPs and sections), examples of automatic shorelines overlapped on a snapshot geo-rectified image.

The Ionian Sea is generally characterized by low tidal amplitude oscillations, ranging from 0.1 m ÷ 0.6 m below the still water level. For this reason, due to the mean beach slope equal to about 10%, the mean projected horizontal distance investigated is equal to around 2 m, with a maximum vertical excursion of around $0.25\ m$.

In Figure 3.10 (top), as an example, both measured (solid lines) and calculated (dashed lines) profiles are reported for the transects n. 0, 4, 5, and 11.

The comparison shows a quite good agreement between measured (solid lines in) with a mean, overall transects, RMS error equal to 0.025 m. Calculated profiles are almost linear with respect to the measured ones. In reality, the lowest RMS error (equal to about $0.005\ m$) occurs for transect n. 11, which is characterized by a linear beach

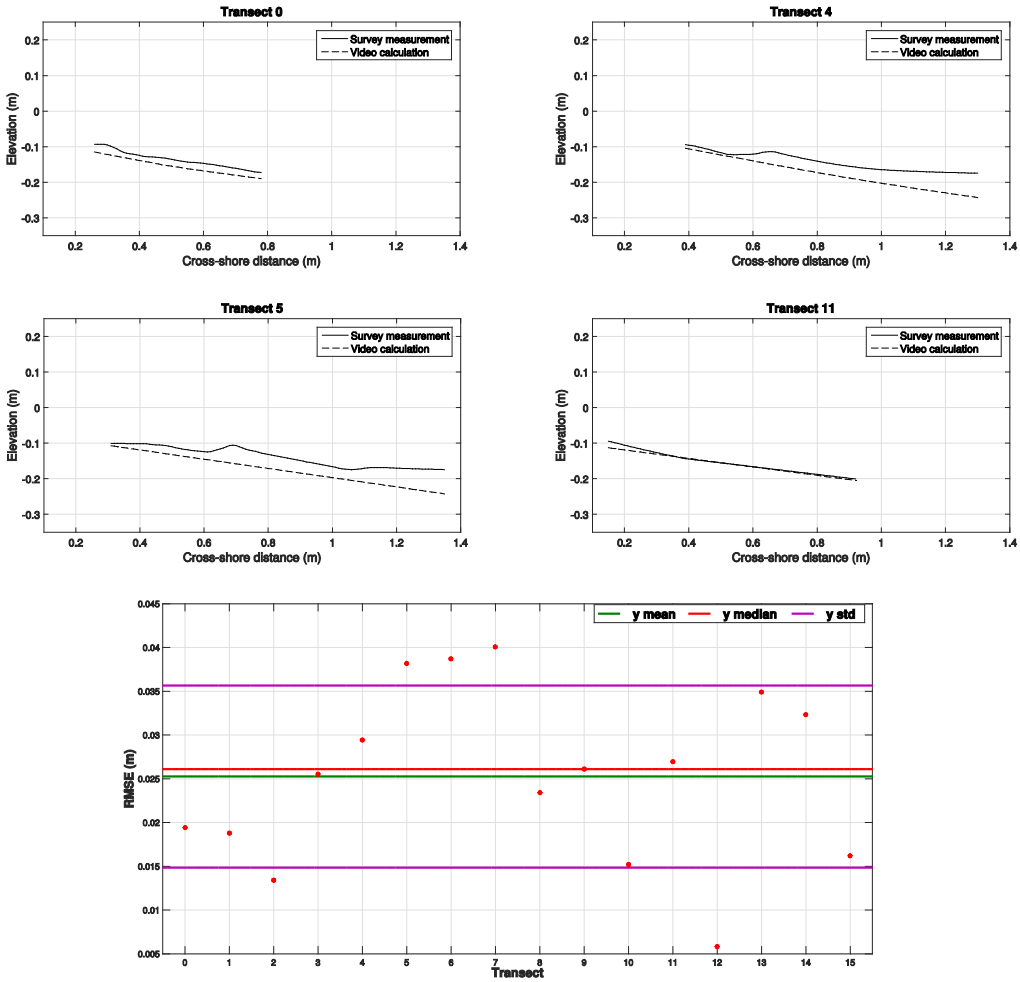

Figure 3.10 ***Top:*** Comparison of intertidal bathymetry derived from video analysis with the field measured profiles for transects n. 0, 4, 5 and 11 (see Figure 3.9). **Bottom:** Vertical RMS error (m) for all transects analysed.

profile. The greatest errors (i.e. transects n. 4, 5 and 6 of about $0.04\ m$) can be observed when beach profiles present small changes in elevation ($\sim cm$).

Such results, seem to be fully comparable with respect to the previous studies performed on beach intertidal bathymetry reconstruction, mainly deployed on beaches characterized by a higher tidal amplitude. In fact, by using Argus system, Aarninkhof et al. (2003) obtained errors lower than $0.15\ m$ along 85% of the $2\ km$ beach. Plant and Holman (1997) reported $0.24\ m$ vertical RMSE, latter corrected to 0.06 m when empirical corrections of water level were made and Vousdoukas et al. (2011), using an automated video system with two MOBOTIX cameras, found an vertical RMSE of $0.22\ m$ for a five-month period of fully automated operation.

Image displacement correction

The procedure for image displacement has been tested in this study only in the event of a human-accident displacement, during maintenance operations. Consider this, in the 5th step of Section 3.5, the reflection and scaling factors are assumed to be null, since undistorted images are used and the influence of thermal expansion neglected. Blend overlapping figures, representative of the transformation applied on PC_{vs1} camera at the station of PC is shown in Figure 3.11. Estimated accuracy after the correction is overall below $0.4\ pixel$.

3.8. Web-tool

The possibility of sharing the on-going results of coastal video-monitoring is quite promising, supporting professionals and coastal managers in morphological analysis. Furthermore, beach-users and stakeholders may be aware on actual beach state and relative evolution. This has led to the construction of a web-portal (http://91.121.30.84), which includes the publication of results in a quasi-real time, by using the schema described above (Figure 3.1). The web-site is specifically built by using JavaScript and coded HTML, and it is a 1.0 version, released and included into the main AdBP coastal web-area (simopadb.dyndns.org/web/simop).

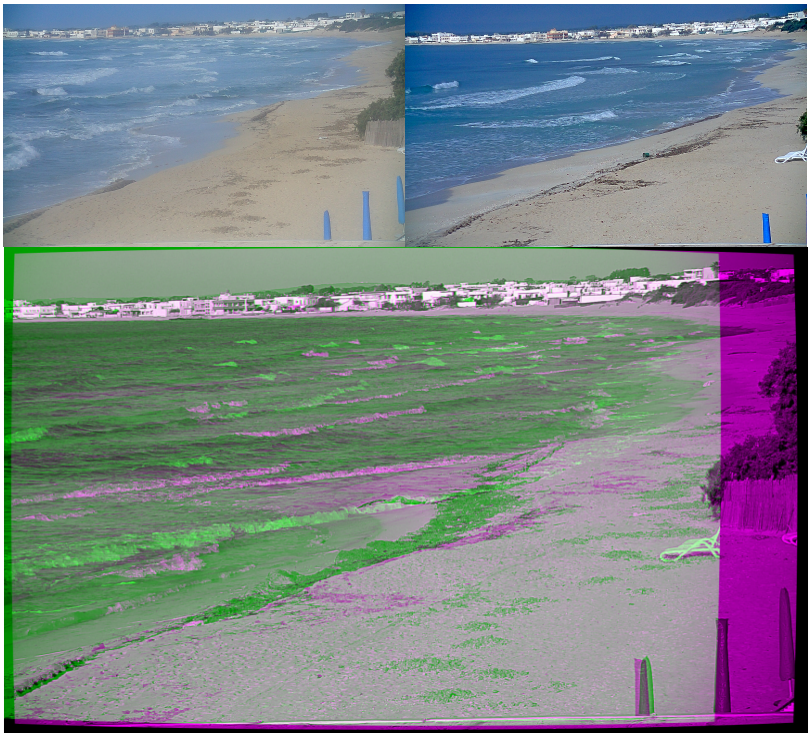

Figure 3.11 **Top left:** Original image at the time of external calibration; **Top right**: Image displaced; **Bottom**: Overlay of original registered image over displaced one, by using alpha blending, showing high accuracy (green channel).

It consists of 5 modules of different consultation tabs. The "*Current images*" tab is intended to list the last images produced at all the stations of the system, among those produced (Snap, Timex, STD and geo-rectified); the "*Images Report*" allows user to view thumbnails and download images, choosing interval and extremes date of a time period . "*Shoreline map*" tab permits a mapping of the geo-rectified shoreline, as dots, over the rectified geo-referenced image; while "*Shoreline Transect Analysis*" is a tool able to plot the shoreline distance to a baseline over time, after a transect is chosen from a list, displayed also over the oblique image (Figure 3.12). The "*Download*" tab allow users to download all the data produced by the monitoring stations (Valentini et al., 2016).

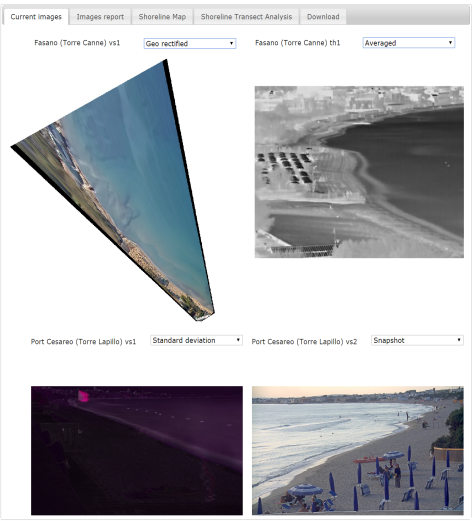
Current images
Images report
Shoreline Map
Shoreline Transect Analysis
Download
Fasano (Torre Canne) vs1
Geo rectified
Fasano (Torre Canne) th1
Averaged
Port Cesareo (Torre Lapillo) vs1
Standard deviation
Port Cesareo (Torre Lapillo) vs2
Snapshot

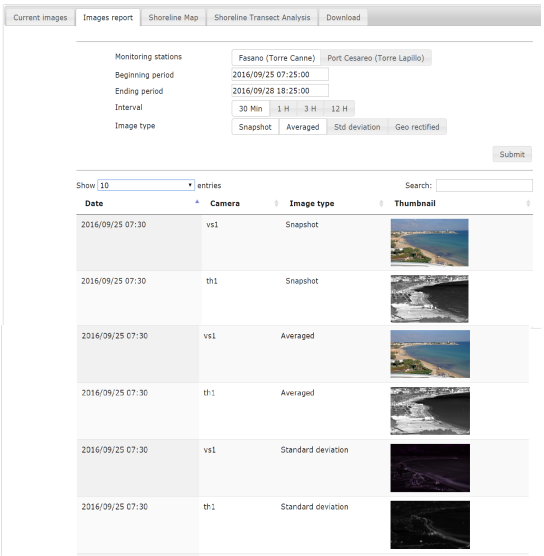
Current images
Images report
Shoreline Map
Shoreline Transect Analysis
Download
Monitoring stations
Fasano (Torre Canne)
Port Cesareo (Torre Lapillo)
Beginning period
2016/09/25 07:25:00
Ending period
2016/09/28 18:25:00
Interval
30 Min
1 H
3 H
12 H
Image type
Snapshot
Averaged
Std deviation
Geo rectified
Submit
Show 10 entries
Search:
Date
Camera
Image type
Thumbnail
2016/09/25 07:30 vs1 Snapshot
2016/09/25 07:30 th1 Snapshot
2016/09/25 07:30 vs1 Averaged
2016/09/25 07:30 th1 Averaged
2016/09/25 07:30 vs1 Standard deviation
2016/09/25 07:30 th1 Standard deviation

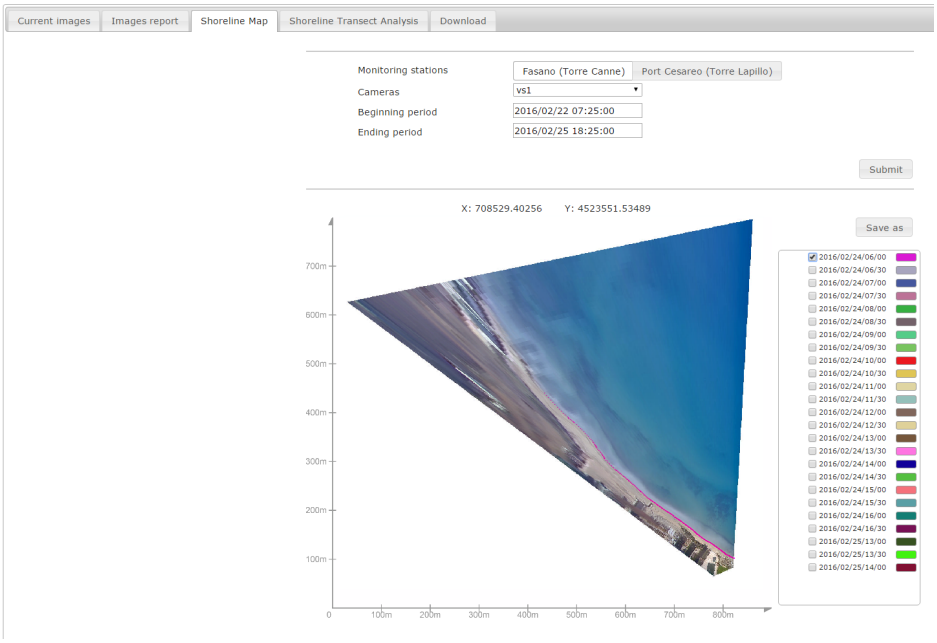
Current images
Images report
Shoreline Map
Shoreline Transect Analysis
Download
Monitoring stations
Fasano (Torre Canne)
Port Cesareo (Torre Lapillo)
Cameras
vs1
Beginning period
2016/02/22 07:25:00
Ending period
2016/02/25 18:25:00
Submit
X: 708529.40256
Y: 4523551.53489
Save as
700m
600m
500m
400m
300m
200m
100m
0
100m
200m
300m
400m
500m
600m
700m
800m
2016/02/24/06/00
2016/02/24/06/30
2016/02/24/07/00
2016/02/24/07/30
2016/02/24/08/00
2016/02/24/08/30
2016/02/24/09/00
2016/02/24/09/30
2016/02/24/10/00
2016/02/24/10/30
2016/02/24/11/00
2016/02/24/11/30
2016/02/24/12/00
2016/02/24/12/30
2016/02/24/13/00
2016/02/24/13/30
2016/02/24/14/00
2016/02/24/14/30
2016/02/24/15/00
2016/02/24/15/30
2016/02/24/16/00
2016/02/24/16/30
2016/02/25/13/00
2016/02/25/13/30
2016/02/25/14/00

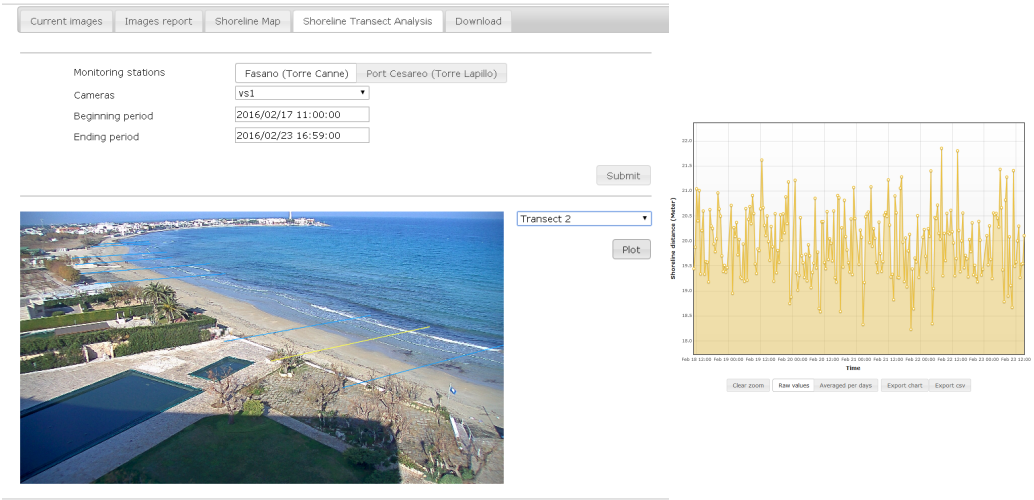

Figure 3.12 **Top Left to right:** *Current Images* and *Images Report* tabs; **Middle:** *Shoreline Map* tab used for mapping shoreline on geo-rectified images (pointed lines); **Bottom Left to right:** Cross-shore transect user-selected and shoreline distance from baselines plotted over time.

3.9. Conclusions

Nowadays, risk assessment plays a fundamental role in preventing irreversible erosion processes as well as flooding damages. In this context, the video monitoring represents a low-cost instrument to store a large amount of data, due to the feasibility in extracting several morphodynamic and hydrodynamic measurements from images/videos. In this chapter, a new coastal video monitoring system deployed and integrated in the Apulia Region Monitoring Network (South Italy) is presented, which is born to work completely automatically.

In 2015, two new video stations were installed at two sites along Apulian coasts in order to study both morphodynamic and hydrodynamic processes affecting the coast. For this reason, a new model (SDM) for image processing has been developed, aimed at extracting shoreline from Timex oblique images. The procedure is mainly based on the recognition of sea/sand contour from an automatic segmented area. The SDM has been firstly calibrated and validated (see Chapter 2 -), and then tested on images derived from different video systems, facing sites characterized by different geographic expositions and illumination conditions, such as Torre Lapillo site. Such a procedure

demonstrates the feasibility of the model to be extended at different sites, giving good results in shoreline detection, quantified by comparing manual and automatic shorelines.

Another strength of the system is the dissemination of results on a web portal, freely accessible. In quasi-real time, users can view and download, for free, processed images from all the cameras installed, shoreline maps with different time intervals and time shoreline variation on user-specified transects, in cross-shore direction. A specific routine has been developed, allowing the automatic geo-rectification of images with respect to the sea level registered by the nearest tide gauge, opportunely filtered.

Several coastal information can be provided from images. In the present chapter first results on intertidal bathymetry derived from video analysis is presented. The vertical precision in coastal features extraction obtained is quite similar to other systems and comparable to standard surveys methods. The comparison with d-RTK GPS survey shows a good agreement, with a mean RMS error, overall investigated transects, equal to $0.025\ m$.

Moreover, a thermal camera has been installed in TC shore mainly with the twofold purpose of: (i) support the visible stream during nightlight hours in order to monitor beach, particularly on severe events and (ii) implement the segmentation of the upper part of intertidal area for studies of potential sources of Aeolian sediment (Hoonhout et al., 2013) by using the Global Probability of Boundary method.

The overall results are very encouraging in what concerns this new video system application in the long-term monitoring of beach systems.

Future system developments include the integration of routines for linking the exact wet/dry interface elevation to more specialized hydrodynamic model results in order to take into account swash prediction, then for estimating beach state and the design of a communication infrastructure that will enable to use the new system in a real time coastal hazard warning system. The latter task will be eased by the use of standard IP surveillance cameras, a domain where most of communication operational issues have already been solved.

CHAPTER 4

UNMANNED AERIAL VEICHLE (UAV) APPLICATION FOR BEACH DSM RECONSTRUCTION

Chapter 4 - UNMANNED AERIAL VEICHLE (UAV) APPLICATION FOR BEACH DSM RECONSTRUCTION

4.1. Introduction

This chapter aims at describe the creation of point cloud and validation of a Digital Surface Model (DSM) of a beach system, in the location where a new video monitoring system is installed. A briefly introduction on the solutions for coastal environment DSM reconstruction is presented, then material and methods adopted in this context are described, so results and at last, discussion and concluding remarks highlighted.

Nowadays, in contrast with traditional techniques useful for accurate representation of coastal topography, geomorphology and its evolution assessment, the Unmanned Aerial Vehicle (UAV) equipped with imaging sensors is being constantly investigated.

Briefly, standard instruments for foreshore DSM reconstruction are represented by airborne Light Detection And Ranging (LiDAR) and TLS, whose results are very detailed and straight forwarded for coastal applications.

Airborne techniques have the advantage of providing large coverage and good accurate topography (point cloud or orthophotos), but they have the particular features of having high costs and logistic constrains. Furthermore, for short-term evaluation of topographic changes, due to e.g. significant storm impacts, it is quite impossible to perform surveys evenly repeated in time or each time it is necessary. By using the alternative of proximity survey, TLS can achieve greater accuracy, instead smaller area is covered, hence, more surveys and very long processing time is required for large extension. Furthermore, the oblique acquisition procedure, which is more often undertaken, has been demonstrated to lead to errors/inaccuracies when sudden changes on topography are encountered (Casella et al., 2014, Mancini et al., 2013, Naumann et al., 2013).

The work of Gonçalves and Henriques (2015) discuss and summarize different advantages of the UAVs with respect to traditional tools as related to: i) the high level of automation of photographic survey; ii) a very low operating cost; iii) the easiness in

repeatability of the survey and iv) the possibility to obtain orthomosaic with centimetric resolution. UAV applications for 3D reconstruction spans from the historical heritage and archaeology, forestry and agriculture, topography, etc. In addition, UAV for coastal environment has been approached (Gonçalves and Henriques, 2015, Harwin and Lucieer, 2012, Long et al., 2016, Mancini et al., 2013). Specifically, while analysing the point cloud generated from UAV imagery of coastal environment, Harwin and Lucieer (2012) deal with a workflow based on patch-based multi-view stereo software (Furukawa and Ponce, 2010). Long et al. (2016) by means of three subsequent campaigns analysis, study erosion/accretion behaviours of a lagoon-inlet system; Gonçalves and Henriques (2015) asses and quantify a low-cost hardware equipped solution for topographic monitoring of Portuguese beaches. Mancini et al. (2013) demonstrate, by comparison with DSM TLS-derived, the great and comparable accuracy that could be achieved.

The latter three works are based on the application of the software Photoscan and his routines. This software includes and uses the Structure from Motion (SfM) method, borrowed from computer vision field, aimed at reconstruct 3D scene geometry and often not calibrated camera motion from a set of images of a static scene by using matching features on multiple images (Bay et al., 2008). With respect to classical photogrammetry, where a well-defined strategy of the images acquisition phase has to be designed, an unconstrained and unstructured imagery acquisition could be possible (Fonstad et al., 2013).

The UAV imagery combined with SfM method has been applied in this study for twofold purposes. It is well known that beach system, while imaged by a proximity aerial survey or video monitoring system, shows a great variability mainly in terms of contrast and prevalent histogram bands. This behaviour combined with the presence of low vegetation, small-sized ripples, geotextile bags filled by sand, algae blossom, which are very common in Apulian region, makes the opportunity of evaluate the UAV accuracy on a Ionian facing beach, a challenge. This acts as pathfinder for a near future well-defined

monitored programme, which would plan frequent surveys in order to detect and quantify associated morphological changes, for an efficient coastal zone management.

The high resolution beach assessment is quite important also for single or multitemporal elevation dataset that serves as input data for numerical models. A second purpose (better discussed in Chapter 5 -) is, indeed related to the effective chance of developing a modelling tool, which includes concatenated hydrodynamics models (2-d wave-flow for run-up modelling) and topographic input via low-cost and effective DSM UAV-generated.

4.2. Study area

The study area corresponds to a stretch at the centre of Torre Lapillo embayment, hamlet of Porto Cesareo. A coastal video monitoring station, deployed by the AdBP, is installed in the same area (Chapter 3 -). The reader is referred to Subs. 3.7.2. for further details about the morphological environments and main characteristics.

4.3. Materials and methods

4.3.1. The UAV Technical specification and Features

The UAV data used in this study are obtained using multicoter Aeromax 300, developed by the Microgeo Company (Florence, Italy). Areomax is an autonomous UAV with onboard intelligent artificial system, which analyses information from Intertial Measurement Unit (IMU) and on-boarding GPS in order to optimize flights. It is equipped with 4 arms and 8 motors, and characterized by full carbon/aluminum structure, not more than $2.5\ kg$ as maximum weight for full equipment. A Ground Control Station linked ($2.4\ GHz$) by a modem is characterised by few channels. Furthermore, telemetry for real-time control allows communications between the software/pilot and the UAV up to a distance of $1 \div 2\ km$, the path-tracking is also available on video sources. Flight modes available are standard waypoints-based or by wireless control.

The battery pack are 2 $Lipo\ 4S$ ($4500\ mAh$) connected in parallel, which provides at maximum $12\ min$ operative flight, with the upmost payload.
The aircraft is equipped with a two axes stabilized "GIMBAL" camera support, particularly optimized for a compact camera acquisition system, with tilt and roll damping system. The Sony Exmor™ APS HD camera, with 20.1 c CMOS sensor, defines the acquisition hardware. Its actual focal length ranges from 16 to $50\ mm$.

Figure 4.1 The UAV multicopter (photo taken by Eng. Luigi Pratola, LIC).

The flight is operated with PC Ground Station DJI (http://www.dji.com/pc-ground-station), useful because of its intuitive interface, google 3D maps support, real-time flight monitoring, photogrammetric tool option enabled. Specifically, the latter allows to simulate the flight before the mission in order to define all the parameters, among others the height of the flight, the overlap between consecutive images and/or the images resolution. The number of photos, surface covered and time of flight are also calculated for an easy consultation by user.

4.3.2. Ground Truth Survey (d-RTK)

In natural environments such a beach system, and more generally coastal areas, time-invariant targets are difficult to be deployed. So, artificial targets are used in this study:

white/black chessboard-structured pattern of plasticized paper sheets are deployed on the ground and are partially buried because of the wind.

A Real Time Kinematic survey using differential GPS solution on the Global Navigation Satellite System (GNSS) of Apulia Region is carried out on 26th May 2016, together with the UAV flight activity. The Leica GS14 antenna, receiving on telescopic rod AT450N, both manufactured by Leica Geo-Systems are used, coupled with the CS20 Disto palmar for activities viewing and checking.

Eleven GCPs, consisting of chessboard pattern materialized on plasticized paper sheets, sized A4 have been uniformly disseminated on the study area, and 97 Validation Points (VP) evenly distributed on several (16) cross-shore transects chosen along the examined beach extent have been selected for further processing. The above mentioned dataset has been evaluated in terms of horizontal and vertical accuracies and the RMS results of 0.0067 and $0.013\ m$, respectively, for all the sampled points.

With respect to the VP survey points procedure, the tie of the rod used, which measure $0.06\ m$ in his length, has not been perfectly stuck on its base, but rather penetrated for part of his length (due to device weight). This has been taken into account by choosing a constant value $(0.04\ m)$ added to the original measured orthometric height.

The horizontal coordinates are referenced to UTM Zone 33N (ETRF2000), and the vertical values are referred to mean sea level by using the ITALEO2005 of Italian Geographic Military Institute (IGMI). The location of the GCPs and VPs used in this contest are shown in Figure 4.2, the study area is defined by the black dashed perimeter.

The surveys and instrumentation equipment have been supported by the AdBP personnel.

4.3.3. Image acquisition

With the aim of solving the spatial topography, the flight planned covers almost the whole study area in Figure 4.2. It is realized at a low altitude: $30\ m$ above the ground level, expecting a high spatial resolution of released results. For this field campaign, the

focal length is set to $16\,mm$, combined with altitude lead to images with a spatial resolution of $0.0044\,m$. The survey lines are planned using Google Earth maps (plugin DJI Ground Station) dated 2015, acquisition is automatically set at one shot per second.

The automatic flight through waypoints is enabled during the survey, the “Stop and Turn” mode is set with an hold time on waypoints of $3\,s$, except for landing stage.

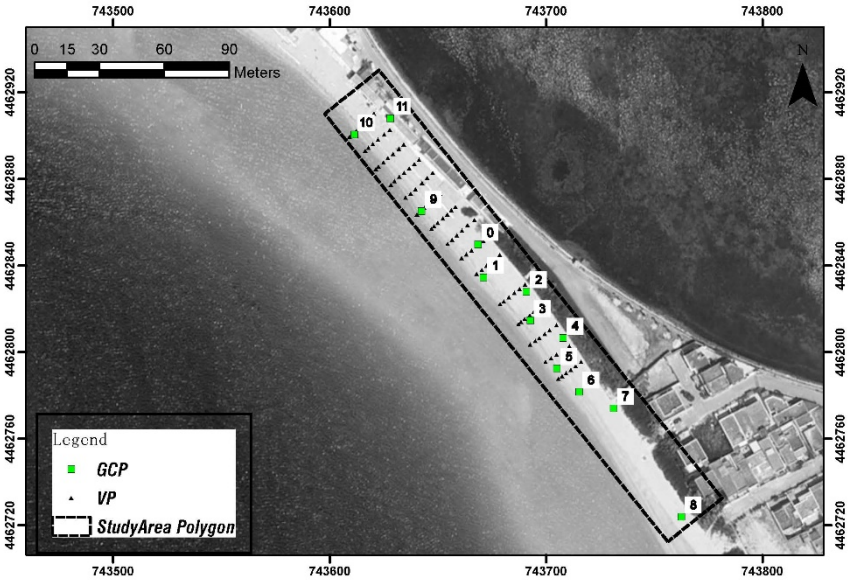

Figure 4.2 Study area highlighted. GCPs used as reference points (green square); VPs for validation purposes as black triangle.

The landing operation is quite complicate in such an environment and the sands can create damages, so this issue is solved by applying a manual driving mode and by using the large smooth top cover of UAV box as base support.

The cross-shore images overlap is 65% and the along-shore is set at 70%. The few images acquired during the take-off and landing operations are filtered out in the post-processing stage, as suggested in (Mancini et al., 2013). The pilot approaches also a manual shooting mode since he notices trough joystick, the camera acquisition had some issues. This does not compromise the results.

The meteorological conditions, which represent a potential limitation for the flight, are measured at the nearest anemometer station of Porto Cesareo hold by AdBP and are extremely calm. The recorded wind is regular with an average speed around $3.5\ m/s$, and a prevalent direction of $270°$ North, hence the UAV does not encounter in changes on trajectories.
Around 119 photos are recorded to cover this area of around $10{,}000\ m^2$.

4.3.4. Photogrammetric process

The 3D analysis of the topography is required for the use of such a system. In order to reconstruct the area, a photogrammetric process based on the SfM algorithm is approached. As introduced above, the SfM can be described as a photogrammetric method for creating three-dimensional models of a feature or topography from overlapping two-dimensional photographs taken from many locations and orientations (stereoscopy) to reconstruct the photographed scene. The Scale Invariant Feature Transform (SIFT) identifies common feature points across the different images, enough to establish the spatial relationships between the original image locations in an arbitrary 3-D coordinate system. A sparse bundle adjustment (Snavely et al., 2008), needed to transform measured image coordinates into 3-D points covering the area of interest, is used in this process. The result is represented by the three-dimensional locations of the feature points in the form of a sparse point cloud in the local 3-D coordinate system.

The SfM algorithm is included in several software, coded in different forms, typically taking advantage of up-to-date computer vision routines. The friendly and useful interface of Agisoft Photoscan Professional Edition (version 1.2.4 - 64 bit) has been chosen, due to its suitability to UAV images post-processing (Agisoft and Manual).
In particular, the workflow proposed by this software, which is sketched in the right part of schema in Figure 4.3, is suitable for DSM generation. At the first step the image loading and alignment is performed. Common points on different images, represented by particular features and edges are identified and matched. The camera position and the camera calibration parameters are hence, evaluated by the algorithm. The camera

parameters EXIF file contains the focal length (f_x, f_y), principal points coordinates (c_x, c_y), the skew, the radial and tangential components of distortion model, k_1, k_2, k_3 and p_1, p_2, respectively.

GCPs are uploaded into the model by writing/importing their coordinates. The user has to select manually the GCP on one image and then, it is recognized on every other image containing the same point. The manual correction of GCPs mismatched location (by the algorithm) on some images can be applied. The alignment optimization is performed in order to exclude sparse points with high reprojection error. Moreover, by choosing a bounding box one can exclude outliers.

After this step a dense point cloud is reconstructed, on pixel basis. The local point cloud is georeferenced in a world coordinate system, and a triangular mesh is built. The mosaic of images is created on the mesh for producing an orthomosaic (Agisoft and Manual). The DSM and orthomosaic are so exportable, with the selected coordinates system and spatial resolution.

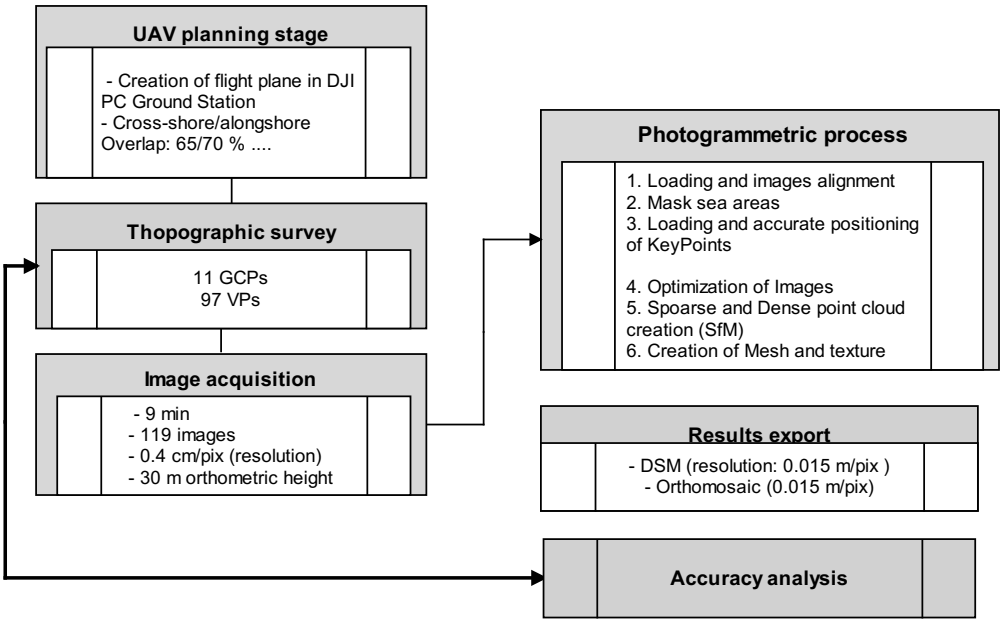

Figure 4.3 Workflow of methods used, starting with the UAV campaign preparation until the determination of orthomosaic and DSM accuracy assessment on the basis of GNSS data (VPs points)

4.4. Results

4.4.5. Image processing

The processing of 119 images is undertaken for this flight application. A pre-processing routine includes the gamma correction, contrast adjustment and the masking of the water surface areas. The highest “accuracy” value is chosen in the image alignment procedure. The GCPs are imported, correctly assigned on each image manually and the orientation process is optimized. Small changes of camera parameters, as highlighted in Long et al. (2016) after optimization is experienced. The accuracy for all points is set at $0.005\ m$.

The resulting residual errors computed on GCPs from the bundle adjustment procedure are shown in Table 4.1. Specifically, the transformation resulted in RMS errors of $0.017\ m$ in the East, $0.018\ m$ in the North and $0.011\ m$ in the vertical direction,

while the overall total error is computed as $0.0279\ m$. In pixel space, this results in an average $0.3\ pixel$ error, with only one outlier computed as $1.4\ pixel$.

Table 4.1 Resulting residuals errors of the bundle adjustment transformation computed on Ground Control Points (GCPs) where total error is in 3-D (m), X-Error refers to East, Y-Error to North and Z-Error to the Altitude direction, respectively.

GCP	East	North	Altitude	X-Error (m)	Y-Error (m)	Z-Error (m)	Tot. Error (m)
0	743668,508	4462849,897	0,930	-0.003266	-0.033531	0.006934	0.034396
1	743671,049	4462834,682	0,242	-0.004987	0.000025	0.001205	0.005130
2	743690,897	4462828,080	1,123	0.016409	0.013190	0.012176	0.024321
3	743692,641	4462814,729	0,570	-0.018792	-0.010577	0.001916	0.021649
4	743707,771	4462806,618	0,363	0.042052	0.025039	-0.009320	0.049822
5	743704,940	4462792,556	1,065	-0.004768	0.011833	0.015096	0.019765
6	743715,170	4462781,711	0,416	-0.027909	-0.023665	-0.017678	0.040638
7	743731,094	4462774,141	1,175	-0.001613	0.003385	-0.002291	0.004394
9	743762,418	4462724,031	0,213	0.003124	0.004535	0.006443	0.008476
10	743642,335	4462865,223	0,376	-0.000490	-0.017076	0.006752	0.018369
11	743624,733	4462908,133	4,430	0.001528	0.028357	-0.023561	0.036899
RMS				0.017170	0.018744	0.011585	0.027935

4.4.6. Digital Surface Model

As highlighted on the schema in Figure 4.3, a dense point cloud is produced, by using the “high” quality parameter and “aggressive” Depth filtering option in the software (Figure 4.4). This parameters combination determines an increasing in processing time, but as well, it helps supporting the reconstruction when a low number of keypoints is used, as for this application.

In order to investigate the absolute accuracy of 3D surface from the point cloud, the default linear interpolator in Photoscan is used to produce a DSM. The DSM generation would be difficult on such a coastal area, specifically while analysing white and smooth surface areas, hence the interpolation optimizes the results. The pixel spacing has been

chosen on the basis of software estimated resolution, which is $0.0152\ m$, derived from the averaged distance between points within denser areas.

The DSMs and the orthomosaics are analysed within a geographical information system (GIS) based on the ArcGIS® software 10.1. The Figure 4.5 shows the resulting DSM.

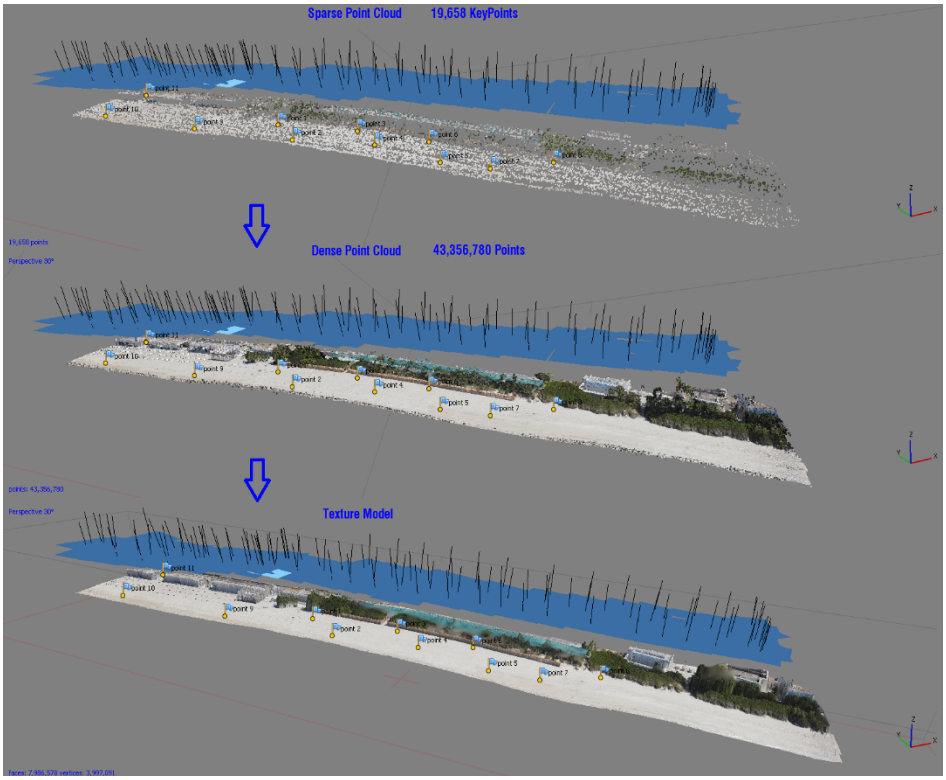

Figure 4.4 Latest stages of the photogrammetric process at the Torre Lapillo beach: **Top:** creation of sparse point cloud, **Middle:** dense points cloud, **Bottom:** model texture (the reference number on the left bottom of each of the 3-d sketch defines the KeyPoints and faces/vertices.

4.4.7. Vertical accuracy evaluation of DSM

To assess the vertical accuracy of the DSM UAV-derived, the arithmetic average error and the root mean square error (RMSE) are calculated on the basis of the difference between the orthometric height measured with d-RTK GNSS (on the VPs, distributed over the cross-shore transects) and extracted from DSM at those coordinates (Figure 4.2). This assessment is made possible thanks to the high spatial resolution of DSM.

The average difference, which is $0.033\ m$ is in good agreement with the absolute vertical accuracy of the GNSS points, equal to $0.013\ m$, an overall little overestimation can be fully justified. The RMSE is almost equal to the mean, indeed the related histogram highlights the narrow amplitude of variation, with only 1 significant outlier, which is at $0.12\ m$. The Figure 4.6, at the Top, shows the regression line, which underlines a very good agreement of measurements and a fit close to slope 1, between corresponding points. Relative R^2 of model fitting is high (0.995). The frequency histogram shows a quasi-Gaussian curve in the UAV-GNSS comparison.

The systematic positive error is most probably due to a combination of factors. First of all, the post-processed tuning of orthometric height, due to not rigorous acquisition procedure used for VPs topographic survey, described in Sec. 4.3.2. . Then, the linear interpolation used to reconstruct the DSM carries out artefacts in a high-corrugated sandy environment, and at least the techniques employed for both surveys are different, based on imagery and rod acquisitions. Nevertheless, the comparison results in high level of accuracy of DSM UAV-derived.

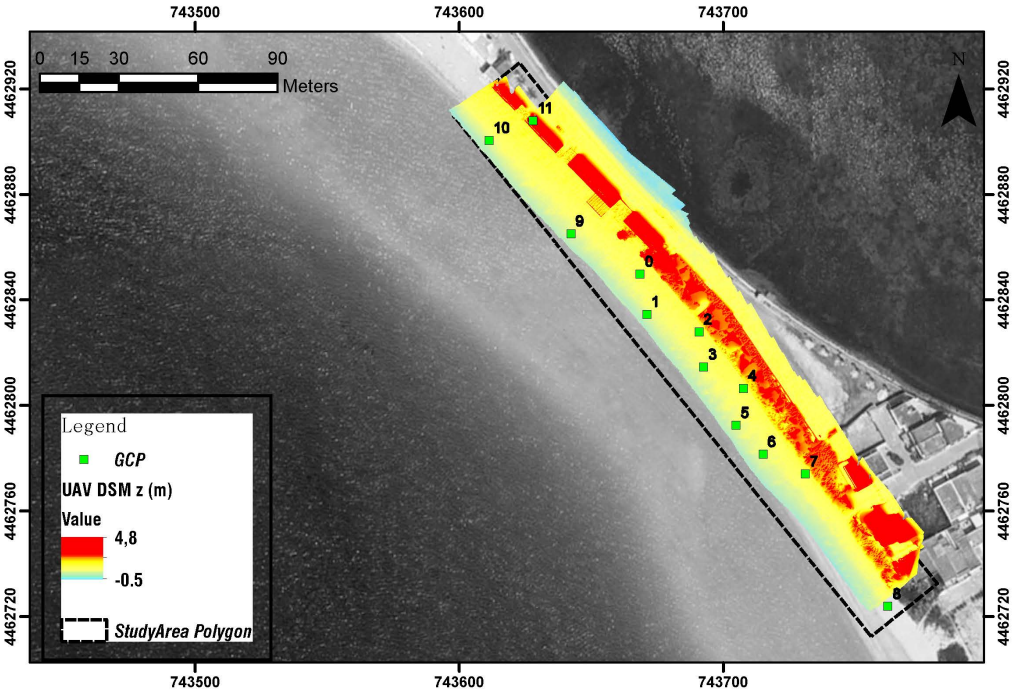

Figure 4.5 DSM obtained from UAV survey. Elevation above sea levels measured in m. Highlighted the GCPs location.

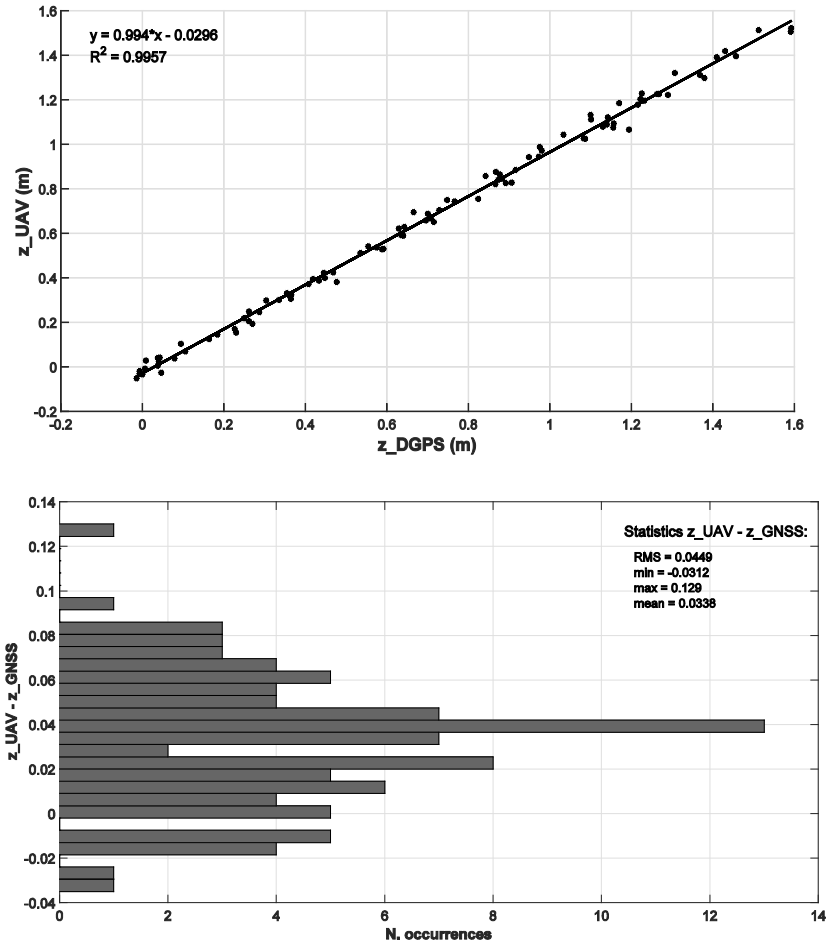

Figure 4.6 ***Top:*** *Comparison between the elevation of VPs GNSS data and corresponding points extracted from the UAV DSM. Linear fitting plotted and regression parameters highlighted.* ***Bottom:*** *Histogram of relative differences for classes of* $2\ cm$*. Legend displayed mean statistics of comparison.*

4.5. Discussion

The DSM reconstruction of a sandy beach is undertaken over a small area of the embayment beach at Torre Lapillo, in the South of Italy, by using UAV imagery and SfM algorithm.

A redundant number of images, a mean of 13 overlapping images is calculated for this study, enables the SfM matching algorithm to well perform (Fonstad et al., 2013). The GCPs location has been evenly distributed and the pattern and size used have demonstrated to be successful. Bundle adjustment residual errors are computed on 11 GCPs. Harwin and Lucieer (2012) suggest GCPs spacing of one fifth to one tenth the UAV flying height, while using focal length $> 10\ cm$. In this study, a focal length of $16\ cm$ is implemented, and moving from central to side area, a spacing of around 15 to $30\ m$ (the applied flight height) has been verified to be robust. Only GCP N. 8 (Table 4.1), which is outside the study area, is not considered. Flight height of $30\ m$ guarantees high definition results (orthophoto and DSM), and permits, coupled with 20.1 megapixel camera hardware, potential further detailed investigation on the site. The take-off and landing operations are manually performed and facilitated by the UAV box placed very close to the study area limit. An issue in the automatic acquisition shooting is found during survey and overcome with a manual mode intervention, which does not affect the results.

The vertical accuracy of the method presented in this chapter is shown to be around 4 cm, accurate in the order of magnitude of GNSS-based surveys (Lee et al., 2013), but much faster and providing much denser spatial information. These results are in line with previous and current coastal UAV application, always using the SfM method (Long et al., 2016, Mancini et al., 2013).

The coastal stretch investigated includes topographic complexity due to vegetation at the foreshore limits, that are protected by bamboo fence seaward, and other man-made improvised emerged barriers of sandbags. Further analysis would allow to access the importance of these complexities in order to an overall accuracy determination for such a complex foreshore system. As expected the swash area produces point cloud to be scattered and not well suited to be post-processed, hence this is masked.

4.6. Conclusion

This study demonstrates the potential of UAV imagery using a photogrammetric/computer vision approach, the SfM algorithm, in order to solve the topography in peculiar beach environment.

This study involves the survey of a small coastal stretch, of $10{,}000\ m^2$ around, by using a UAV multicoter. Such a non-intrusive method can be easily extended over larger geographical extension, still maintaining high dense spatial information, even if more surveys are needed, due to low battery lifetime. The Photoscan software is motivated in this study because it represents an attractive method since the software package has a linear, project-based workflow, which is intuitive and can be easily mastered.

The validation procedure illustrated in this chapter suggests that the method applied, employed to generate point cloud and high resolution DSM, orthophoto of the beach system, demonstrates a very good degree of agreement with GNSS ground truths. As suggested in Mancini et al. (2013), this solution represents a cost-effective alternative with respect to TLS survey in high resolution DSM reconstruction, as the latter instrument increases two or three time order of magnitude the total costs. While traditional topographic survey by GPS, with same expense, would result coarser.

The gamma correction and contrast adjustment are applied to the imagery, in order to facilitate the photogrammetric process. An algorithm to identify and automatically mask water areas would be useful, meanwhile this process is manually performed in this study.

CHAPTER 5

VIDEO ANALYSIS OF WAVE RUN-UP AND NUMERICAL PREDICTIONS WITH SWASH MODEL

Chapter 5 - VIDEO ANALYSIS OF WAVE RUN-UP AND NUMERICAL PREDICTIONS WITH SWASH MODEL

5.1. Introduction

Storms represent one of the most significant natural hazards always explored by coastal communities, leading to lives lost and properties damage. It is one of the main cause of extensive changes to coastal topography, including shoreline erosion, destruction of protective dunes, creation of large overwash deposits, damage/destruction to infrastructures and other unfavourable consequences. Such negative effects thus invoke the need for new tools concerned with coastal risk management and safety issues, aim at developing reliable predictive models, potential warning systems and vulnerability maps, in support of preventing often-irreversible conditions and flooding.

In such a perspective, the importance of understanding and quantifying the accuracy of run-up predictions under severe conditions is twofold. Firstly, an accurate prediction of sediment transport processes by both numerical models and statistical approaches are based on calibration analysis. It is important to know if these calibrations are correct for underlying prediction errors in hydrodynamic processes (Nielsen and Hanslow, 1991). Moreover, the predictions of severe water levels that include wave run-up are required for more accurate assessments of coastal hazards. As introduced, wave-induced water levels can be a direct threat to people, infrastructure, and ecosystems; however, they are often not routinely included in the analysis of coastal hazards by e.g. the weather forecasting community. Meanwhile, understanding the accuracy of run-up predictions during extreme wave events will help to inform and improve assessments of potential hazards to people, communities and structures (e.g. roads, houses, nests) in such a dynamic coastal environments that shift and change with each storm (Ruggiero et al., 2004).

Wave run-up processes are not easy to measure, particularly under extreme conditions. Powerful wave forces and significant beach change can damage observing equipment

or introduce uncertainty in the underlying topographic elevations needed to understand the run-up processes.

Two approaches useful to circumvent data collection challenges could be based on ground-remote observations potential and on numerically simulations of swash zone and run-up. Both approaches are implemented and described in this chapter by taking advantages of the new developed video monitoring system and by using SWASH model simulations, respectively.

SWASH is chosen since in literature it is revealed to be numerically more straightforward with respect to similar phase resolving model (i.e. Bousinnesq wave model MIKE21 BW), in terms of numerical robustness (De Roo et al., 2015), easiness in implementation and open source orientation.

Here, it is presented a merging strategy of a high detailed DSM UAV-derived with a Multi-beam bathymetric dataset, which provides topographical input for SWASH 2d numerical modelling, whose results are compared, at several cross-shore sections, with corresponding video run-up measurements.

Then, it is conducted a comparison and sensitivity study to assess the accuracy of SWASH run-up predictions in 1d mode, across a range of beach cross-shore transects, in correspondence of two significant storm events with relative video run-up measurements.

At the end, by means of state of the art empirical models, the run-up is evaluated during considered events. Suggestions on a workflow for developing reliable tools for coastal planning and management, by using the above mentioned strategy are discussed.

5.2. Measurement from video observations

The study area under analysis corresponds to a stretch of the embayment beach at Torre Lapillo, hamlet of Porto Cesareo, where a coastal video monitoring station, is installed (Chapter 3 -). The reader is referred to Subs. 3.7.2. for further details about the morphological environments and main wave regime characteristics.

Real Time Kinematic surveys using differential GPS solution on the Global Navigation Satellite System (GNSS) of Apulia Region were carried out on 1st March 2016 and 26th May 2016, supported by the AdBP personnel. The surveys allow to measure the cross-shore beach profile on $10\,m$ spaced 12 and 16 transects, in the area framed by the PC_{vs1} and PC_{vs2}, respectively, providing the alongshore variation of beach slopes until around $0.9 \div 1\,m$ depth. The horizontal coordinates refer to UTM Zone 33N (ETRF2000), while the vertical values are measured with respect to the mean sea level derived from the ITALGEO2005 model, provided by the Italian Geographic Military Institute (IGMI). They are representative of the gently curved centre of the embayment beach that is characterized by a typically asymmetrical planform shape. An exhaustive discussion on the acquisition instrumentations and methods is illustrated in Subs. 4.3.2.

5.2.1. Methodology

A great effort on the use of video-based techniques addressed to the acquisition of wave run-up has been made over the recent years in order to define an effective tool in coastal research (Holman and Stanley, 2007a, Salmon et al., 2007).

The leading edge of the uprush phase of the swash can be easily identified as clear feature and hence, easily extracted through semi-automated routines, with minimal human input. However, the downrush phase is less distinguishable, limiting delineation of its position under storm waves.

For this study, time-stack images for wave run-up measurements are generated in correspondence of two significant events, dated 1st March 2016 and 11st May 2016, recorded by cameras PC_{vs2} and PC_{vs1} (Section 3.7 for naming conventions), respectively. In the following, they are referred as Ev_1 and Ev_2.

The transformation from image to world coordinates, image geo-rectification, takes place after applying a lens distortion correction, and by applying the 3×4 perspective transformation matrix, defined as P, using homogeneous coordinates. The procedure followed is described in details in Section 3.4 (geo-rect). The real world coordinates of

the points along the desired beach transects, on cross-shore direction, are transformed into image space in order to define the line along the original image (undistorted). The pixel intensities are extracted along the line with python scripting and OpenCV libraries from each frames, during video progressions. Each recorded video has a duration of 30 min and the acquisition frequency used is $5\ Hz$. Final time-stack images, resampled at $2.5\ Hz$ are produced, with x-axis and y-axis indicating time and cross-shore distance, respectively.

The elevation and location of the cameras have a high impact on the cross-shore resolution of the pixel time-stack extracted. The cross-shore (horizontal) resolution is in the range $2 - 15\ cm$ around, for both cameras time-stacks images. These estimations are derived from the values of the minimum pixel footprints along each monitored transect. The topographic surveys described above, for the two events, take place on the same day and few days later with respect to the measurements, respectively.

Time-stack pre-processing has been crucial before implementing routines for swash extremes recognition, due also to the framed sand geo-textiles bags, algae, even flags of a nearest beach establishment, which make images dirty or altered and not feasible for subsequent processing. It is mainly based on a procedure that includes manual masking of the above mentioned pixel areas, and a macro comprising a special combination of background subtraction, BEEPS (see Chapter 3, iv)) and variance filters on the grey-coded channel image (Figure 5.1). In order to obtain optimal performance on the following real processing task, a manual sensitivity analysis on the filter parameters is approached.

Hence, for the real time-stack processing, in this work it is adopted an open-source GUI software (GUI_timestack, https://sourceforge.net/projects/guitimestack), which is based on MATLAB, useful to extract and process time series of cross-shore position of the swash extremes (Vousdoukas et al., 2012). It is based on modified Otsu's thresholding method and a manual control on the results is available through the GUI.

The GUI interface is divided into five panels and the options are briefly summarized in Table 5.1. The application requires unique structures that encompass primarily the following information:

- time-stack itself: image $n_x \times n_t$, where n_x expresses the number of grid points along the beach transect considered for time-stack generation and n_t the number of individual snapshots processed to generate the timestack image;
- x, z : cross-shore real-world coordinates and elevation of the beach transect considered for time-stack generation;
- $sdate$: time series of MATLAB serial date corresponding to the acquisition time of the individual snapshots processed to generate the timestack image;
- $date$ & $time$;
- H_s, T_p, Dir_p : spectral wave parameters (Vousdoukas et al., 2012).

Table 5.1 The graphical user interface time-stack processing application (from Vousdoukas et al. (2012))

Time-stack	Additional plot	General options	Swash tracking	Export options
Display time-stack and swash excursion with peaks.	Beach profile plot (the R_2,$R_{\max}$, η_{tide} levels) and wave run-up spectra plot.	Basic settings before the actual time-stack Is processed.	Manage the quality peak detection with limit in the time-stack area, manual control, etc.	The estimated data extraction options.

The obtained pixel values, expressing cross-shore coordinates of swash extremes, are transformed into elevations using the topographic information from the field surveys, assuming there are little morphological change between video acquisition and d-RTK GPS surveys.

The estimated elevations represents the total wave run-up $\eta_{tot}(t)$, which can be defined as:

$$\eta_{tot}(t) = \eta_{tide} + \eta_{su} + \eta_s + S_{sw}(t) \tag{5.1}$$

where η_{tide} and η_{su} are the tidal and surge heights, respectively; η_s is the maximum wave set-up height; and $S_{sw}(t)$ is the swash-induced water-level fluctuation (Stockdon et al., 2006, Vousdoukas et al., 2009). The run-up height R, usually defined as discrete variable, is derived from the peaks of water level fluctuations $\eta_{wl}(t)$ time-series with respect to still water level, described in Eq. (5.2):

$$\eta_{wl}(t) = \eta_s + S_{sw}(t) \tag{5.2}$$

Given the distance of the PC tidal gauge, the tidal and surge heights variation are assumed to be considered because directly measured. The run-up statistics are calculated for each 30-min video recordings, considering 2% exceedance values derived from the cumulative probability density function of run-up maxima elevations, and maxima value of time series.

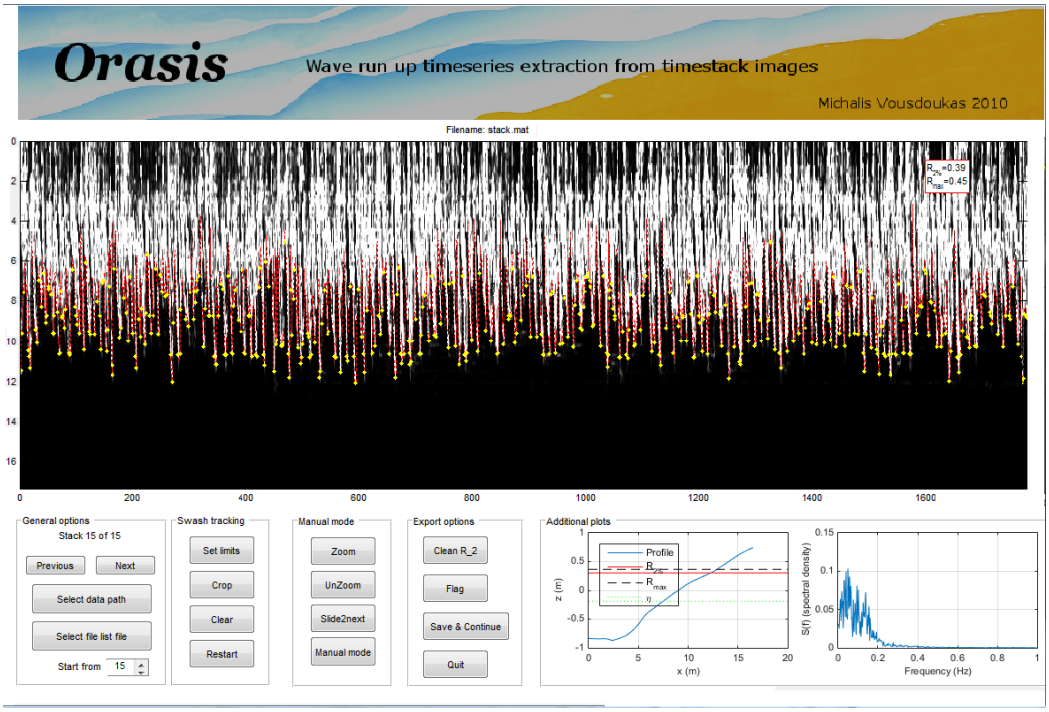

Figure 5.1 **Top:** Camera PC_{vs2} undistorted FoV and one corresponding oblique run-up time-stack (red dashed line, Transect N.7). **Bottom:** Screenshot of the GUI processing software used. The top panel shows time-stack with the y-axis that represents the cross-shore transect location of video-derived run-up observations and the x-axis the time variability. The leading edge of swash is plotted through time (red line) and converted into a time series of water-level elevations, yellow dots are the swash extremes recognized by software routine. The bottom panels are well summarized in Table 5.1.

5.3. *Numerical approach*

The numerical approach employed in this context is to use the output of model Mete-Ocean (WaveWatchIII), combined with SWAN and SWASH runs (see Section 1.2), to describe waves approaching the nearshore, including the surfing zone. To simulate waves from the offshore zone until shore, numerical simulations with nesting schemes have been run. The proposed strategy is to use the MeteOcean forecast database for nesting into the SWAN model rather than feeding it directly into the SWASH model. The great accuracy of MeteOcean model is briefly discussed in Subs. 1.2.3. Furthermore,

it is extensively known and assessed the capability of SWAN to produce very accurate shallow water spectral wave conditions, ideal for SWASH implementation (Guimarães et al., 2015). Hence, a good representation of the wave processes on meso and fine scales are achieved. In the Chapter 4 - the capabilities of UAV imagery in solving beach topography with photogrammetric and computer vision techniques is evaluated and discussed. Results show very high level of precision, as derived from a non-standard photogrammetric technique and especially suitable for being used in coastal process simulations.

5.3.1. Spectral model set up

SWAN is the third-generation wave model that computes random, short-crested wind-generated waves in coastal regions and inland waters to solve the spectral action balance equation, treated in discrete form (Booij et al., 1996), see Subs. 1.2.4.

The models set-up, in both approaches, mono and two-dimensional presented hereafter include spectral waves modelling, by using two nested SWAN grids.
In the present study, the SWAN simulations are performed in a two-dimensional, non-stationary mode, over regular grids, on two nested domains (Figure 5.2). The coarser offshore grid ($16.2\ km$ long and $17.4\ km$ wide) starts at a depth of around $90\ m$, equally discretized in both x-y directions, with a resolution of $150\ m$. From around 35 m deep water until the shoreline, waves transformations are analysed on a nested regular finer grid, with a spatial discretization equal to $80\ m$ (Table 5.2). The nearest coastal grid is 4.5 km long and 5.1 km wide (Figure 5.2).
The table 5.2 shows, following the SWAN standard convention, main features of SWAN grids (DIR_x refers to direction of the positive x-axis of computational grid, Cartesian conventions).
A time step of $30\ min$ is used in simulations, with the wave boundary conditions data included every $1\ hr$. The tidal data are corrected as well, by using measured water level by nearest Porto Cesareo tidal station. The spectral space is computed at 24

Table 5.2 Computational SWAN grid features

GRID	RESOLUTION	ORIGIN		DIR_x	m_x*m_y
		x_c	y_c		
$G1_{150}$	$150\ m$	*728722.8*	*4451961.1*	*338°*	*115 *107*
$G2_{80}$	$80\ m$	*739010.1*	*4460207.1*	*338°*	*63* 56*

equally spaced propagation directions in the circle ($\Delta\theta = 15°$) and 28 logarithmically spaced frequencies between $0.04\ Hz$ and $0.5\ Hz$.

The default parameters in the physical configuration are used (breaking constant, Jonswap formulation of friction, Setup, Diffraction and Triad interactions included, the quadruplet interactions parameter is set off). Wind forcing is not considered due to the near small geographic size of the computational domain.

The bottom conditions implemented in SWAN computational grids derive from IGM digitized nautical charts, merged in the nearshore zone with a more detailed dataset. The former is used to the littoral area of Ionian sea until $100\ m$ isobath. The latter is derived from a survey conducted by the management consortium of Porto Cesareo "Area Marina Protetta" by using MultiBeam EchoSounder R2 Sonic 2022 and hydrographic software QINSy and it covers the relative Marine Protected area (AMP, 2014). By using ArcGis Spatial Analyst tool, the Robust Kriging interpolation method is implemented, which represents an optimal and advanced geostatistical procedure that generates an estimated surface from a scattered set of points with z-coordinate (contour points). The output raster is built with a resolution of $20\ m$ (Kr_{20}). The coastline has been accurately adjusted, in the area spanned by both grids, before the interpolation procedure, on the basis of satellite derived data from Google Earth, dated 2015.

To input the wave boundary conditions, the results of the third generation wind wave model WaveWatchIII, as wave forecast database, is used. The model is maintained by MeteOcean group at DICCA department of Genoa. The model publishes $120\ hr$ forecasts, which includes the Ionian sea computations. The boundaries points locations are chosen and highlighted in Figure 5.2 (layer $Bound_{MO}$). Specifically, the two points closest to the coastline, $N.1,9$, placed on the WNW and ESE boundaries, are not

used because of null values computed. The MeteOcean model output dataset, sampled at $1\ hr$, includes the wind speed and direction, the main bulk spectral parameters, specifically significant wave height (H_s), peak period (T_p) and mean direction of wave propagation at the peak period (Dir_p). The nesting strategy is applied in SWAN, it is a well known in hydrodynamics simulation community, not discussed here. The total computational time is defined in the interval time of $20\ hr$ around the observations available.

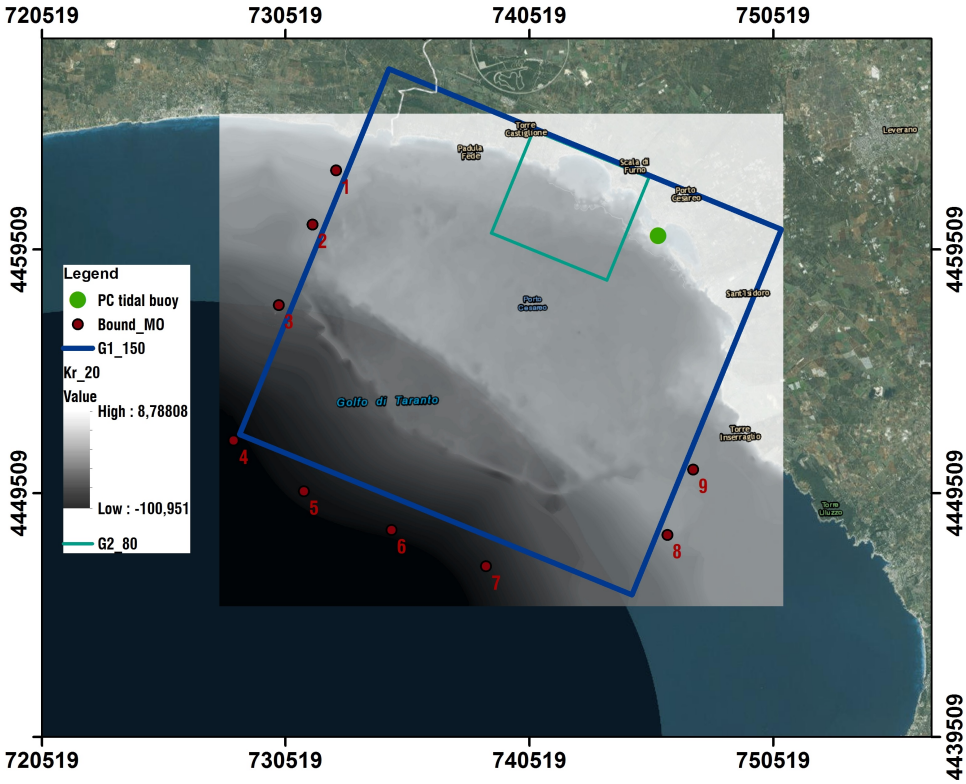

Figure 5.2 Study field representation. Blue line is the grid boundary of SWAN Grid $G1_{150}$, while light green line is of $G2_{80}$ grid. The bathymetry used interpolated on SWAN grid for simulations (Kr_{20}) is overlapped over gray-coded google earth basemap. The green points is the location of tidal buoy of Porto Cesareo (PC). The MeteOcean boundaries locations (red spots) are also displayed: 2 of them are not used because of “0” value.

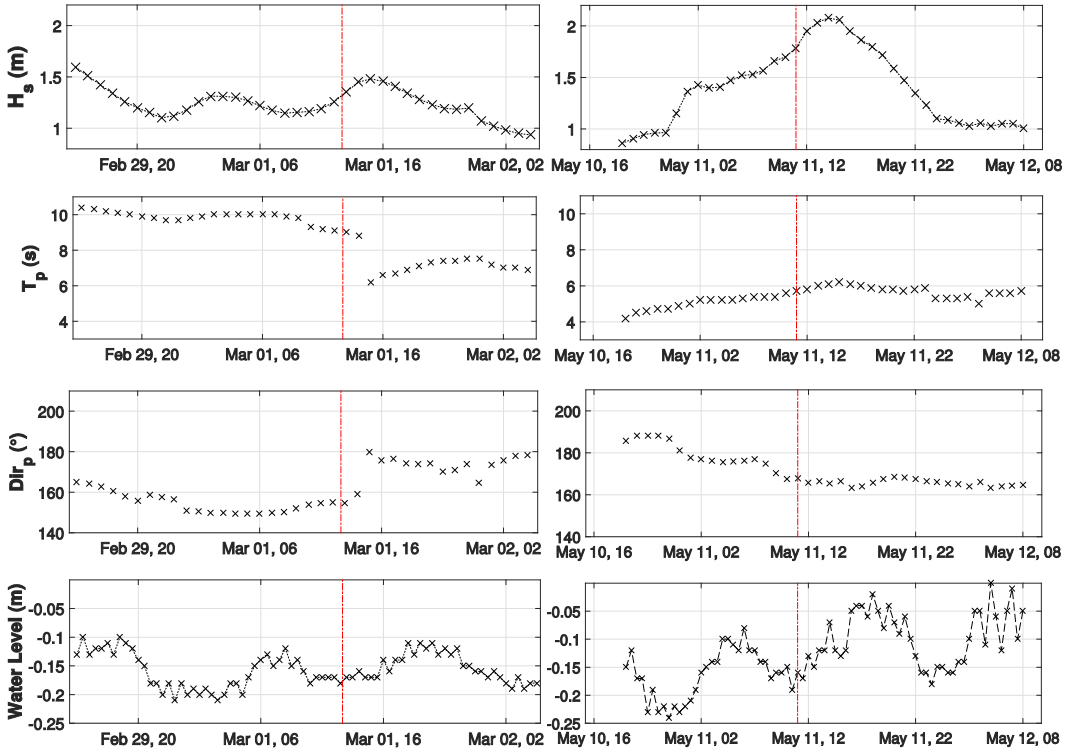

Figure 5.3 Boundary bulk spectral parameters from MeteOcean model, computed at point 6 (in the map counting counterclockwise from North in *Figure 5.2*), and sea level measured by tide gauge at nearest PC tidal gauge. **From Top to Bottom:** Significant wave height, peak period, peak direction, sea level. Vertical dotted red lines indicate times of run-up measurements.

5.3.2. SWASH 2-d model set-up

The SWASH model (an acronym of SimulatingWAves till SHore) introduced in Zijlema et al., (2011) is a non-hydrostatic model governed by the nonlinear shallow water equations, further details are discussed in Subs. 1.2.5. In this study, the 2-dimensional depth-averaged simulation of the event Ev_2 with SWASH is performed in a stationary mode over a curvilinear grid (205 x 1346) on the domain defined by the vertices $(743030.9\ E, 4462451.6\ N)$, $(743158.4\ E, 4462293.6\ N)$, and $(743614.7\ E, 4462922.9\ N)$, $(743742.2\ E, 4462765.0\ N)$.

SWASH is run including non-hydrostatic pressure, since it plays an important role in wave propagation processes (Suzuki et al., 2011). The domain spans $203\ m$ in the

alongshore and $750\ m$ in the cross-shore. The computational grid has a higher resolution close to the shoreline. Specifically, the alongshore resolution is fixed at $1\ m$, while the cross-shore one is set in the range $1 \div 0.13\ m$.

On Figure 5.6 the SWASH grid boundaries can be seen in geographic projected space.

The bottom condition implemented here is generated by merging the above mentioned MultiBeam dataset, with the cross-shore transects (survey dated 26/05/2016, above described), which are smoothed with natural neighbours interpolation, used for solving first seabed area more in details (until around $1\ m$ depth), and the high detailed DSM UAV-derived. It is built a raster with a resolution of $0.1\ m$ (Kr_{01}). The merge is done by using Data Management Tools - Mosaic To New Raster of ArcGIS® Desktop.

The simulation length is assigned to 35 min and time step is set to 0.004 s, which is automatically doubled at the beginning of simulation to 0.008 s. The results are recorded every $0.4\ s$ ($2.5\ Hz$) and the first $5\ min$ are considered as a spin up time. The default minimum and maximum Courant numbers are kept as 0.4 and 0.8, respectively.

The mean water level condition during simulation is imposed by considering the water level at Porto Cesareo measured by a tide gauge maintained by AdBP. Wave spectral conditions are set at each open boundary of the computational grid domain. The conditions are taken from the time dependent energy peak of the SWAN spectral results described above. While SWAN runs are performed in non-stationary mode, the irregular waves in SWASH simulation are treated as stationary. By using the linear wave theory, the velocity at a depth (Eq. (5.3) is found in SWASH by linear superposition of N harmonic waves, whose amplitude are determined by sampling a variance density spectrum and whose phase are randomly chosen for each realisation:

$$u_b(z,t) = \sum_{j=1}^{N} a_j \left[\omega_j \frac{\cosh k_j(z+d)}{\sinh k_j d} + \sqrt{\frac{g}{h}}\right] \cos(\omega_j t - \alpha_j) - \sqrt{\frac{g}{h}}\zeta \qquad (5.3)$$

where k_j and α_j are the wave number and the random phase, respectively, ω_j is the frequency. Given a wave spectrum $E(\omega)$, the amplitude of each harmonic is calculated as $a_j = \sqrt{2E(\omega_j)\Delta\omega}$, where $\Delta\omega$ is the frequency interval ($\omega_j = j\Delta\omega$).

The standard first order upwind scheme is kept for discretization of momentum equations. The Manning formulation is used for bottom friction with its default value ($cf = 0.019$). Sediment transport is not included in the simulations.

In the case of inundation or run-up, the SWASH model considers a moving shoreline. To solve the computational grid depth, hence to calculate the flooded area over the topography, the above mentioned detailed bathymetric dataset (Kr_{01}) supplies for the bottom condition (Figure 5.6).

In the SWASH output options, the horizontal maximum run-up is defined as H_{run}, as a vector with entries 0 and 1, representing a binary variable of land or water points, respectively, outputted at the end of computation. Thus, for a horizontal run-up it is possible to identify the maximum run-up by $\nabla H_{run} \neq 0$ as a horizontal grid index. This quantity, combined with the corresponding grid index of the bottom level output variable (*Botlev*) allows the determination of the vertical maximum run-up. While in order to perform a time series analysis, the SWASH output variables *Depth* or *Watlev* could be used, equivalently. Specifically, the wet front (wet/dry interface) is tracked by storing the last landward grid index equal to 1 at each time step. The corresponding index of bottom level is used for defining the run-up vertical excursion time-series. Hence, the value of $R_{2\%}$ is statistically obtained by considering the exceedance curve of the peaks of run-up elevations time series at each transect.

Figure 5.4 shows an example, as plan view, of the spatial variability of SWASH water-level (*Watlev*) output at one time step and the cross-shore temporal variation of water levels at a single longshore location.

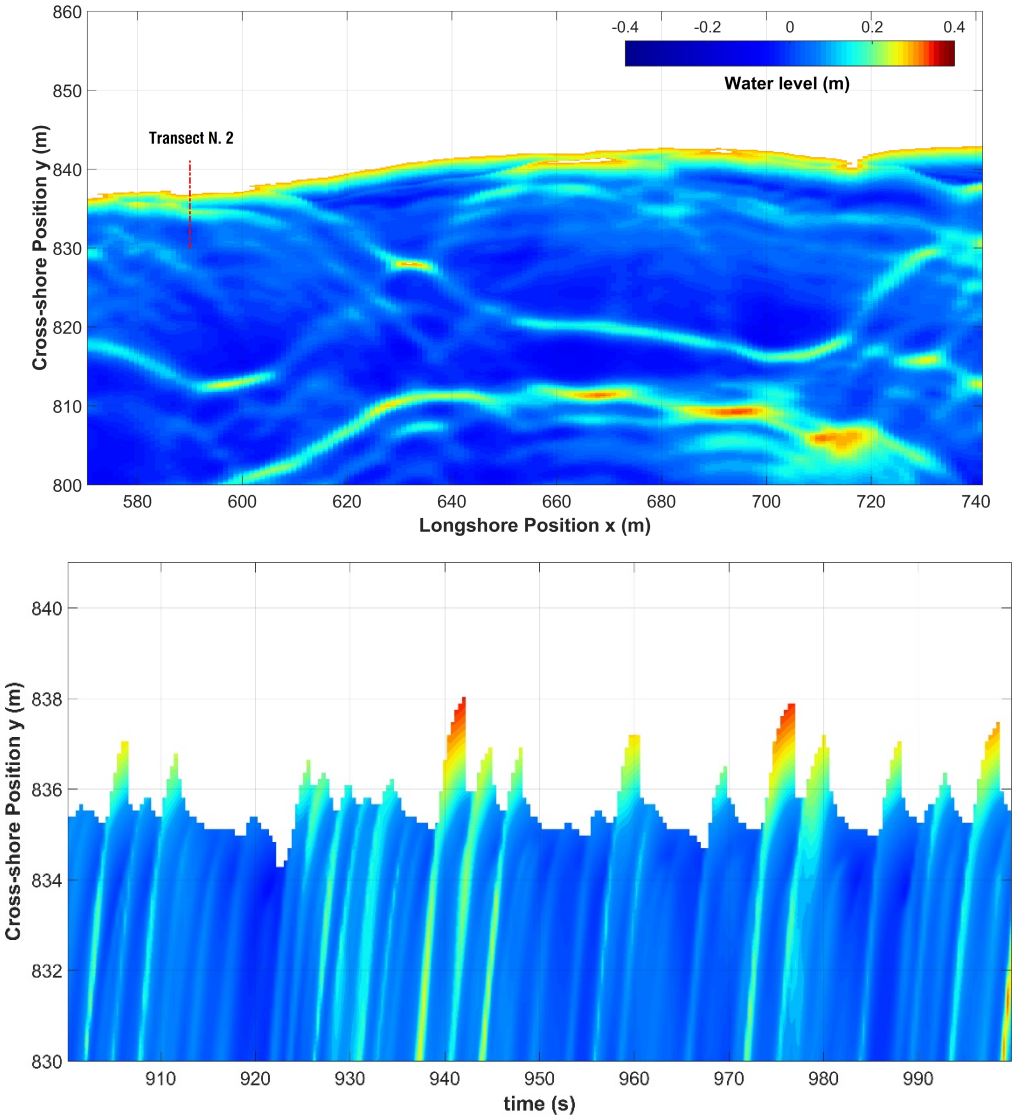

Figure 5.4 **Top:** Plan view showing the spatial variability of SWASH water level computed at 06:00 min time step (Ev_2). **Bottom:** Time variation (time-stack) of SWASH water levels at i.e. one longshore location ($x = 590\ m$ on dashed red line on Top panel). Origin of local Coordinate system: $[x, y] = [7.435838e + 05, 4.4624715e + 06]$

5.3.3. Results

The output quantities of SWASH model are defined overall the computational grid and specifically on 16 chosen transects, built by extending seaward the topographic surveys dated 26th May 2016, where corresponding time-stack measurements are also performed (horizontal grid step$=0.13\ m$). The SWASH computation for Torre Lapillo beach resulted in 35 min of non-hydrostatic simulation of the offshore hydrodynamic conditions during stationary wave event described in Figure 5.3 on the right.

A simulation of a 35 min length takes approximately 2 days on 8 cores of a Windows Desktop with an Intel Core i7 5390k, up to 3.2 GHz processor without using mpich2 for parallel MPI implementation.

In Figure 5.5 the comparison between the 2% exceedance and maximum wave run-up calculated by the SWASH model ($R_{2,sw2d}$, $R_{max,sw2d}$) and derived from the video measurements ($R_{2,ts}$, $R_{max,ts}$) is reported for the transects where valid numerical and video-measurements outputs are considered.

In the comparison of measurement data to model results, two statistical measures are used for define the accuracy of the model results: i) the root mean square error and the ii) bias, Eq. (5.5), respectively defined as follows:

$$RMSE\ (x) = \sqrt{\left(\frac{1}{N}\sum_{i=1}^{n}\left(x_{i,modelled} - x_{i,measured}\right)^2\right)}$$

$$bias(x) = \frac{1}{N}\sum_{i=1}^{n}\left(x_{i,modelled} - x_{i,measured}\right) \tag{5.4}$$

The maximum difference between the two methodologies for these mostly practical variables $R_{2\%}$ (R_{max}) is $0.182\ (0.24)\ m$ and the minimum is $-0.0048\ (0.04)\ m$ along the transects selected, where valid numerical and video-measurements output are present. In general, the $R_{2\%}$ is better predicted rather than the R_{max}, with a $RMSE \cong 0.08\ m$ and, except for transect N. 3, the numeric shows a small tendency of underestimating, as confirmed by the negative value of $bias$ $(-0.06\ m)$. Greater

differences can be observed for R_{max} with a equal to $0.15\ m$, overall the selected transects. Differently from the $R_{2\%}$, for which the differences between measured and predicted values are quite the same, the R_{max} is particularly underestimated for middle transects (e.g. n. 6, 9 and 12), while smaller differences can be observed for the other transects. Such a general trend should be also motivated by the vertical accuracy of the DSM UAV-derived, where an almost systematic error of around $0.033\ m$ is highlighted.

Unfortunately until now only very few data and corresponding DSM field measures at this region are available which makes impossible to systematically evaluate the precise performance of implemented model, especially during most severe storm events.

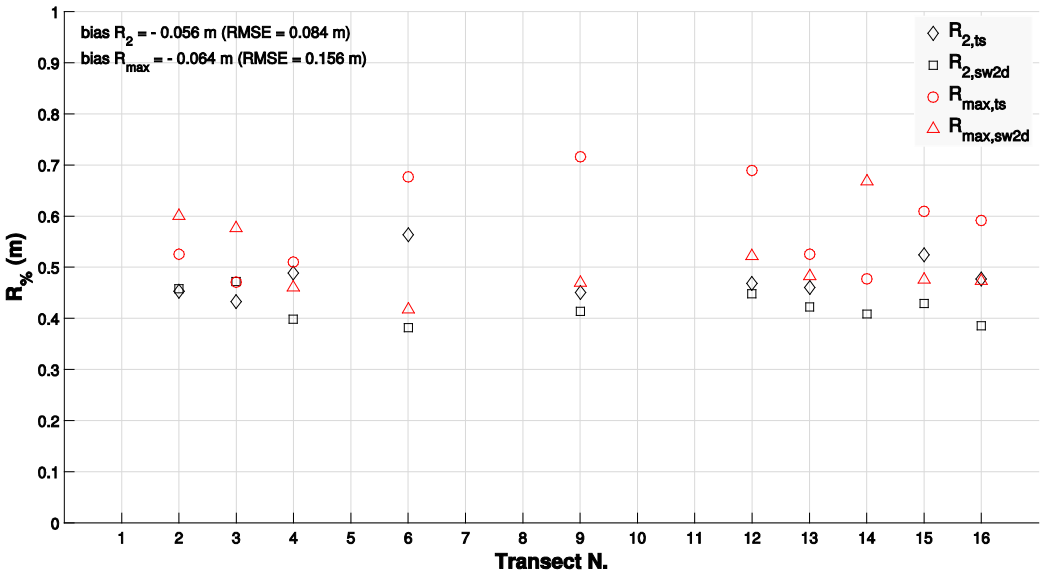

Figure 5.5 Comparison between predicted and measured R_2 and R_{max} over 16 transects, in the area framed by camera PC_{vs1}. Main difference and RMSE are highlighted.

5.4. Comparison between 1-d and 2-d SWASH simulations

The capability of the numerical model SWASH to be implemented in one-dimensional mode is tested and described hereafter, for both events described above.

5.4.4. Model Set-up

The SWASH simulations are performed in 1-d domains along the cross-shore transects introduced above where topographical measurements are present, so assuming alongshore uniformity. The sensitivity of wave run-up to the choice of domain dimensional space is evaluated and discussed.

Specifically, the cross-shore grids deployed for the transects in the area framed by cam PC_{vs1} have mean length of $700\ m$, a grid step of $0.13\ m$, in the cross-shore direction. While in the area framed by PC_{vs2}, since they are closer to the camera, a step of $0.05\ m$ is used, with same mean length of around $700\ m$. In Figure 5.6, the implemented SWASH grids can be seen in geographical projected space.

The simulation length for each transects test case is assigned to 35 min and time step is set to 0.006 s, which is automatically doubled at the beginning of simulation and set to 0.014 s. The outputs, after a spin-up time of $5\ min$, are requested every $0.4\ s$, consistent with the time-stack evaluation. The default minimum and maximum Courant numbers are kept as 0.4 and 0.8, respectively, as in 2-d case.

The mean water level condition during each simulation is imposed by considering the water level at Porto Cesareo measured by the tide gauge maintained by AdBP. Wave spectral conditions are set at the open boundary points of the computational grid domains. The conditions are taken from the time dependent energy peak of the SWAN spectral results described above, as non-directional wave spectrum. As described for bi-dimensional simulation, the irregular waves in SWASH simulations are treated as stationary. The standard first order upwind scheme is kept for discretization of momentum equations.

In order to solve the computational grid depth, hence to calculate the flooded area over the topography, the above mentioned detailed bathymetric dataset and RTK-GPS surveys are opportunely merged to supply for the bottom condition (Kr_{20}). With respect to 2-d mode cases of SWASH, the simulations of the mono-dimensional events are less computationally demanding (around half an hour each simulation).

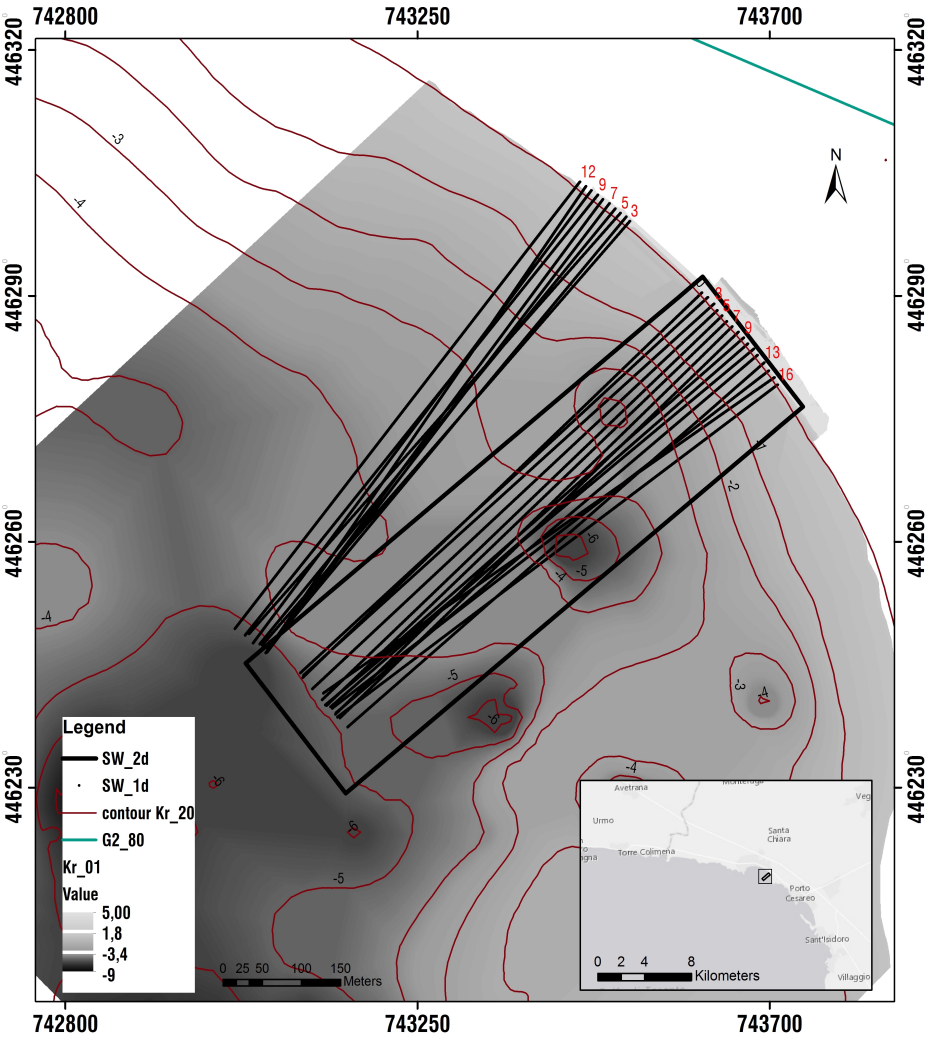

Figure 5.6 Study area of the SWASH simulations, 2d model boundary and 1d model grids highlighted. The contours of the bathymetry Kr_{20} and the raster of Kr_{01} are represented.

5.4.5. Results

Estimates of significant swash, in term of run-up prediction differ between the 1-d and 2-d SWASH implementations. Since the alongshore components of bathymetry, the wave groups, and swash are not fully resolved, 2-d swash levels lower than 1-d ones are expected (Stockdon et al., 2014). In Figure 5.8 the comparison between 1-d and 2-

d model predictions of run-up is reported. For all transects the difference between 1-d and 2-d simulations is rather the same. In general, the mean difference is almost equal to $0.22\ m$ for $R_{2\%}$ and of $0.28\ m$ for R_{max}, with a maximum difference of R_2 ($R_{\max}$) equal to $0.28\ (0.39)\ m$ for transect N.2 (9), while the minimum is 0.17 m (0.07), calculated at transect N. 3 (14). The overall trend is common for all transects investigated for the event Ev_2.

Before discussing, it must be pointed out the imposition of the same radiation boundary condition within the investigated area to simulate entering waves without some reflections. These differences in run-up for the two dimensional space could be reasoned for several physical/numerical factors. In order to retrieve reasonable causes for this behaviour some concepts could be highlighted. Firstly, it is verified there are no substantial differences in the wave height modelling within the surf zone between the two implementations, $H_{s,\mathrm{sw}2d} - H_{s,\mathrm{sw}1d} \cong +0.06\ m$, even if 2-d signal shows higher oscillations, which increase approaching the breaking zone . In the swash zone greater attenuation is highlighted for the 2-d, with respect to 1-d model (Figure 5.7). The one-sided spectral density of water levels outputs at a boundary, breaking and swash representative sections are reported in Figure 5.7. Spectra show the typical increasing of the bandwidth parameter across the swash zone, due to the interaction with the seabed, with a consequent transmission of the wave energy to higher frequencies, more relevant in the 2-d domain, thus leading to an overestimation of 1-d derived run-up. For this reason, moreover, a preliminary analysis by using cross spectral analysis via magnitude-square coherence of run-up and surf zone water levels has been conducted. A standing-wave component in the infragravity frequencies is observed in 1-d runs with respect to the 2-d domain. This behaviour, associated to the highlighted different simulated contributes of alongshore dissipation mechanisms of swash, via non-linear and frictional processes has most probably led to such results.

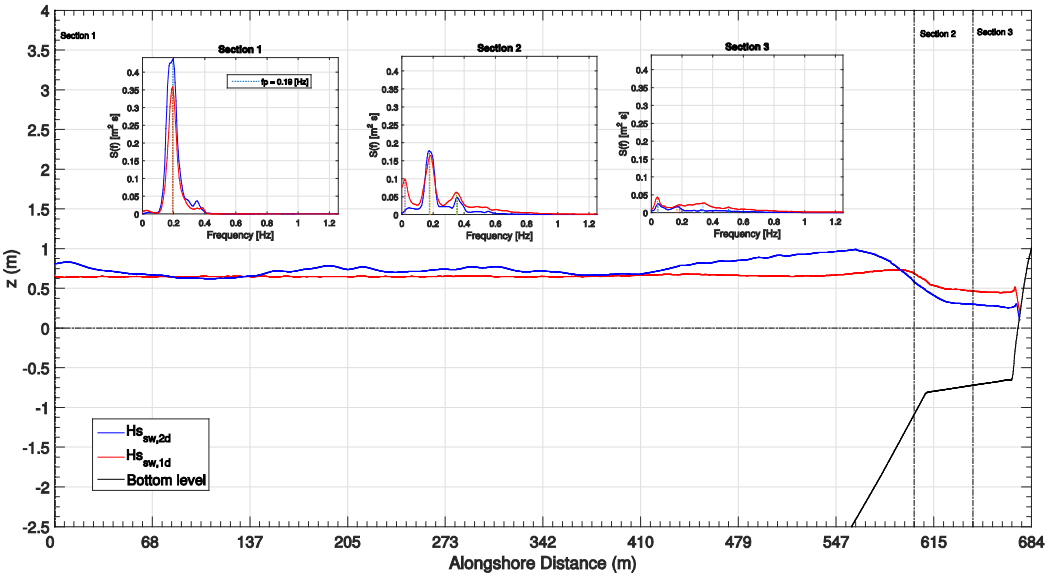

Figure 5.7 Alongshore variability of H_s between SWASH 1-d and 2-d and e.g. spectral transformation of water levels output comparison for the two spatial domains, at three representative sections. (Transect n.9)

Additional investigations, which are outside the scope of this chapter, may be required for a detailed understanding of the swash differences between the two spatial domains implementations.

By comparing both 1-d and 2-d numerical models with the run up measurements derived from video analysis, results show that the 1-d model systematically over predicts the time-stack results. A significant influence of the bottom friction in wave run-up prediction and wave overtopping, for NLSW equation models is well-known (Suzuki et al., 2011, Tuan and Oumeraci, 2010).

Different formulations are implemented in SWASH for the dimensionless friction coefficient calculation c_f. In the present study, the one based on Manning's roughness coefficient n, is used, as follows Eq. (5.5):

$$c_f = \frac{n^2 g}{h^{1/3}} \tag{5.5}$$

The default configuration setting for this parameter in SWASH is set equal to $\mathrm{n} = 0.019\ s/m^{1/3}$. There are still not univocal results and suggestions available in literature about its optimal variability. It is commonly accepted that, among several parameters, n mainly varies with grain diameter (Reis and Gama, 2010). For instance, previous experiences (Suzuki et al., 2011) suggest that smooth materials behaviour in laboratory condition could be well represented by using a value around 0.01 $s/m^{1/3}$, even the physical meaning of this value is associated to material such as glass. While a Manning's coefficient equal to about 0.02 $s/m^{1/3}$ is suggested for sandy materials with a diameter close to 1 mm, as such the present field case.

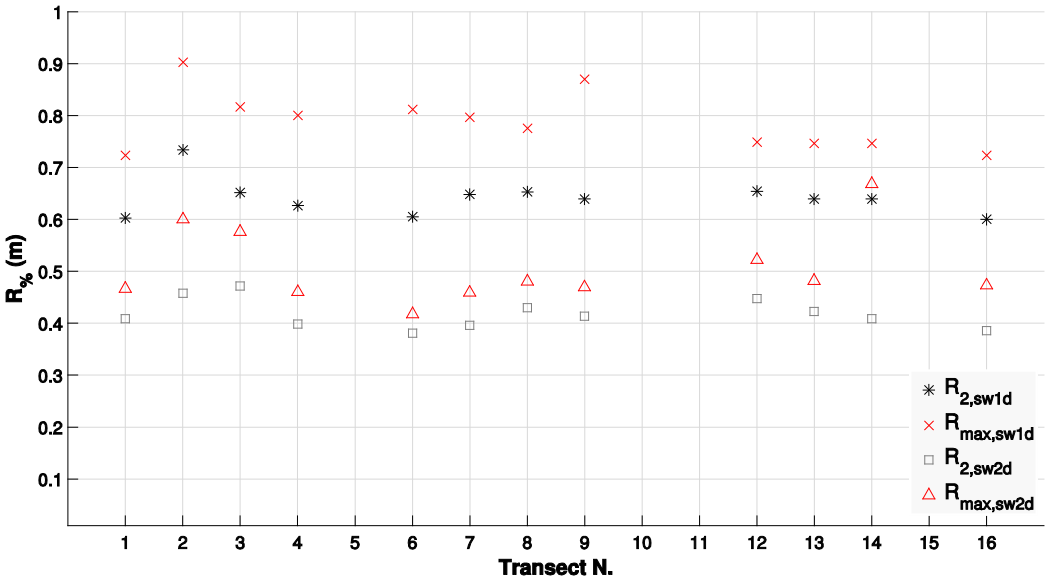

Figure 5.8 Difference in run-up prediction between the two spatial domain invetigated, for event Ev_2.

Due to such a range of variability of the Manning's coefficient and the difficulties in measuring it, it could represent a useful and straightforward setting parameter for numerical model calibration. In the present study, a sensitivity analysis of the SWASH model capability in predicting hydrodynamics, by varying the Manning's roughness factor, ranging from 0.01 to $0.04\ s/m^{1/3}$, according to the most typical field relevant values, is reported.

The Figure 5.9 shows an example of the significant wave height derived from the zero-order moment of the spectrum (H_{m0}) and wave set-up variation over the depth for transect n. 6, at different bottom friction values. As expected, far from nearly first breaking section, where maximum significant wave height and the minimum set-up (set-down) occur, both the significant wave height and set-up are not so sensitive to bottom friction. Such a behaviour is observed for all transects. On the contrary, around the above-mentioned mean breaking line and approaching swash zone, they become more sensitive to n. The peak period has been also investigated, and non-remarkable differences are highlighted.

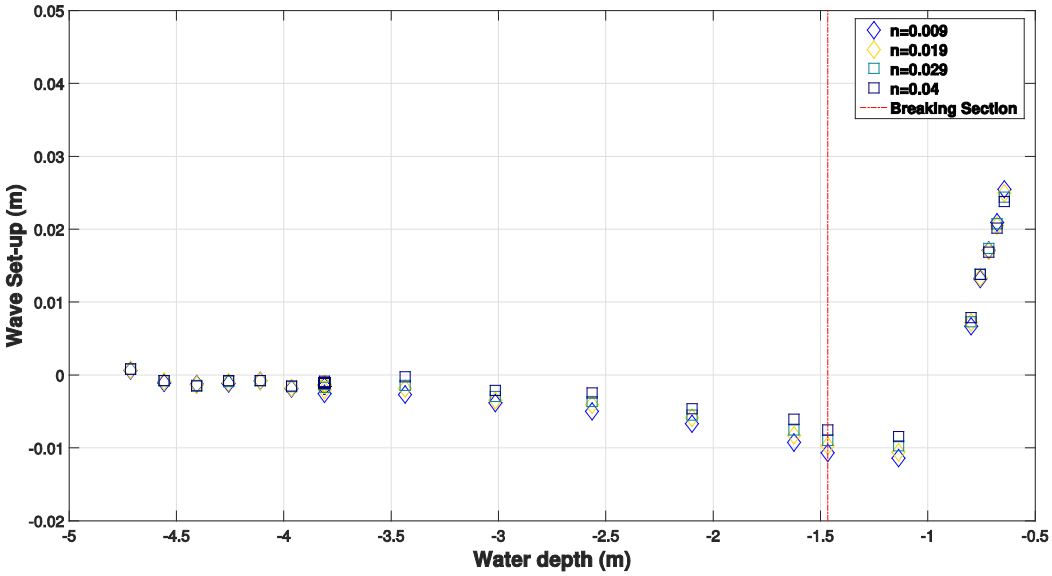

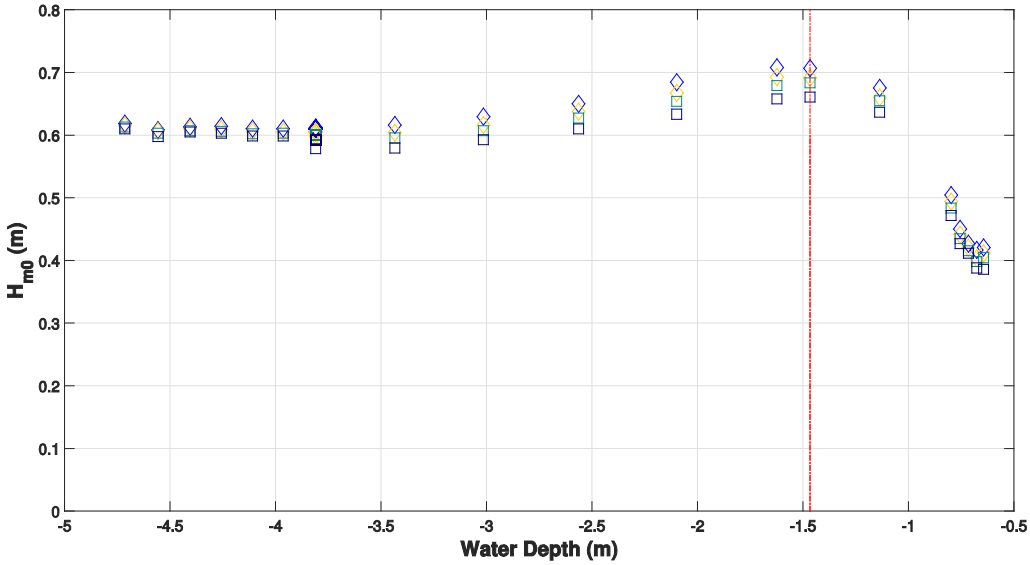

Figure 5.9 Sensitivity of wave set-up (**Top**) and significant wave height H_{m0} (**Bottom**) for varying Manning coefficient of bottom friction, respectively.

Figure 5.10 and 5.11 show the sensitivity of the bottom friction coefficient to the R_2 and R_{max} simulated by SWASH model. In this case, for each value of n investigated, the mean difference and RMSE between predicted and measured values over all transects studied are plotted. These figures indicate that the bottom friction has a significant influence on wave run-up, and the value of $\mathrm{n} = 0.04\ s/m^{1/3}$ reveals the best fit in predicting the time-stack measurements. With respect to R_2 calculation the RMSE≅0.06, $bias \cong 0.025\ m$, while for R_{max}, $RMSE \cong 0.075$, and $bias \cong 0.01\ m$. With respect to the 2-d simulation, where the model achieves optimal performance in run-up prediction with the default friction coefficient, $\mathrm{n} = 0.019\ s/m^{1/3}$, the 1-d results are satisfying only with an ad-hoc calibration of this parameter.

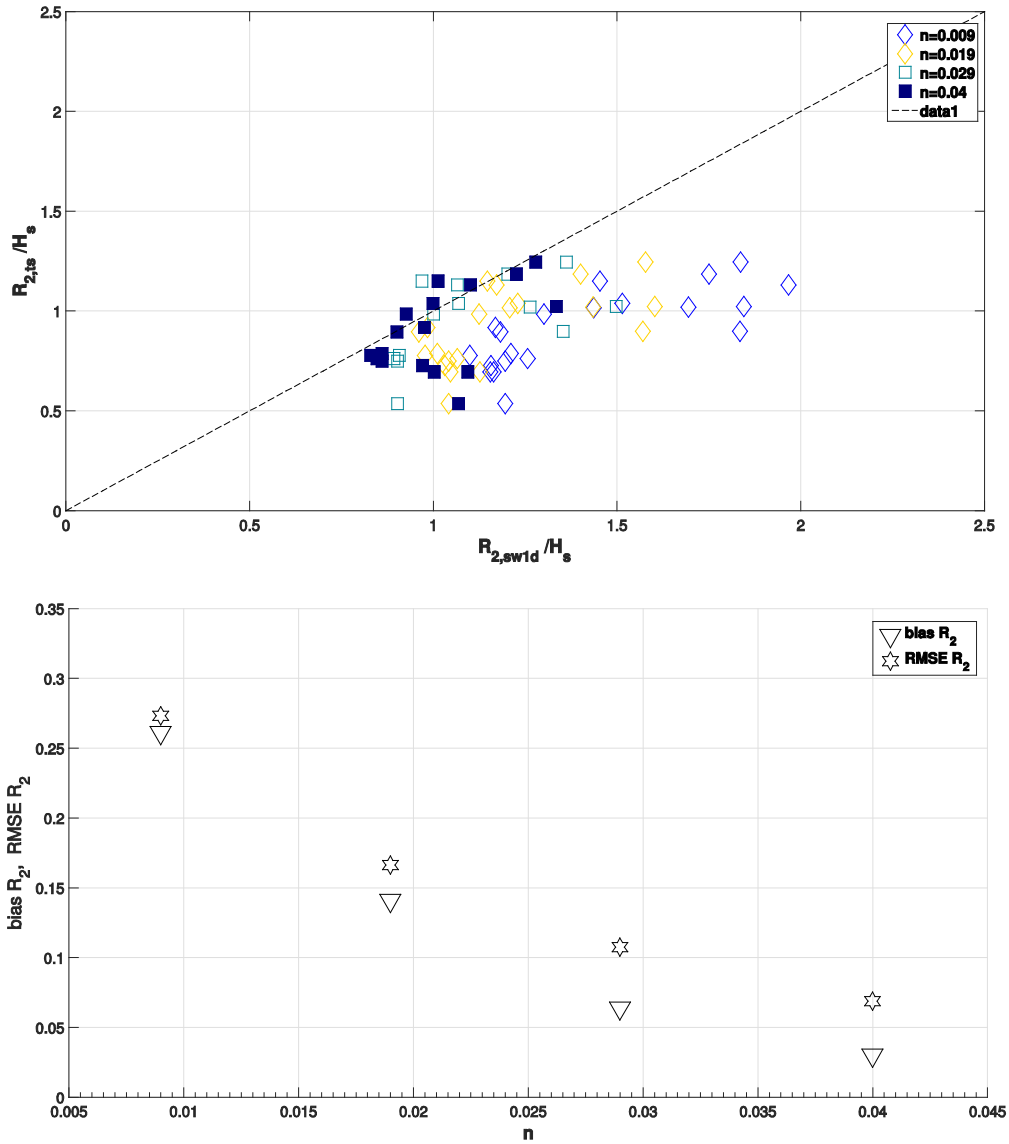

Figure 5.10 **Top:** Predicted R_2 plotted against the measured one for all transects analysed, both quantities are normalized for the significant height at relative boundary. **Bottom:** Sensitivity of bottom friction with respect to computed R_2.

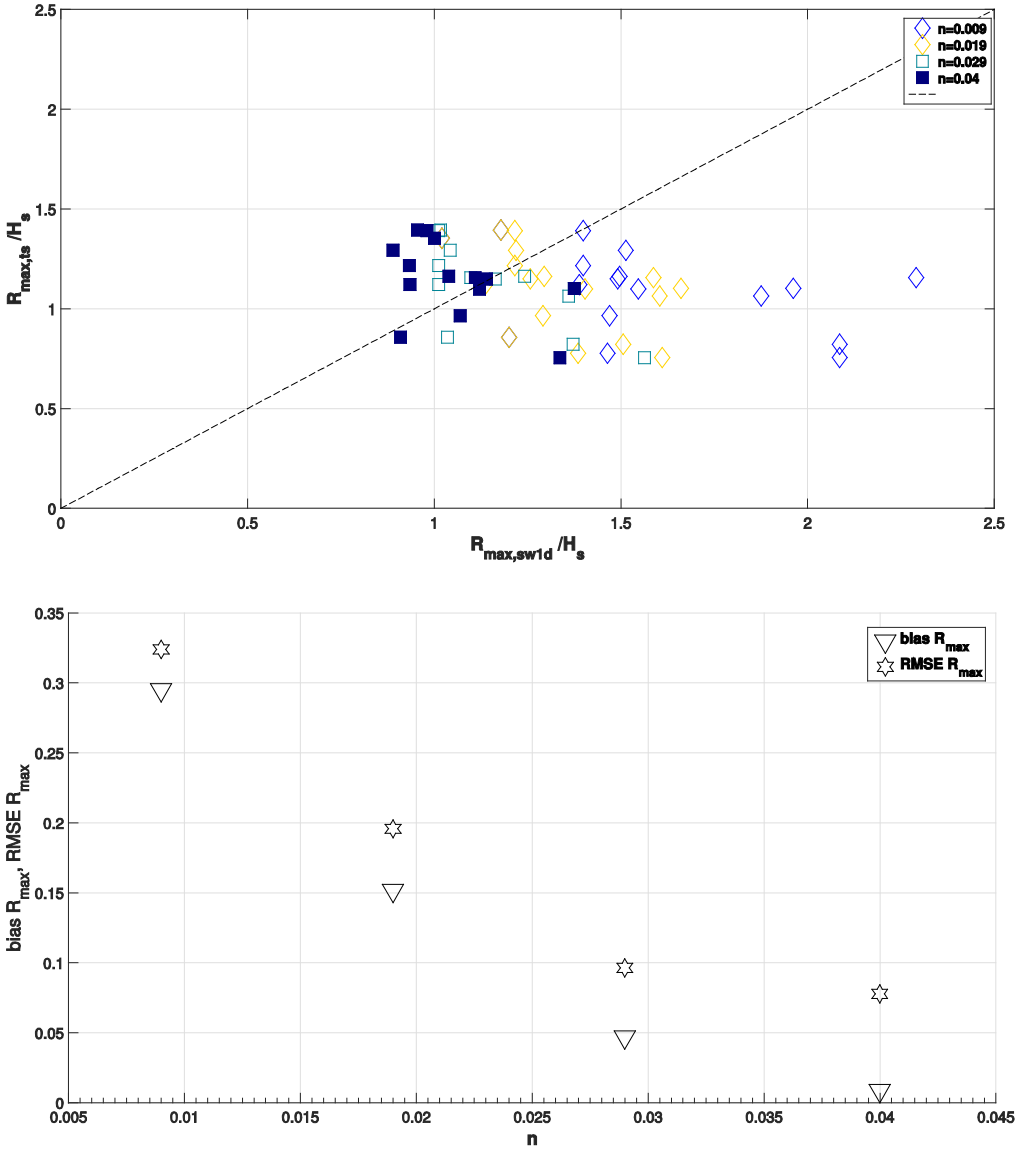

Figure 5.11 **Top:** R_{max} predicted plotted against the measured one for all transects analysed, both quantities are normalized for the significant wave height at relative boundary. **Bottom:** Sensitivity of bottom friction with respect to computed R_{max}.

5.5. Empirical run-up estimation

The prediction of extreme wave run-up on natural beaches is of particular interest for both coastal managers and land use planners, and its statistical exceedance values are very often applied in coastal engineering application. On the other side, simple and practical wave run-up predictive tool, which can be used for natural sandy beaches by coastal planners or managers, is straight forwarded. The most used formulations of those discussed in Subs. 1.1.2. , are implemented for both events Ev_1 and Ev_2, where corresponding measurements are available. Table 5.3 summarizes the results as mean values of both quantities R_2 and R_{max}, overall the transects analysed, representative of the gently curved centre of such a large embayment beach. Both quantities refer to the offshore spectral wave parameters (e.g. H_s, L_{0p}, T_p), derived from averaging the MeteOcean model inputs on the 4 points (Points N. 4, 5, 6, 7 in Figure 5.6) located at the SW boundary of SWAN grid $Gr_{150.}$

Most run-up studies have been carried out on open, macrotidal, oceanic sandy beaches approached by long-period waves even if the formulations are often used in several different beach morphologies and broad wave climate conditions, providing a wide scatter of results. While few run-up studies have been carried out on such embayment beaches (Vousdoukas et al., 2009). Predictive models of wave run-up, and specifically most of those investigated in the present work, have traditionally focused on the beach foreslope slope β_f as the key determinant of $R_{\%}$, either in studies using regular waves (Hunt, 1959, Mase, 1989), and irregular waves (Holman, 1986, Nielsen and Hanslow, 1991, Ruggiero et al., 2001, Stockdon et al., 2006). The exceptions are the model proposed by Douglass (1992) who argued that maximum run-up is independent of the beach-face slope, and the Nielsen and Hanslow (1991) model, which has no dependence on beach slope for $tan\beta_f \leq 0.1$, as the case for most of the cross-shore transects under analysis, except for 2 of them.

Summarizing, the empirical models produce a wide scatter of results when applied to these real situations, and all the models investigated, except (Mayer and Kriebel, 1994)

Table 5.3 Summary of the run-up predictions from empirical formulations, as mean values over the transects investigated for two storm events described above.

	R_2 (m)	
Time-stack	0.49	0.50
Holman (1986) $\frac{R_{2\%}}{H_{m0}} = a\xi_{0p}^{b} + c$; $a = 0.83$, b = 1, $c = 0.2$	0.92	1.13
Nielsen and Hanslow (1991) $R_{2\%} = 1.98L_{zwm}$; $L_{zwm} = \begin{cases} 0.05\sqrt{H_{rms}L_0} & \beta_f < 0.1 \\ 0.6\beta_f\sqrt{H_{rms}L_0} & \beta_f \geq 0.1 \end{cases}$	0.88	0.81
Mayer & Kriebel (1994) $R = \frac{m}{2}\left(X_b - \sqrt{H_0L_0}\right)\left[-1 + \sqrt{1 + \frac{4h_b\sqrt{H_0L_0}}{m\left(X_b - \sqrt{H_0L_0}\right)^2}}\right]$	0.52	0.56
Ruggiero et al. (2001) $R_{2\%} = 0.27\sqrt{\beta_f H_0 L_0}$	0.93	0.78
Stockdon et al. (2006) $R_{2\%} = 1.1\left(0.35\beta_f(H_0L_0)^{\frac{1}{2}} + \frac{[H_0L_0(0.563\beta_f^2 + 0.004]^{\frac{1}{2}}}{2}\right)$	0.96	0.88

	R_{max} (m)	
Time-stack	0.60	0.58
Douglas (1992) $\frac{R_{max}}{H_o} = C\sqrt{H_0/L_0}$	1.22	1.17
Mather et al. (2010) $R_{max} = CH_oS^{2/3}$	0.56	0.68

and (Mather et al., 2011) predictions for R_2 and R_{max}, respectively, mostly overestimate the observed wave run-up.

This bears witness to the fact, as suggested also in Stockdon et al., (2006), the run-up prediction using deep water buoy measurements may result in significantly higher results than those obtained using a wave height measured at a local (closer to the shore) buoy, since, in the latter condition, the wave processes (i.e. refraction and frictional dissipation mainly) could be properly taken into account. This is particularly so for the southern and southeastern events (Figure 5.3), in which refraction and diffraction effects are important, and so the effects on the computed run-up could be significant. Moreover, inundation process at a tideless embayed beach has been demonstrated to be better captured by using even the breaking wave height, H_b (Sancho-García et al., 2012). On the other side, general parameterizations generally suffer, as highlighted in Stockdon et al., (2014) from systematic errors due to site-specific characteristics that are not included in the models.

The exceptional empirical models are largely motivated in their different and well-fitted performances, by the approaches used for the calculation. In the application of the analytical solution of Mayer and Kriebel (1994), which is based on the concept of the *effective slope* (see Section 1.1.2.). The statistical exceedance value for R_2 is calculated from the time series of distance X_b and the corresponding h_b, both derived from 2-d SWASH simulations, while the m value in the original formula simply represents the foreshore beach slope, conventionally called β_f.

Whereas, Mather et al. (2010) correlate the maximum wave run-up height R_{max} with the shape of the offshore profile as well as the foreshore slope. Specifically, such an offshore limit is defined until a specified point at a certain distance x_h and depth h seaward of the surf zone, following the relationship in Eq. (5.6):

$$\frac{R_{max}}{H_0} = \left(\frac{x_h}{h}\right)^p \tag{5.6}$$

where p is comparable to the coefficient of power law in Bruun's equilibrium profile. Hence, for the model of Mather et al. (2010), the C, as a dimensionless coefficient, is

assumed to be derived for large embayment condition ($= 9$), while S is referred to a representative nearshore slope, calculated until the closure depth. The latter is estimated by using Berkemeier formula (AdB-Puglia, 2015), at a depth of around $5.4\ m$.

The straightforward usage of the empirical model can give a general view on a maximum wave run-up during most of the cases, corresponding to a safe side attitude. However, for research and engineering purposes, to define the run-up, and consequently the potential flooded area at such an embayed beach, the use of overused empirical formulation with deep water wave measurements determine high overestimated results.

5.6. Conclusions

Wave run-up motions deliver much of the energy responsible for beach erosion and define the area that can be flooded; hence, its predictability has become increasingly crucial. The new video monitoring system after a close collaboration between DICATECh department of Technical University of Bari, ACIC (Multitel Spin-off) installed and implemented in the Apulia region AdBP monitoring network, is used in order to measure run-up at the beach, in the central area of the embayment at Torre Lapillo, by using time-stack images.

Several transects alongshore, framed by both cameras installed and 2 storm events are chosen for analysis. The methodology implemented for time-stack collection and accurate processing is described and discussed. Numerical simulations for run-up calculations have been performed for both events introduced.

The computational approach introduced in this chapter combines two different wave and wave-flow models, SWAN and SWASH respectively, opportunely nested, forced by MeteOcean forecasting model input, provided by DICCA Department, Genoa University. This allows the study of waves at different time and spatial scales, from deep water up to the total energy dissipation in the swash zone. Considering the high computational demands of the SWASH flow model, short periods' simulation has to be considered. In

order to properly represent the complex hydrodynamic interactions at the beach profile, one could benefit from the use of a high-resolution representation of the sub-aerial surface. So, it is here introduced a merging strategy of different field surveys data and instruments. Specifically, the highly detailed DSM UAV-derived, which provides a surface map with an altimetric accuracy in the order of few cm, is implemented as topographic input. The small difference in time date between the UAV survey and the wave measurements and simulations (few days) is assumed to not influence results. On the other side, the bathymetry is provided by a highly detailed Multibeam dataset, and since this do not cover the whole seabed area until shoreline, from around $1\ m$ depth to shoreline it is solved by using the d-RTK GPS surveys data. This last input aggregation is needed and cannot be circumvented since it is useful to solve properly the swash zone.

The use of UAV and the reconstruction of DSM by using non standard photogrammetric techniques to be implemented as topographic input could so represent a reliable solution for being included in 2-d hydrodynamic simulation set-up, allowing to fully resolve the alongshore components of bathymetry, wave groups, and swash. This alternative solution to time-consuming, point-by-point, d-RTK GPS survey, is demonstrated to represent a very valid tool, accurate and low-cost, particularly useful for those fragile, complex coastal areas, where single cross-shore transects give no guarantee to well represent the shore. Considering the actual condition of Apulia beaches, and generally, of Italian shores, the coastal managers, who take care of ensuring the optimal administration and preservation of these areas, could benefit from the easy and quick deployment of UAV surveys. Furthermore, by defining strategies useful in order to make measurements available within given time interval, continuous monitoring of i.e. potential sources of Aeolian sediments, dune evolution, and beach nourishments progress could be performed (Gonçalves and Henriques, 2015, Long et al., 2016). Few operational constraints today remain; related i.e. to environmental conditions, mainly the wind, which pose the primary difficulty or the placing task of artificial ground control on large or irregular areas.

Run-up is numerically simulated by using SWASH and it is compared to observations to investigate the simulation accuracy. Specifically, the comparison of event Ev_2 run-up results, by using 2-d simulation suggests an optimal representation of swash zone. The $bias$ in R_2 calculation is actually of around $-0.06\,m$ and $RMSE$ around $0.08\,m$ which is quite in line also with the overall accuracy of the DSM. The choices of the appropriate peak spectral waves and water levels are crucial for a good representation of the storm waves and the associate swash phenomena, so the choice of MeteOcean for boundaries condition and taking advantage of the tidal gauges retained by the coastal network of AdBP, constitute a very attractive solution for being implemented in a modelling chain.

In summary, the methodology proposed and employed in this study can be used as a practical tool for identification of the potential run-up excursion, exceedance values and if the case, extreme flooding analysis at the embayment of Torre Lapillo, thus providing a valuable information for coastal authorities, to be also extended on the coasts of Apulia region, affected by wide erosion phenomena.

The danger of using numerical models is often referable to the fact that the results may depend on poorly constrained model-parameter assumptions, many of which are contained in the default configuration. Here, it is not explored a sensitivity study on the best parameter choices on the basis of predicted wave-heights, since no precise wave measurements are available. Whereas, it has been stated that changing the friction Manning coefficient can have a significant effect on the 1-d SWASH modelled run-up and so, the extents of inundation. If SWASH is used for estimating real-world hazards, users should think carefully about choosing an appropriate value, and may want to run sensitivity studies. In this study, the 1-d SWASH results are satisfying with an ad-hoc calibration of the Manning value of the friction coefficient and $\mathrm{n} = 0.04\ s/m^{1/3}$ results to best fit the time-stack measurements.

Unfortunately, only very few data and field experiments at this region are available until now, which makes impossible to properly evaluate the overall sensitivity of the models on the two spatial domain, especially during severe events.

The reliability of empirical model formulations, which are of great interest for both coastal planners and managers, is evaluated. The empirical models usually have over-estimated the video-measurements and numerical model predictions and this has been associated with the fact that the most of them do not take into account complex hydro-dynamic processes, the propagation from intermediate to shallow water waves, properly. Whereas, by including information of the overall nearshore slope or the breaking points opportunely, only the models of Mayer and Kriebel (1994) and Mather et al. (2011) are capable of better capturing the run-up phenomena, in term of R_2 and R_{max}, respectively, with low errors in predictions.

Conclusions

Main Summary and future works

The Apulia is one of the regions along the Italian coast most affected by erosion phenomena. In this context, with the aim of a long-term morphological monitoring of beaches, this research project has been primarily addressed to an in-depth understanding of the core features and functionalities of a coastal video monitoring system in order to be embedded in the monitoring network established by the local AdBP. In the present work, the development of a new coastal video monitoring system has been described, and few main video applications investigated. Moreover, numerical modelling of run-up on sandy beach has been applied by also employing a modelling chain, which include a DSM derived from Unmanned Aerial Vehicle imagery.

One main functionality to be implemented in the video system is the completely automatic shoreline detection; so on the basis of a database of Timex images, from a system installed back in the 2006 at Alimini (Le), a new routine for automatic image segmentation and shoreline detection is built. The Shoreline Detection Model (SDM) is based on the identification of sea/sand boundary from automatic segmented coastal images, framed by visible camera. The routine is constructed by pairing multiscale local brightness, colour, and texture cues with a globalization framework, by using spectral clustering and then by implementing image segmentation tasks, taking advantage from state-of-the-art algorithms. Validation results, based on cross-shore differences between manual and automatic contours at several transects, have showed to guarantee high performance (less than $2\ pixels$ over the validation dataset).

The video system developed includes some core factors such as easy installation, robustness, low cost, efficiency of the acquisition and tasks scheduling. In December 2015, two video monitoring stations were installed at two sites on Apulian coasts, in Torre Canne (Br) e Torre Lapillo (Le), which born to work completely automatically. Non-metric IP surveillance cameras are employed and they have been verified to accurately quantify coastal processes. Several coastal information can be provided from

images. In particular, the SDM has been tested at Torre Lapillo, confirming the feasibility of the model to be extended at different sites. Results on intertidal bathymetry derived from video analysis are also presented, the comparison with d-RTK GPS surveys shows a very good agreement, with a mean RMS error, overall investigated transects, equals to 0.025 m. The vertical precision in coastal features extraction obtained is quite similar to other systems and comparable to standard surveys methods.

Routines for automatic georectification of images with respect to the sea level registered by the nearest tide gauge, opportunely filtered, are included. Furthermore, embracing the idea of a people-centred information system, the dissemination of results on a web portal has enhanced the system potential, allowing, in quasi real time, to view and download, for free, processed images from all camera installed, shoreline maps and time shoreline variation on user-specified transects, in cross-shore direction.

The further researches in this context are addressed to improve the SDM performance, by down-warding the minimum scale parameter σ of local cues, in order to be completely insensitive to the height and the distance of the camera, and to test new calibration methods based i.e. on learning process simply including pixels seeds area histograms. Moreover, the thermal camera, installed in Torre Canne, will be beneficial for supporting the visible stream during nightlight hours and for evaluating the *gPb* capabilities for the segmentation of upper intertidal area in order to the study of potential sources of Aeolian sediment. Future system developments would include the integration of routines for linking the exact wet/dry interface elevation to more specialized hydrodynamic model results in order to take into account accurate swash prediction, then for estimating beach states and the design of a communication infrastructure that will enable to use the new system in a real time coastal hazard warning system.

By exploiting the coastal video station in the centre of the embayment at Torre Lapillo, run-up measurements are undertaken via video time-stacks. Furthermore, the UAV imagery post-processed by applying photogrammetric/computer vision approach, the Structure from Motion algorithm, in order to solve the topography in such a peculiar beach environment, has demonstrated to determine high vertical accuracy. This leaded

to focus into run-up predictions, in term of exceedance and maxima values, by simulating the hydrodynamics using SWASH numerical model for comparison with the observations. The availability of the topographical DSM input and a high detailed Multibeam dataset, for submerged beach, have allowed to build a high resolute 2-d model which allows to fully resolve the alongshore components of bathymetry, the wave groups, and swash. The bias in R_2 calculation over several transects is of around $0.06\,m$ and $RMSE$ around $0.08\,m$ which demonstrates a good correlation with the measured values. While, in order to assess 1-d SWASH modelling performance, a sensitivity analysis has been conducted. Changing the friction coefficient (Manning) has been verified to have a significant effect on the extent of run-up, which lead to obtain appreciable results only with $n = 0.04\ s/m^{1/3}$.

Furthermore, empirical model formulations are used to calculate run-up predictions. An overestimation trend is confirmed for the majority of them. Only the models that integrate information of the overall nearshore slope or the breaking points opportunely (Meyer and Kriebel (1994) and Mather et al. (2011)) have been verified to better capture the phenomena.

The 2-d novel methodology proposed and employed in this study can be used as a practical tool for identification of the run-up during storms on the coast of the embayment of Torre Lapillo, thus providing crucial information for coastal authorities, valuable to be extended also on other coasts of Apulia region, affected by wide erosion phenomena.

Unfortunately, few data and field experiments at this region are available until now, which makes impossible to properly evaluate the sensitivity of the SWASH models on the two spatial domains. Further researches are hence addressed at the collection of a more consistent dataset. In addition, this dataset would be very useful for deploying a local appropriate empirical formulation or calibrate coefficients of an existing model.

References

Aarninkhof, S. G., Turner, I. L., Dronkers, T. D., Caljouw, M. & Nipius, L. 2003. A video-based technique for mapping intertidal beach bathymetry. *Coastal Engineering,* 49**,** 275-289.

Aarninkhof, S. G. J. 2003. *Nearshore bathymetry derived from video imagery*, TU Delft, Delft University of Technology.

Aarninkhof, S. G. J., Roelvink, J.A. 1999. Argus-based monitoring of intertidal beach morphodimanics. *Proc. Coastal sediment,* 1999**,** 15.

AdB-Puglia 2015. Relazione tecnica finale: "Monitoraggio delle dinamiche meteo-marine di controllo dei fenomeni di erosione delle coste".

Aedla, R., Dwarakish, G. S. & Reddy, D. V. 2015. Automatic Shoreline Detection and Change Detection Analysis of Netravati-GurpurRivermouth Using Histogram Equalization and Adaptive Thresholding Techniques. *Aquatic Procedia,* 4**,** 563-570.

Agisoft, L. & Manual, A. P. U. Professional Edition. *Version 1.2.4. 2016: Agisoft LLC*.

Akpınar, A., van Vledder, G. P., Kömürcü, M. İ. & Özger, M. 2012. Evaluation of the numerical wave model (SWAN) for wave simulation in the Black Sea. *Continental Shelf Research,* 50**,** 80-99.

Almeida, L. P., Masselink, G., Russell, P. E. & Davidson, M. A. 2015. Observations of gravel beach dynamics during high energy wave conditions using a laser scanner. *Geomorphology,* 228**,** 15-27.

AMP, P. C. 2014. BIOMAP - BIOcostruzioni MArine in Puglia, si inquadra nell'ambito del programma - Interventi per la rete ecologica. Porto Cesareo Area Marina Protetta di Porto Cesareo.

Anders, F. J. & Byrnes, M. R. 1991. Accuracy of shoreline change rates as determined from maps and aerial photographs. *Shore and Beach,* 59**,** 17-26.

Ansar, A. & Daniilidis, K. 2003. Linear pose estimation from points or lines. *Pattern Analysis and Machine Intelligence, IEEE Transactions on,* 25**,** 578-589.

Arbelaez, P. Boundary extraction in natural images using ultrametric contour maps. Computer Vision and Pattern Recognition Workshop, 2006. CVPRW'06. Conference on, 2006. IEEE, 182-182.

Arbeláez, P. & Cohen, L. Constrained image segmentation from hierarchical boundaries. Computer Vision and Pattern Recognition, 2008. CVPR 2008. IEEE Conference on, 2008. IEEE, 1-8.

Arbelaez, P., Maire, M., Fowlkes, C. & Malik, J. From contours to regions: An empirical evaluation. Computer Vision and Pattern Recognition, 2009. CVPR 2009. IEEE Conference on, 2009. IEEE, 2294-2301.

Arbelaez, P., Maire, M., Fowlkes, C. & Malik, J. 2011. Contour detection and hierarchical image segmentation. *Pattern Analysis and Machine Intelligence, IEEE Transactions on,* 33**,** 898-916.

Archetti, R. & Zanuttigh, B. 2010. Integrated monitoring of the hydro-morphodynamics of a beach protected by low crested detached breakwaters. *Coastal Engineering,* 57**,** 879-891.

Baldock, T. E., Kudo, A., Guard, P. A., Alsina, J. M. & Barnes, M. P. 2008. Lagrangian measurements and modelling of fluid advection in the inner surf and swash zones. *Coastal Engineering,* 55**,** 791-799.

Battjes, J. 1974. Surf similarity. *Coastal Engineering Proceedings,* 1.

Battjes, J. & Janssen, J. 1978. Energy loss and set-up due to breaking of random waves. *Coastal Engineering Proceedings,* 1.

Bay, H., Ess, A., Tuytelaars, T. & Van Gool, L. 2008. Speeded-up robust features (SURF). *Computer vision and image understanding,* 110**,** 346-359.

Besio, G. 2012. *MeteOcean - Home Page DICCA* [Online]. Dipartimento di Ingegneria civile, chimica e ambientale (DICCA). Available: http://www.dicca.unige.it/meteocean/model.html.

Beucher, S. & Meyer, F. 1992. The morphological approach to segmentation: the watershed transformation. *OPTICAL ENGINEERING-NEW YORK-MARCEL DEKKER INCORPORATED-,* 34**,** 433-433.

Blenkinsopp, C. E., Matias, A., Howe, D., Castelle, B., Marieu, V. & Turner, I. L. 2016. Wave runup and overwash on a prototype-scale sand barrier. *Coastal Engineering,* 113**,** 88-103.

Blenkinsopp, C. E., Mole, M. A., Turner, I. L. & Peirson, W. L. 2010. Measurements of the time-varying free-surface profile across the swash zone obtained using an industrial LIDAR. *Coastal Engineering,* 57**,** 1059-1065.

Blenkinsopp, C. E., Turner, I. L., Masselink, G. & Russell, P. E. 2011. Swash zone sediment fluxes: Field observations. *Coastal Engineering,* 58**,** 28-44.

Boak, E. H. & Turner, I. L. 2005. Shoreline Definition and Detection: A Review. *Journal of Coastal Research***,** 688-703.

Booij, N., Holthuijsen, L. & Ris, R. 1996. The" SWAN" wave model for shallow water. *Coastal Engineering Proceedings,* 1.

Bouguet, J.-Y. 2004. Camera calibration toolbox for matlab.

Bradski, G. & Kaehler, A. 2008. *Learning OpenCV: Computer vision with the OpenCV library*, " O'Reilly Media, Inc.".

Bresenham, J. E. 1965. Algorithm for computer control of a digital plotter. *IBM Systems journal,* 4**,** 25-30.

Brignone, M., Schiaffino, C. F., Isla, F. I. & Ferrari, M. 2012. A system for beach video-monitoring: Beachkeeper plus. *Computers & Geosciences,* 49**,** 53-61.

Brocchini, M. & Baldock, T. E. 2008. Recent advances in modeling swash zone dynamics: Influence of surf-swash interaction on nearshore hydrodynamics and morphodynamics. *Reviews of Geophysics,* 46**,** n/a-n/a.

Bruno, M., Molfetta, M. & Petrillo, A. 2014. The influence of interannual variability of mean sea level in the Adriatic Sea on extreme values. *Journal of Coastal Research,* 70**,** 241-246.

Bruno, M. F., Molfetta, M. G., Mossa, M., Nutricato, R., Morea, A. & Chiaradia, M. T. 2016. Coastal Observation through Cosmo-SkyMed High-Resolution SAR Images. *Journal of Coastal Research***,** 795-799.

Camfield, F. E. & Morang, A. 1996. Defining and interpreting shoreline change. *Ocean & Coastal Management,* 32**,** 129-151.

Canesso, D., Cordella, M. & Arena, G. 2012. Manuale di mareografia e linee guida per i processi di validazione dei dati mareografici. ISPRA, Manuali e Linee guida.

Canny, J. 1986. A computational approach to edge detection. *IEEE Transactions on pattern analysis and machine intelligence***,** 679-698.

Casella, E., Rovere, A., Pedroncini, A., Mucerino, L., Casella, M., Cusati, L. A., Vacchi, M., Ferrari, M. & Firpo, M. 2014. Study of wave runup using numerical models and low-altitude aerial photogrammetry: A tool for coastal management. *Estuarine, Coastal and Shelf Science,* 149**,** 160-167.

Cavaleri, L. & Rizzoli, P. M. 1981. Wind wave prediction in shallow water: Theory and applications. *Journal of Geophysical Research: Oceans,* 86**,** 10961-10973.

Collins, J. I. 1972. Prediction of shallow-water spectra. *Journal of Geophysical Research,* 77**,** 2693-2707.

Damiani, L., Aristodemo, F., Saponieri, A., Verbeni, B., Veltri, P. & Vicinanza, D. 2011. Full-scale experiments on a beach drainage system: hydrodynamic effects inside beach. *Journal of Hydraulic Research,* 49**,** 44-54.

Damiani, L. & Molfetta, M. A video based technique for shoreline monitoring in Alimini (LE). Coastlab08, 2008. L. Damiani, M. Mossa, 153-156.

Davidson, M., Van Koningsveld, M., de Kruif, A., Rawson, J., Holman, R., Lamberti, A., Medina, R., Kroon, A. & Aarninkhof, S. 2007. The CoastView project: Developing video-derived Coastal State Indicators in support of coastal zone management. *Coastal Engineering,* 54**,** 463-475.

De Roo, S., Suzuki, T., Kolokythos, G., Zhao, G. & Verwaest, T. Numerical modelling of 2D wave transformation processes from nearshore to a shallow foreshore: comparison between the Mike21, swash and XBeach models. 36th IAHR World Congress, 2015. 1-6.

Delle Rose, M. 2015. Medium-term Erosion Processes of South Adriatic Beaches (Apulia, Italy): A Challenge for an Integrated Coastal Zone Management. *J Earth Sci Clim Change,* 6, 2.

Dijkstra, E. W. 1959. A note on two problems in connexion with graphs. *Numerische mathematik,* 1, 269-271.

Dolan, R., Fenster, M. S. & Holme, S. J. 1991. Temporal analysis of shoreline recession and accretion. *Journal of coastal research*, 723-744.

Douglas, B. C., Crowell, M. & Leatherman, S. P. 1998. Considerations for shoreline position prediction. *Journal of Coastal Research*, 1025-1033.

Douglass, S. L. 1992. Estimating extreme values of run-up on beaches. *Journal of waterway, port, coastal, and ocean engineering,* 118, 220-224.

Eggert, C. 2012. *Implementation and Evaluation of the gPb Contour Detector.* MSc, Augsburg University.

Engström, P., Larsson, H. & Rydell, J. Geometric calibration of thermal cameras. 2013. 88970C-88970C-8.

Fiore, P. D. 2001. Efficient linear solution of exterior orientation. *IEEE Transactions on Pattern Analysis & Machine Intelligence*, 140-148.

Fischler, M. A. & Bolles, R. C. 1981. Random sample consensus: a paradigm for model fitting with applications to image analysis and automated cartography. *Communications of the ACM,* 24, 381-395.

Fonstad, M. A., Dietrich, J. T., Courville, B. C., Jensen, J. L. & Carbonneau, P. E. 2013. Topographic structure from motion: a new development in photogrammetric measurement. *Earth Surface Processes and Landforms,* 38, 421-430.

Fragakis, C. 2002. Preface. *Coastal Engineering,* 47, 79-80.

Furukawa, Y. & Ponce, J. 2010. Accurate, dense, and robust multiview stereopsis. *IEEE transactions on pattern analysis and machine intelligence,* 32, 1362-1376.

Gao, X.-S., Hou, X.-R., Tang, J. & Cheng, H.-F. 2003. Complete solution classification for the perspective-three-point problem. *Pattern Analysis and Machine Intelligence, IEEE Transactions on,* 25, 930-943.

Gonçalves, J. & Henriques, R. 2015. UAV photogrammetry for topographic monitoring of coastal areas. *ISPRS Journal of Photogrammetry and Remote Sensing,* 104, 101-111.

Group, T. W. 1988. The WAM model-a third generation ocean wave prediction model. *Journal of Physical Oceanography,* 18, 1775-1810.

Guimarães, P. V., Farina, L., Toldo, E., Diaz-Hernandez, G. & Akhmatskaya, E. 2015. Numerical simulation of extreme wave runup during storm events in Tramandaí Beach, Rio Grande do Sul, Brazil. *Coastal Engineering,* 95, 171-180.

Guza, R. T. & Thornton, E. B. 1982. Swash oscillations on a natural beach. *Journal of Geophysical Research: Oceans,* 87, 483-491.

Hartley, R. & Zisserman, A. 2003. *Multiple view geometry in computer vision*, Cambridge university press.

Harwin, S. & Lucieer, A. 2012. Assessing the accuracy of georeferenced point clouds produced via multi-view stereopsis from unmanned aerial vehicle (UAV) imagery. *Remote Sensing,* 4, 1573-1599.

Hasselmann, K. 1974. On the spectral dissipation of ocean waves due to white capping. *Boundary-Layer Meteorology,* 6, 107-127.

Hasselmann, K., Barnett, T., Bouws, E., Carlson, H., Cartwright, D., Enke, K., Ewing, J., Gienapp, H., Hasselmann, D. & Kruseman, P. 1973. Measurements of wind-wave growth and swell decay during the Joint North Sea Wave Project (JONSWAP). Deutches Hydrographisches Institut.

Hofland, B., Diamantidou, E., van Steeg, P. & Meys, P. 2015. Wave runup and wave overtopping measurements using a laser scanner. *Coastal Engineering,* 106, 20-29.

Holland, K. T., Holman, R. A., Lippmann, T. C., Stanley, J. & Plant, N. 1997. Practical use of video imagery in nearshore oceanographic field studies. *Ieee Journal of Oceanic Engineering,* 22, 81-92.

Holman, R. 1986. Extreme value statistics for wave run-up on a natural beach. *Coastal Engineering,* 9, 527-544.

Holman, R., Plant, N. & Holland, T. 2013. cBathy: A robust algorithm for estimating nearshore bathymetry. *Journal of Geophysical Research: Oceans,* 118, 2595-2609.

Holman, R. A. & Sallenger, A. H. 1986. High-energy nearshore processes. *Eos, Transactions American Geophysical Union,* 67, 1369-1371.

Holman, R. A. & Stanley, J. 2007a. The history and technical capabilities of Argus. *Coastal Engineering,* 54, 477-491.

Holman, R. A. & Stanley, J. 2007b. The history and technical capabilities of Argus. *Coastal Engineering,* 54, 477-491.

Hoonhout, B., Radermacher, M., Baart, F. & Van der Maaten, L. 2015. An automated method for semantic classification of regions in coastal images. *Coastal Engineering,* 105, 1-12.

Horaud, R., Dornaika, F. & Lamiroy, B. 1997. Object pose: The link between weak perspective, paraperspective, and full perspective. *International Journal of Computer Vision,* 22, 173-189.

Hunt, I. A. 1959. Design of sea-walls and breakwaters. *Transactions of the American Society of Civil Engineers,* 126, 542-570.

Janssen, P. A. 1989. Wave-induced stress and the drag of air flow over sea waves. *Journal of Physical Oceanography,* 19, 745-754.

Jimenez, J. A., Osorio, A., Marino-Tapia, I., Davidson, M., Medina, R., Kroon, A., Archetti, R., Ciavola, P. & Aamikhof, S. G. J. 2007. Beach recreation planning using video-derived coastal state indicators. *Coastal Engineering,* 54, 507-521.

Kendall, D. G. 1989. A survey of the statistical theory of shape. *Statistical Science*, 87-99.

Kingston, K. S. 2003. Applications of complex adaptive systems approaches to coastal systems.

Kobayashi, N. 1999. Wave runup and overtopping on beaches and coastal structures. *Advances in coastal and ocean engineering,* 5, 95-154.

Komar, P. D., Díaz-Méndez, G. M. & Marra, J. J. 2001. Stability of the New River Spit, and the position of Oregon's beach-zone line. *Journal of Coastal Research*, 625-635.

Komen, G., Hasselmann, K. & Hasselmann, K. 1984. On the existence of a fully developed wind-sea spectrum. *Journal of physical oceanography,* 14, 1271-1285.

Kong, T. Y. & Rosenfeld, A. 1996. *Topological algorithms for digital image processing*, Elsevier.

Kroon, A., Davidson, M. A., Aarninkhof, S. G. J., Archetti, R., Armaroli, C., Gonzalez, M., Medri, S., Osorio, A., Aagaard, T., Holman, R. A. & Spanhoff, R. 2007. Application of remote sensing video systems to coastline management problems. *Coastal Engineering,* 54, 493-505.

Lagarias, J. C., Reeds, J. A., Wright, M. H. & Wright, P. E. 1998. Convergence properties of the Nelder--Mead simplex method in low dimensions. *SIAM Journal on optimization,* 9, 112-147.

Lee, J.-M., Park, J.-Y. & Choi, J.-Y. 2013. Evaluation of sub-aerial topographic surveying techniques using total station and RTK-GPS for applications in macrotidal sand beach environment. *Journal of Coastal Research,* 65, 535-540.

Lippmann, T. & Holman, R. A. 1989. Quantification of sand bar morphology: a video technique based on wave dissipation. *Journal of Geophysical Research: Oceans (1978–2012),* 94**,** 995-1011.

Lisi, I., Molfetta, M., Bruno, M., DiRisio, M. & Damiani, L. 2011. Morphodynamic classification of sandy beaches in enclosed basins: the case study of Alimini (Italy). *Journal of Coastal Research***,** 180.

List, J. H. & Farris, A. S. Large-scale shoreline response to storms and fair weather. Coastal Sediments, 1999. ASCE, 1324-1338.

Long, N., Millescamps, B., Guillot, B., Pouget, F. & Bertin, X. 2016. Monitoring the Topography of a Dynamic Tidal Inlet Using UAV Imagery. *Remote Sensing,* 8**,** 387.

Lu, C.-P., Hager, G. D. & Mjolsness, E. 2000. Fast and globally convergent pose estimation from video images. *Pattern Analysis and Machine Intelligence, IEEE Transactions on,* 22**,** 610-622.

MacQueen, J. Some methods for classification and analysis of multivariate observations. Proceedings of the fifth Berkeley symposium on mathematical statistics and probability, 1967. Oakland, CA, USA., 281-297.

Madsen, O. S., Poon, Y.-K. & Graber, H. C. 1988. Spectral wave attenuation by bottom friction: theory. *Coastal Engineering Proceedings,* 1.

Maire, M. 2009. *Contour detection and Image Segmentation.* Dissertation, University of California, Berkeley.

Mancini, F., Dubbini, M., Gattelli, M., Stecchi, F., Fabbri, S. & Gabbianelli, G. 2013. Using Unmanned Aerial Vehicles (UAV) for high-resolution reconstruction of topography: The structure from motion approach on coastal environments. *Remote Sensing,* 5**,** 6880-6898.

Mangor, K. 2001. *Shoreline management guidelines*, DHI Water & Environment.

Martin, D., Fowlkes, C., Tal, D. & Malik, J. A database of human segmented natural images and its application to evaluating segmentation algorithms and measuring ecological statistics. Computer Vision, 2001. ICCV 2001. Proceedings. Eighth IEEE International Conference on, 2001. IEEE, 416-423.

Martin, D. R., Fowlkes, C. C. & Malik, J. 2004. Learning to Detect Natural Image Boundaries Using Local Brightness, Color, and Texture Cues. *IEEE Trans. Pattern Anal. Mach. Intell.,* 26**,** 530-549.

Mase, H. 1989. Random wave runup height on gentle slope. *Journal of Waterway, Port, Coastal, and Ocean Engineering,* 115**,** 649-661.

Masselink, G., Hughes, M. & Knight, J. 2014. *Introduction to coastal processes and geomorphology*, Routledge.

Mather, A. A., Stretch, D. & Garland, G. 2011. WAVE RUN UP ON NATURAL BEACHES. *Coastal Engineering Proceedings,* 1**,** 45.

Mayer, R. & Kriebel, D. 1994. Wave runup on composite-slope and concave beaches. *Coastal Engineering Proceedings,* 1.

McBride, R. A., Hiland, M. W., Penland, S., Williams, S. J., Byrnes, M. R., Westphal, K. A., Jaffe, B. E. & Sallenger, A. H. Mapping barrier island changes in Louisiana: techniques, accuracy, and results. Coastal Sediments, 1991. ASCE, 1011-1026.

MeilPa, M. & Shi, J. Learning segmentation by random walks. Neural Information Processing Systems, 2001.

Melby, J., Caraballo-Nadal, N. & Kobayashi, N. 2012. Wave runup prediction for flood mapping. *Coastal Engineering Proceedings,* 1**,** 79.

Mentaschi, L., Besio, G., Cassola, F. & Mazzino, A. 2015. Performance evaluation of Wavewatch III in the Mediterranean Sea. *Ocean Modelling,* 90**,** 82-94.

Miles, J. W. 1957. On the generation of surface waves by shear flows. *Journal of Fluid Mechanics,* 3**,** 185-204.

Moore, L. J., Benumof, B. T. & Griggs, G. B. 1999. Coastal erosion hazards in Santa Cruz and San Diego Counties, California. *Journal of Coastal Research***,** 121-139.

Najman, L. & Schmitt, M. 1996. Geodesic saliency of watershed contours and hierarchical segmentation. *Pattern Analysis and Machine Intelligence, IEEE Transactions on,* 18**,** 1163-1173.

Naumann, M., Geist, M., Bill, R., Niemeyer, F. & Grenzdörffer, G. 2013. Accuracy comparison of digital surface models created by unmanned aerial systems imagery and terrestrial laser scanner. *International Archives of the Photogrammetry, Remote Sensing and Spatial Information Sciences,* 5**,** W2.

Ng, A. Y., Jordan, M. I. & Weiss, Y. 2002. On spectral clustering: Analysis and an algorithm. *Advances in neural information processing systems,* 2**,** 849-856.

Nielsen, P. & Hanslow, D. J. 1991. Wave runup distributions on natural beaches. *Journal of Coastal Research***,** 1139-1152.

NOAA. 2013. *WAVEWATCH III® Model* [Online]. Marine Modeling and Analysis Branch, 5830 University Research Court, College Park, MD 20740. 2016].

Osorio, A. F., Medina, R. & Gonzalez, M. 2012. An algorithm for the measurement of shoreline and intertidal beach profiles using video imagery: PSDM. *Computers & Geosciences,* 46**,** 196-207.

Parker, B. 2001. Where is the shoreline?: the answer is not as simple as one might expect.

Penate-Sanchez, A., Andrade-Cetto, J. & Moreno-Noguer, F. 2013. Exhaustive linearization for robust camera pose and focal length estimation. *Pattern Analysis and Machine Intelligence, IEEE Transactions on,* 35, 2387-2400.

Pérez Muñoz, J. C., Ortiz Alarcón, C. A., Osorio, A. F., Mejía, C. E. & Medina, R. 2013. Environmental applications of camera images calibrated by means of the Levenberg–Marquardt method. *Computers & Geosciences,* 51, 74-82.

Peter, R., Komar, P. D., William, G. M., John, J. M. & Reggie, A. B. 2001. Wave Runup, Extreme Water Levels and the Erosion of Properties Backing Beaches. *Journal of Coastal Research,* 17, 407-419.

Petrillo, A. F. & LIC 2010. Determinazione del clima meteomarino al largo e sottocosta e del trasporto solido per paraggi significativi della costa pugliese. Bari: DIAC.

Peyré, G. & Cohen, L. D. Landmark-based geodesic computation for heuristically driven path planning. Computer Vision and Pattern Recognition, 2006 IEEE Computer Society Conference on, 2006. IEEE, 2229-2236.

Phillips, O. M. 1957. On the generation of waves by turbulent wind. *J. Fluid Mech,* 2, 417-445.

Pitman, S. 2014. Methods for field measurement and remote sensing of the swash zone.

Plant, N. G., Aarninkhof, S. G., Turner, I. L. & Kingston, K. S. 2009. The performance of shoreline detection models applied to video imagery.

Plant, N. G., Holland, K. T. & Haller, M. C. 2008. Ocean wavenumber estimation from wave-resolving time series imagery. *Geoscience and Remote Sensing, IEEE Transactions on,* 46, 2644-2658.

Plant, N. G. & Holman, R. A. 1997. Intertidal beach profile estimation using video images. *Marine Geology,* 140, 1-24.

Pranzini, E., Wetzel, L. & Williams, A. T. 2015. Aspects of coastal erosion and protection in Europe. *Journal of Coastal Conservation,* 19, 445-459.

Priest, G. R. 1999. Coastal shoreline change study northern and central Lincoln county, Oregon. *Journal of Coastal Research*, 140-157.

Quartel, S., Addink, E. & Ruessink, B. 2006. Object-oriented extraction of beach morphology from video images. *International journal of applied earth observation and geoinformation,* 8, 256-269.

Radermacher, M., Wengrove, M., Van Thiel de Vries, J. & Holman, R. Applicability of video-derived bathymetry estimates to nearshore current model predictions. Proceedings of the 13th International Coastal Symposium, Durban, South Africa, 13-17 April 2014. Journal of Coastal Research, Special Issue 70, 2014, 2014. Coastal Education and Research Foundation (CERF).

Raubenheimer, B., Guza, R., Elgar, S. & Kobayashi, N. 1995. Swash on a gently sloping beach. *Journal of Geophysical Research: Oceans,* 100, 8751-8760.

Raubenheimer, B. & Guza, R. T. 1996. Observations and predictions of run-up. *Journal of Geophysical Research: Oceans,* 101, 25575-25587.

Reis, A. H. & Gama, C. 2010. Sand size versus beachface slope—An explanation based on the constructal law. *Geomorphology,* 114, 276-283.

Ren, X. 2008. Multi-scale improves boundary detection in natural images. *Computer Vision–ECCV 2008.* Springer.

Rigos, A., Andreadis, O., Andreas, M., Vousdoukas, M., Tsekouras, G. & Velegrakis, A. 2014. Shoreline Extraction from Coastal Images Using Chebyshev Polynomials and RBF Neural Networks. *In:* Iliadis, L., Maglogiannis, I. & Papadopoulos, H. (eds.) *Artificial Intelligence Applications and Innovations.* Springer Berlin Heidelberg.

Roberts, T. M., Wang, P. & Kraus, N. C. 2010. Limits of wave runup and corresponding beach-profile change from large-scale laboratory data. *Journal of Coastal Research*, 184-198.

Roerdink, J. B. & Meijster, A. 2000. The watershed transform: Definitions, algorithms and parallelization strategies. *Fundamenta informaticae,* 41, 187-228.

Rogers, W. E., Kaihatu, J. M., Hsu, L., Jensen, R. E., Dykes, J. D. & Holland, K. T. 2007. Forecasting and hindcasting waves with the SWAN model in the Southern California Bight. *Coastal Engineering,* 54, 1-15.

Ruessink, B., Kleinhans, M. & den Beukel, P. 1998. Observations of swash under highly dissipative conditions. *Journal of Geophysical Research: Oceans,* 103, 3111-3118.

Ruggiero, P., Holman, R. A. & Beach, R. A. 2004. Wave run-up on a high-energy dissipative beach. *Journal of Geophysical Research: Oceans,* 109, n/a-n/a.

Ruggiero, P., Komar, P. D., McDougal, W. G., Marra, J. J. & Beach, R. A. 2001. Wave runup, extreme water levels and the erosion of properties backing beaches. *Journal of Coastal Research*, 407-419.

Rusu, L., Pilar, P. & Soares, C. G. 2008. Hindcast of the wave conditions along the west Iberian coast. *Coastal Engineering,* 55, 906-919.

Salmon, S., Bryan, K. & Coco, G. 2007. The use of video systems to measure run-up on beaches. *Journal of Coastal Research,* 50, 211-215.

Sancho-García, A., Guillén, J., Simarro, G., Medina, R. & Cánovas, V. Beach inundation prediction during storms using direferents wave heights as inputs. 2012. International Conference on Coastal Engineering.

Santos, F., Pais-Barbosa, J., Teodoro, A. C., Gonçalves, H., Baptista, P., Moreira, A., Veloso-Gomes, F., Taveira-Pinto, F., Gomes-Costa, P., Lopes, V. & Neves-Santos, F. Coastal morphodynamic features/patterns analisys through a video-based system and image processing. 2012. 85381Q-85381Q-12.

Saville Jr, T. 1957. Wave Run-Up on Composite Slopes. *Coastal Engineering Proceedings,* 1**,** 41.

Schindelin, J., Arganda-Carreras, I., Frise, E., Kaynig, V., Longair, M., Pietzsch, T., Preibisch, S., Rueden, C., Saalfeld, S. & Schmid, B. 2012. Fiji: an open-source platform for biological-image analysis. *Nature methods,* 9**,** 676-682.

Schwiegerling, J. Field guide to visual and ophthalmic optics. 2004. Spie.

Sembiring, L. E. 2015. *Rip Current Prediction System for Swimmer Safety: Towards operational forecasting using a process based model and nearshore bathymetry from video.* TU Delft, Delft University of Technology.

Sethian, J. A. 2003. Level set methods and fast marching methods. *Journal of Computing and Information Technology,* 11**,** 1-2.

Shi, J. & Malik, J. 2000. Normalized cuts and image segmentation. *IEEE Transactions on pattern analysis and machine intelligence,* 22**,** 888-905.

Shoshany, M. & Degani, A. 1992. Shoreline detection by digital image processing of aerial photography. *Journal of Coastal Research***,** 29-34.

Silva, A., Taborda, R., Catalão, J. & Freire, P. 2009. DTM extraction using video-monitoring techniques: application to a fetch limited beach. *Journal of Coastal Research***,** 203-207.

Simarro, G., Bryan, K. R., Guedes, R. M., Sancho, A., Guillen, J. & Coco, G. 2015. On the use of variance images for runup and shoreline detection. *Coastal Engineering,* 99**,** 136-147.

Simm, J., Brampton, A. H., Beech, N. W., Research, C. I., Association, I. & Brooke, J. S. 1996. *Beach Management Manual*, Construction Industry Research and Information Association.

Skamarock, W. C., Klemp, J. B., Dudhia, J., Gill, D. O., Barker, D. M., Wang, W. & Powers, J. G. 2005. A description of the advanced research WRF version 2. DTIC Document.

Smith, R. & Bryan, K. 2007. Monitoring beach face volume with a combination of intermittent profiling and video imagery. *Journal of Coastal Research***,** 892-898.

Stafford, D. & Langfelder, J. 1971. Air photo survey of coastal erosion. *Photogrammetric Engineering*.

Stockdon, H., Thompson, D., Plant, N. & Long, J. 2014. Evaluation of wave runup predictions from numerical and parametric models. *Coastal Engineering,* 92**,** 1-11.

Stockdon, H. F., Holman, R. A., Howd, P. A. & Sallenger Jr, A. H. 2006. Empirical parameterization of setup, swash, and runup. *Coastal Engineering,* 53**,** 573-588.

Stockdon, H. F., Sallenger Jr, A. H., List, J. H. & Holman, R. A. 2002. Estimation of shoreline position and change using airborne topographic lidar data. *Journal of Coastal Research***,** 502-513.

Suanez, S., Cancouët, R., Floc'h, F., Blaise, E., Ardhuin, F., Filipot, J.-F., Cariolet, J.-M. & Delacourt, C. 2015. Observations and predictions of wave runup, extreme water levels, and medium-term dune erosion during storm conditions. *Journal of Marine Science and Engineering,* 3**,** 674-698.

Suzuki, T., Verwaest, T., Hassan, W., Veale, W., Reyns, J., Trouw, K., Troch, P. & Zijlema, M. The applicability of SWASH model for wave transformation and wave overtopping: A case study for the Flemish coast. Proceedings of the 5th International Conference on Advanced COmputational Methods in ENgineering (ACOMEN 2011), Liège, Belgium, 2011.

Thévenaz, P., Sage, D. & Unser, M. 2012. Bi-exponential edge-preserving smoother. *Image Processing, IEEE Transactions on,* 21**,** 3924-3936.

Thornton, E., Dalrymple, T., Drake, T., Elgar, S., Gallagher, E., Guza, B., Hay, A., Holman, R., Kaihatu, J., Lippmann, T. & Ozkan-Haller, T. 2000. State of Nearshore Processes Research: II.

Tolliver, D. A. & Miller, G. L. Graph partitioning by spectral rounding: Applications in image segmentation and clustering. 2006 IEEE Computer Society Conference on Computer Vision and Pattern Recognition (CVPR'06), 2006. IEEE, 1053-1060.

Tolman, H. L. 1997. *User manual and system documentation of WAVEWATCH III version 3.14*, Technical Note (US Department of Commerce, National Oceanographic and Atmospheric Administration, National Weather Service, National Centers for Environmental Predictions, 2009).

Tolman, H. L. 2009. User manual and system documentation of WAVEWATCH III TM version 3.14. *Technical note, MMAB Contribution,* 276.

Trujillo-Pino, A., Krissian, K., Alemán-Flores, M. & Santana-Cedrés, D. 2013. Accurate subpixel edge location based on partial area effect. *Image and Vision Computing,* 31**,** 72-90.

Tuan, T. Q. & Oumeraci, H. 2010. A numerical model of wave overtopping on seadikes. *Coastal Engineering,* 57**,** 757-772.

Turner, I. L., Leyden, V. M., Symonds, G., Mcgrath, J., Jackson, A., Jancar, T., Aarninkhof, S. & Elshoff, I. Predicted and observed coastline changes at the

Gold Coast artificial reef. COASTAL ENGINEERING CONFERENCE, 2001. ASCE AMERICAN SOCIETY OF CIVIL ENGINEERS, 1836-1847.

Turner, I. L., Russell, P. E. & Butt, T. 2008. Measurement of wave-by-wave bed-levels in the swash zone. *Coastal Engineering,* 55**,** 1237-1242.

Turner, I. L. L. V. M. 2000. System Description and Analysis of Shoreline Change: August 1999 - February 2000. Report 1. Water Research Laboratory, University of New South Wales.

Uunk, L., Wijnberg, K. & Morelissen, R. 2010. Automated mapping of the intertidal beach bathymetry from video images. *Coastal engineering,* 57**,** 461-469.

Valentini, N. H., Bas; Saponieri, Alessandra. Application of LiDAR as a measurement instrument for laboratory water waves. Proceedings of the Fifth International Conference on the Application of Physical Modelling to Port and Coastal Protection, 31/09/2014 2014.

Valentini N., Damiani L., Molfetta M. G. and Saponieri A. 2016. New coastal video-monitoring system achievement and development. *Coastal Engineering Proceedings*. Paper accepted No. 1781.

Valentini N., Molfetta M.G., Palumbo N., Francioso R., Pratola L., Saponieri A., Bruno M.F., Damiani L., Di Santo A. R. 2016. Coastline monitoring: experiences in Apulia region. Atti del XXXV Convegno Nazionale di Idraulica e Co-struzioni Idrauliche. Bologna: DICAM - Università di Bologna, p. 1499. ISBN 9788898010400.

Van Dongeren, A., Van Ormondt, M., Sembiring, L., Sasso, R., Austin, M., Briere, C., Swinkels, C., Roelvink, J. & Van Thiel De Vries, J. Rip current predictions through model-data assimilation on two distinct beaches. Coastal Dynamics 2013: 7th International Conference on Coastal Dynamics, Arcachon, France, 24-28 June 2013, 2013. Bordeaux University.

Verma, D. & Meila, M. 2003. A comparison of spectral clustering algorithms. *University of Washington Tech Rep UWCSE030501,* 1**,** 1-18.

Vousdoukas, M., Ferreira, P., Almeida, L., Dodet, G., Psaros, F., Andriolo, U., Taborda, R., Silva, A., Ruano, A. & Ferreira, Ó. 2011. Performance of intertidal topography video monitoring of a meso-tidal reflective beach in South Portugal. *Ocean Dynamics,* 61**,** 1521-1540.

Vousdoukas, M., Velegrakis, A., Dimou, K., Zervakis, V. & Conley, D. 2009. Wave run-up observations in microtidal, sediment-starved pocket beaches of the Eastern Mediterranean. *Journal of Marine Systems,* 78**,** S37-S47.

Vousdoukas, M. I., Kirupakaramoorthy, T., Oumeraci, H., de la Torre, M., Wübbold, F., Wagner, B. & Schimmels, S. 2014. The role of combined laser scanning and

video techniques in monitoring wave-by-wave swash zone processes. *Coastal Engineering,* 83**,** 150-165.

Vousdoukas, M. I., Wziatek, D. & Almeida, L. P. 2012. Coastal vulnerability assessment based on video wave run-up observations at a mesotidal, steep-sloped beach. *Ocean Dynamics,* 62**,** 123-137.

Wolf, J. 2009. Coastal flooding: impacts of coupled wave–surge–tide models. *Natural Hazards,* 49**,** 241-260.

Wolf, P. R. & Dewitt, B. A. 2000. *Elements of Photogrammetry: with applications in GIS*, McGraw-Hill New York.

Wright, J., Colling, A. & Park, D. 1999. *Waves, tides, and shallow-water processes*, Gulf Professional Publishing.

Yu, S. X. Segmentation induced by scale invariance. 2005 IEEE Computer Society Conference on Computer Vision and Pattern Recognition (CVPR'05), 2005. IEEE, 444-451.

Zhang, Z. 2000. A flexible new technique for camera calibration. *Pattern Analysis and Machine Intelligence, IEEE Transactions on,* 22**,** 1330-1334.

Zijlema, M., Stelling, G. & Smit, P. 2011. SWASH: An operational public domain code for simulating wave fields and rapidly varied flows in coastal waters. *Coastal Engineering,* 58**,** 992-1012.

Acknowledgments

Foremost, I want to thank my supervisor Prof. Leonardo Damiani. I greatly appreciated all his contributions of time, ideas, and funding useful to make my Ph.D. experience productive and exciting. Our stimulating, open minding, often heating meetings deeply pushed my research questions, moments that will remain etched in my memory. I would like to express my special appreciation to a mentor and colleague, Alessandra Saponieri, the great enthusiasm she has for research has been contagious for me, even during tough times during my Ph.D. I am thankful for the excellent example they have provided as successful persons and researchers.

The field work involved a number of dedicated and supportive colleagues and friends without whom this work would be much harder, my special thanks in particular to Matteo Molfetta, Gigi Pratola, and the guys of the AdBP.

I wish to acknowledge Cyril Carincotte and Arnaud Bastide for guiding into the computer vision field, their support was very important in my first modelling steps. I am also grateful for the amazing welcome in the Multitel and ACIC offices from the people of the image department and software development, respectively, who helped me a lot in software and servers “stuff”. They were always very dear friends during my stays.

Thanks to the group of PhD XXIX cycle for the amusing time we spent during classes and not.

I would like to thank my Department for the logistic support, equipment and workspace and all the people working there, who always helped lifting my spirit.

Lastly, apart for my work, my eternal thanks to my family for all their great affection and encouragement, their unconditionally support in all my pursuits; to my brother and sister for their loving concerns; to my old friends who always appreciate my research periods abroad.

Nico Valentini

Curriculum

Nico Valentini

DICATECh, Politecnico di Bari, Italy

Tel: (0039) 347/0693296; 080/5963916

Emails: nico.valentini@poliba.it; nicvalen@gmail.com

PROFILE

• Video techniques and analysis.

• Experiences in modelling and hydrodynamics simulation by using Coastal Engineering software (e.g. SWAN, SWASH) and results post-processing by means of MatLab, Python, GIS software, etc. Additional experiences in experimental analysis on Deltares (Delft) flume and LIC (Valenzano, BA) laboratory, with several instrumentations and processing software.

• Computer skills: Unix/Linux/Windows; LaTeX; basic C/C++, etc.

EDUCATION

Politecnico di Bari, Bari,

Ph.D. Civil/Environmental Engineering, March 2017 (expected)

M.S. Civil Engineer, 2013 (110/110 cum laude)

B.S. Environmental Engineering, 2010

RESEARCH INTERESTS

- Coastal Video Monitoring
- Unmanned Aerial Vehicle (UAV) application on coastal area
- Wave propagation using spectral wave model
- Wave energy calculation by using buoy and wave data re-analysis
- Terrestrial Laser Scanner (TLS) for lab wave measurements

RESEARCH CAREER

Deltares, Delft**, Netherlands, Trainee,** March-June 2013
Politecnico di Bari, Bari, **Ph.D. Candidate**, 2014-present
Multitel Research Center and its spin-off **ACIC**, Mons, Belgium, **Visiting PhD Student**, May-Aug 2015 and Jan-Mar 2016

TEACHING EXPERIENCE

Politecnico di Bari, DICATECh, Bari, **Exercises Teaching Assistant**
REGIME E PROTEZIONE DEI LITORALI, Feb-May 2014 - 2015

Short stays in foreign institutions, in Belgium.

March-August 2015. Stay in Research Centre in Telecommunications, Signal and Image Processing, “Multitel”. Initialis Science Park, Rue Pierre et Marie Curie 2, 7000 Mons, Belgium. Supervisor: Dr. Ir. Cyril Carincotte.

February-April 2016. Stay in Development Centre “ACIC”, spin-off of “Multitel”. Initialis Science Park, Rue Pierre et Marie Curie 28, 7000 Mons, Belgium. Supervisor: Ir. Arnaud Bastide.

List of publications

Journals papers and peer-reviewed International and national conference works:

- *Valentini N.*, Saponieri A., Damiani L. and Danisi A. 2017. Video analysis and numerical predictions of wave run-up. Under review at *Coastal Enginering*.
- *Valentini N.*, Damiani L., Molfetta M. G. and Saponieri A. 2016. New coastal video-monitoring system achievement and development. *Coastal Engineering Proceedings*. Paper accepted No. 1781.
- *Valentini N.*, Damiani L., Molfetta M. G. and Saponieri A. *2016.* New Algorithms for Shoreline Monitoring From Coastal Video Systems. Under review at *Earth Science Informatics.*
- *Valentini N.*, Molfetta M.G., Palumbo N., Francioso R., Pratola L., Saponieri A., Bruno M.F., Damiani L., Di Santo A. R. 2016. Coastline monitoring: experiences in Apulia region. *Atti del XXXV Convegno Nazionale di Idraulica e Costruzioni Idrauliche*. Bologna: DICAM - Università di Bologna, p. 1499. ISBN 9788898010400.
- *Valentini N.*, Saponieri A. and Damiani L. 2016. A New Video Monitoring System In Support Of Coastal Zone Management at Apulia Region, Italy. Under review at *Ocean & Coastal Management.*
- Saponieri A., *Valentini N.* and Damiani L. 2015. Wave energy potential offshore Apulian coasts (Italy). Proceedings of the Twenty-fifth (2015) *International Ocean and Polar Engineering Conference*, Kona, Big Island, Hawaii, USA, June 21-26, 2015, Volume: Vol. 1.
- Saponieri A., *Valentini N.* and Petrillo A. F. 2015. Estimation of wave energy potential offshore Apulia (Italy). E-proceedings of the 36th *IAHR World Congress*. Delft - The Hague, the Netherlands. 28 June – 3 July, 2015.
- Valentini N., Hofland B. and Saponieri A. 2014. Application of LiDAR as a measurement instrument for laboratory water waves. Proceedings of the Fifth International Conference on the Application of Physical Modelling to Port and Coastal Protection Vol.1 (2014). doi:10.13140/2.1.1464.5764.
- *Valentini N*. and Damiani L. 2014. Applicazione del LiDAR come strumento di misura di altezza d'onda in laboratorio. *Atti del XXXIV Convegno Nazionale di Idraulica e Costruzioni Idrauliche*, Bari, 7-10 Sep. 2014, ISBN 978-88-904561-8-3.

Workshop Poliba:

- Damiani L. and Valentini N.. Terrestrial Laser Scanner as a measurement instrument for laboratory water waves. 1° Workshop sullo stato dell'arte delle ricerche nel Politecnico di Bari – *1st Workshop on the State of the Art and Challenges of Research Efforts at POLIBA*. Research Contributions (C1). 111-116. Gangemi Editore.
- Molfetta M.G., Valentini N. and Damiani L.: Coastal Video Monitoring system: results and perspectives. 1° Workshop sullo stato dell'arte delle ricerche nel Politecnico di Bari – *1st Workshop on the State of the Art and Challenges of Research Efforts at POLIBA*. Research Contributions (C1). 116-121. Gangemi Editore.